Understanding and Controlling Directional Entropic Forces in Hard Particle Self-Assembly

by

Andrew S. Karas

A dissertation submitted in partial fulfillment
of the requirements for the degree of
Doctor of Philosophy
(Chemical Engineering)
in The University of Michigan
2018

Doctoral Committee:

Professor Sharon C. Glotzer, Chair
Professor Michael J. Solomon
Assistant Professor Greg van Anders
Professor Robert Ziff

Andrew S. Karas

askaras@umich.edu

ORCID iD: 0000-0002-6518-3376

For Katie, whose love and support knows no bounds.

ACKNOWLEDGEMENTS

I want to thank my graduate advisors Sharon Glotzer and Greg van Anders and the rest of my committee, Bob Ziff and Mike Solomon. Their time, insights, and mentorship have helped me immensely throughout graduate school.

I have had the pleasure of working alongside many other great researchers in my time with the Glotzer group, and I would like to thank everyone I have worked with as well as those who came before me in helping to set the framework that exists today. I owe a particular debt of gratitude towards Pablo Damasceno, who helped show me the ropes of how to research self-assembly through simulations. Jens Glaser and Julia Dshemuchadse have been wonderful friends and even better co-authors to work alongside of. Ryan Marson and Eric Harper have also been great friends and mentors. The work that I do has required simulation and software tools written by others, so I would like to thank and acknowledge all who do code development, especially Joshua Anderson, Matthew Spelling, Jens, and Eric. I also want to thank Nathan Minsk for his excellent initial work in studying the behavior of dodecahedra. I would like to give special thanks to Research Manager Karen Coulter. Her hard work is vital to what we do, and the group would fall apart without her.

TABLE OF CONTENTS

LIST OF FIGURES

Figure

ABSTRACT

Particle shape plays a critical role in determining how systems of hard particles self-assemble into ordered structures. Under the hard particle model, the maximization of entropy dictates how systems minimize their free energy. The theory of directional entropic forces attempts to explain hard particle behavior through effective forces that particles exert on one another. These effective forces, which are statistical in nature, account for why particles enter specific relative configurations with one another in order to maximize the entropy of the system.

This work examines the role of directional entropic forces in various systems. I show how the use of many small penetrable particles (the depletion interaction) can control the self-assembly of cuboctahedra into different structures based on the size of the depletant particles. Large depletants induce packing behavior in a fashion similar to increasing pressure in a depletant-free system, but sufficiently small depletants lead to a simple cubic crystal assembly by enhancing directional entropic forces at a shape's largest facets, in effect changing the valence for the entropic bonds a system forms. I compute free energies in these systems as a function of depletant size and concentration by using Free Volume Theory, a technique that accounts for entropic contributions from both the colloid and depletant phase. To examine specific effects of shape change, I compute directional entropic forces in shape families across changes in facet size. I show that rounding a chiral Voronoi particle can suppress the chiral nature of the directional entropic forces, and through depletion can re-strengthen

them. I additionally show how the optimal shape for assembling a diamond crystal has larger facets than would be expected from packing arguments because these larger facets induce stronger directional entropic forces. I further study a group of shapes that form plastic crystals, wherein particles exhibit translational order but orientational disorder. To compare the behavior of particles, I develop new analysis methods to quantify global orientational order, relative angular separations between neighboring particles, and a rotational autocorrelation function. I show that, upon compression, these systems are capable of undergoing gradual ordering transitions, first-order transitions, and orientationally supercooled states that approach an orientational glass transition, and I identify how the valence set by the directional entropic forces connects to these different transition behaviors. Finally, I analyze systems of truncated dodecahedra that are capable of assembling the highly symmetric face-centered cubic crystal as well as the complex β-Mn and γ-brass phases with large unit cells and symmetrically distinct Wyckoff sites. In the complex phases, particles in certain Wyckoff sites experience stronger directional entropic forces and adopt an icosahedral coordination environment with less free volume. The other particles in these systems have a greater amount of free volume and are able to rotate more easily. I present the idea that the local free volume fluctuations that stabilize these complex phases is analogous to behavior seen in metallic and soft matter systems which undergo charge and mass transfer, respectively. The coordination for the sites with less free volume resembles a preferred local dense packing that directional entropic forces will favor. Overall, this work explores how the valence set by emergent directional entropic forces dictates phase behavior.

CHAPTER I

Introduction

1.1 Motivation

New ways of making and processing materials has the power to fundamentally change society. Advancements in metallurgy helped in transforming civilizations to the Bronze and Iron Ages, the use of polymers slashed production costs and made consumer items more widely accessible beginning in the 20th century, and most recently the ability to process silicon allows for increasingly larger computing power in increasingly smaller devices. The next age of materials may be marked by a concept of materials-by-design [1]. Under this paradigm, someone in need of a material would be able to select a specific set of properties (*e.g.* stiffness, conductivity, shape, etc.), and a device or process would be able to return material that meets these guidelines. 3D printing is an example of a current technology for producing objects that operates under the same principle as materials-by-design: one can pass in a model and the 3D printer will produce the desired object. Processes such as chemical vapor deposition, photolithography, or scanning probe methods can similarly be used to build nano-scale features with high fidelity [2, 3].

The manufacturing techniques mentioned in the last paragraph possess various drawbacks that will prevent these techniques alone from being able to fully realize

a materials-by-design future. They all require some sort of external device to create the material with the desired form, they involve multiple preparation steps, and there is the potential for bottlenecks during manufacturing. One can imagine a better way to achieve production at larger scales if individual components just "knew" where to go and arranged on their own when building up a material. Such bottom-up manufacturing techniques do exist, and the process is known as self-assembly.

Self-assembly refers to the spontaneous organization of components into ordered structures without human intervention directly guiding the positions of the individual components [4, 5]. Self-assembly is a ubiquitous process occurring in many different systems and at many different length scales, such as molecules forming nanostructures [6, 7], crystals grown from colloids [8], or the folding of amino acid sequences into functional proteins [9]. Self-assembly is driven by repulsive and attractive interactions between particles as well as entropic considerations. Particles undergoing self-assembly need to be able to move around through space and test different relative configurations; if particles irreversibly bind with one another disordered glasses or gels are nearly guaranteed to form [4]. This work focuses on self-assembly as it relates to colloids. Materials formed from colloidal assemblies have features at the nanometer to micrometer length scale, and they can have applications in areas such as photonics [10, 11], catalysis [12], and superhydrophobicity [13].

One element that makes colloidal particles particularly exciting for self-assembly processes is the ability to program how particles interact with one another through many independent and continuously adjustable anisotropy dimensions [14]. Colloids can be fashioned with hydrophobic [8] or DNA [15] patches such that they bond with one another at these patches. One can also adjust particle shape based on features like the aspect ratio [16, 17] or facetting [18, 19]. This thesis focuses on the role

of particle shape in entropy-driven self-assembly. The rest of the introduction is as follows: I first discuss the role of computer simulations in this field, and how I use simulation to study systems governed by the hard particle model. I then discuss relevant thermodynamic principles, with a focus on how entropy should be interpreted. I then discuss developments behind entropy-driven assemblies. I ultimately conclude the introduction by providing an overview of the research that makes up my thesis.

1.2 Use of Computer Simulations

Given that there are so many possibilities for adjusting the properties of colloids, scientists need a practical means in helping to explore this vast design space. Computer simulations are capable of meeting this need [20]. Using molecular dynamics or Monte Carlo techniques, we can predict the equilibrium and/or kinetic behavior for systems of colloidal building blocks. It is far easier to launch 1000 computer simulations and use automated tools to analyze the results compared to doing the same with physical experiments.

I simulate systems using the hard particle model. The hard particle model assumes that particles do not experience attraction or repulsion with one another; they simply cannot occupy the same space. The potential energy of interaction between two hard particles P_1 and P_2 is given by:

$$U(P_1, P_2) = \begin{cases} \infty & \text{if } P_1 \text{ and } P_2 \text{ overlap} \\ 0 & \text{otherwise} \end{cases} \tag{1.1}$$

While this model is simple, it can mimic phenomena in which strong, short-ranged repulsions are the dominant effect, and simulation has shown that the structure of hard sphere fluids can be similar to that of more complicated interatomic potentials

[21]. Colloidal particles are capable of behaving like hard particles when long-range electrostatic interactions are tuned out by adding salt to the solvent [22]. This model has frequently been employed to study the effect of shape on phase behavior [23, 24, 25, 26, 27].

Monte Carlo (MC) methods, specifically the Metropolis approach [28], allow us to simulate systems with arbitrary interaction potentials. MC simulations stochastically advance the positions and orientations of objects in a thermodynamic ensemble. Metropolis MC simulations employ importance sampling: there is not an attempt to test every conceivable arrangement of particles; instead phase space is sampled according to the underlying probability distribution function. To advance forward a step in an MC simulation, a particle is randomly chosen and is either displaced or rotated by some random amount to generate a new trial configuration. The probability of accepting the move is given by

$$\Pr_{\text{accept}} = \min(1, e^{-(U_{new}-U_{old})}) \tag{1.2}$$

Under the hard particle model, the change in energy in a trial configuration is always ∞ (overlap) or 0 (no overlap), which in turn leads to acceptance probabilities of 0 or 1. Thus any MC move that does not generate an overlap is accepted. Figure 1.1 provides a visualization of these moves for hard particle systems. Colloidal particles undergoing Brownian motion will move through solvent in a fashion similar to the random, small displacements of a Metropolis MC simulation.

I perform simulations using the hard particle Monte Carlo (HPMC) feature of HOOMD-blue [29, 30, 31]. HPMC is an efficient and flexible toolkit capable of simulating many anisotropic geometries and thermodynamic ensembles. HOOMD-blue employs a high-level python scripting interface for ease of use, and it executes

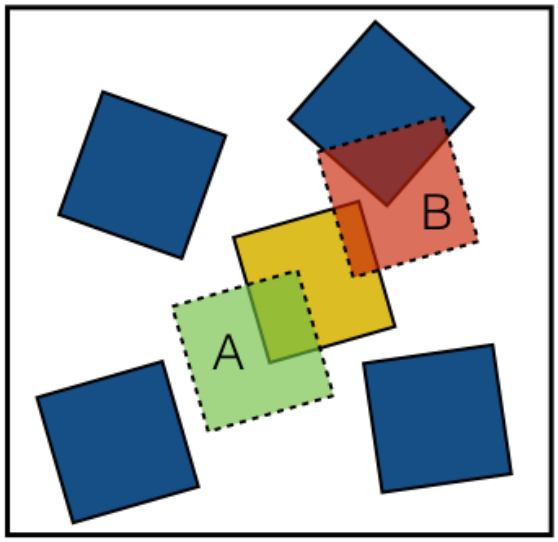

Figure 1.1: Examples of a trial move for the central yellow particle that would be accepted (**A**) and rejected (**B**) in an MC simulation of hard particles. When no overlaps are introduced as in trial move **A**, there is no change to the system energy and the move is always accepted because $e^{-(U_{new}-U_{old})} = e^0 = 1$. A trial move that generates an overlap (**B**), leads to the new configuration having an infinite potential energy, and it is rejected because $e^{-\infty} = 0$

simulations fast and in parallel on multiple CPU or GPU cores.

1.3 Important Thermodynamic Principles

By definition, thermodynamic systems tend towards the equilibrium configuration. This evolution to the equilibrium state is the driving force behind the self-assembly of particles. Equilibrium is defined as a state that minimizes a system's free energy. Let us consider a system in which the number of particles, the volume, and the temperature are kept constant (the NVT or Canonical Ensemble). The appropriate state function to describe this system is the Helmholtz free energy, A:

$$A = U - TS \tag{1.3}$$

In the above, U represents the potential energy, T is the temperature, and S is the entropy. Entropy is often thought of as some sort of measure of disorder.

This definition can hold for a colloquial definition of order *vs.* disorder, but it is not rigorously true in considerations of spatial order. Instead, we must stick with thermodynamics and Ludwig Boltzmann, who formulated entropy as a measure of the number of microstates, Ω, available to a closed system where all microstates have the same energy:

$$S = k_B \ln(\Omega) \tag{1.4}$$

This equation defines entropy for a thermodynamic system as being directly proportional to the number of ways the individual components can be arranged. Entropy differences between different macrostates can be illustrated by splitting five (distinguishable) marbles between two separate bags. One example of a macrostate would be all marbles inside of the first bag. There is only a single microstate ($\Omega = 1$) to achieve such a configuration. A second macrostate would be to have four marbles in the first bag and one marble in the second bag. To reach this macrostate from the first one, any one of the five marbles could be placed in the second bag, and there are thus five microstates that correspond to this macrostate. Accordingly, having the marbles divided between the two bags is a higher entropy configuration than having all marbles in a single bag.

In this thesis, I consider systems in which entropy is solely responsible as the driving force to minimize free energy. Under the hard particle model, any allowed configuration of particles will have $U = 0$, so free energy is minimized by increasing entropy. This means that an ordered configuration must be one which maximizes the number of microstates available to the system's components.

One of the more common examples of producing order through entropy is the depletion interaction. Depletion refers to the effective attraction experienced by

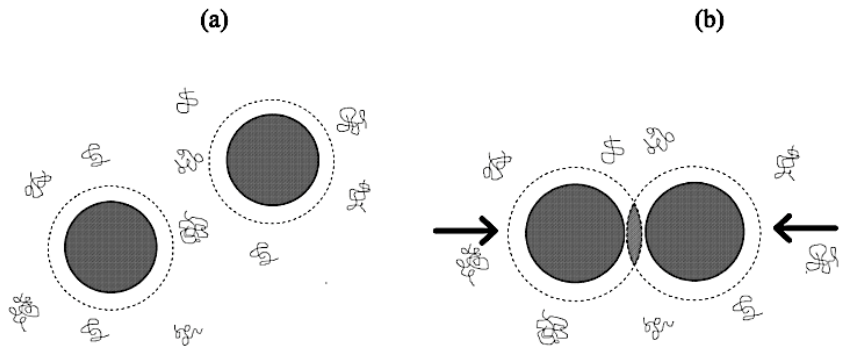

Figure 1.2: In the classical model, depletants are soft polymer coils, and their center of mass is excluded from a shell surrounding the colloids with a radius equal to the polymer radius of gyration. **a.)** When the colloids are separated, the depletants exert an isotropic osmotic pressure on the colloids. **b.)** Once the colloids' excluded volume shells overlap, the depletants are unable to come between the colloids and there is an imbalance in the osmotic pressure that pushes the colloids together. This effective attraction also results in a greater amount of free volume available to the depletants. Because the polymer-polymer interactions are soft, they are often treated as ideal gas particles with respect to one another. Image via Ref. [43]

systems of colloids or nanoparticles immersed in solution along with many smaller depletant particles (typically non-adsorbing polymers). When colloids aggregate (and the polymers are "depleted" from the colloid phase), the depletant polymers have more available space (and thus more entropy). An example schematic is included as Fig. 1.2. Before the theory behind depletion had been developed, it was used in practice to induce creaming of latex particles [32]. The theory of depletion was first posed in the 1950s by Asakura and Oosawa [33, 34] and was later systematically expanded upon by Vrij [35]. Depletion is widely used for inducing assembly [36, 37, 38, 39, 40, 41, 42].

1.4 The Development of Theories on Entropic Assemblies

The notion that entropy alone can be the driving force for ordering in single component systems has been primarily developed over the past 70 years. Lars Onsager was the first to formulate an entropy-driven ordering transition in a single component system. In a paper from 1949 [44], he mathematically reasoned that upon compres-

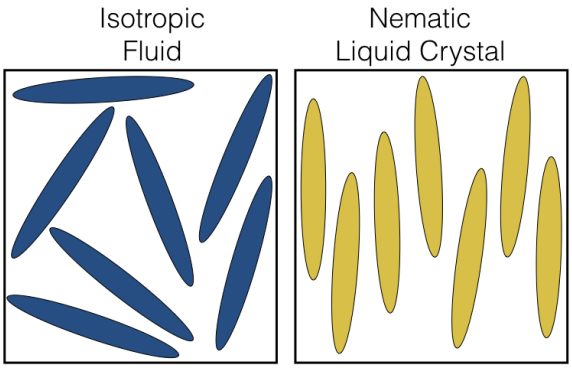

Figure 1.3: Example of the fluid-nematic phase transition described first by Onsager [44]. In the fluid phase, there is a greater variety in the orientations of the rods, but there is little space to move any of the individual rods. In the liquid crystal, the particles align (orientational order), and this allows rods to move up and down past one another (thereby increasing the translational entropy).

sion, a fluid of thin hard rods must undergo a transition from the translationally and orientationally disordered fluid phase to a liquid crystalline nematic phase with orientational order and translational disorder. This ordering transition does decrease the orientational entropy of the system, but it greatly increases the translational entropy. Fig. 1.3 provides an example visualization of this phenomenon. Soon after, entropic order was further pushed by Kirkwood, who predicted the crystallization of hard spheres via entropy [45]. This hypothesis was controversial, but it gained acceptance in 1957 when molecular dynamics and Monte Carlo simulations of the crystallization phenomenon were performed by Alder & Wainwright[46] and Wood & Jacobson [47], respectively. It took until 1968 for computer simulations to advance to a point wherein Hoover and Ree could determine the coexistence densities for the first-order, fluid-to-solid transition of hard spheres ($\phi = 0.494$ and $\phi = 0.545$) [48]. Physical experiments [49, 50], including ones performed in microgravity aboard the Space Shuttle Columbia [51], with hard colloidal spheres have since confirmed simulations results.

Shape has proven to play a major role in the crystallization of hard particles.

In this area, computer simulation has proven to be invaluable. The issue was first pushed by Daan Frenkel, who simulated the phase behavior of hard rods [23, 52]. He showed that in addition to the nematic phase first predicted by Onsager, hard rods with spherical caps are capable of forming a smectic phase. Another breakthrough in entropic ordering occurred in 2009, when Haji-Akbari *et al.* showed that tetrahedra (a simple shape with four identical, triangular facets) is capable of self-assembling a quasicrystal [24, 53]. A quasicrystal is a complex phase in which there is long range periodicity but no repeated unit cell as exists in a crystal. Further complex and unexpected self-assemblies were identified by Damasceno *et al.* in an expansive study of 145 convex polyhedra [26]. In addition to uncovering unexpected phases, this work showed that hard particles tend to self-assemble phases with coordination numbers and local motifs similar to that of the dense fluid, not the densest packing structures. Many shapes order into mesophases with partial order: highly anisotropic particles tend towards liquid crystals (orientational but not translational order) and more sphere-like particles form plastic crystals (translational but not orientational order) [25, 26, 54, 27]. Even though long-range orientational order does not exist in plastic crystals, anisotropic particles tend to show a few preferred orientations [55], and the existence of facets lowers the free energy barrier for crystal nucleation from a fluid as compared to systems of hard spheres [56].

None of the above would matter very much if it were impossible to synthesize these kinds of particles. Fortunately, plenty of progress has been made in controlling the shape of nano- and colloidal particles and their use in assemblies. Many different groups have shown an ability to grow polyhedral nanoparticles from materials like silver, platinum, and gold [12, 18, 19, 57, 58, 59]. Furthermore, these facetted particles will self-assemble structures that depend on nanoparticle shape

[19, 59, 60, 61, 62, 63, 64, 65, 66]. The depletion interaction has also been employed in controlling the assembled structure [59, 64].

Given all available evidence, the theory of directional entropic forces, or DEFs [67, 68, 69], attempts to explain the phenomenon of how hard particles will self-assemble in entropic systems. In the simplest terms, this theory states that particles tend to align along their facets and optimize their local packing because these configurations maximize the total system entropy. More specifically, van Anders *et al.* [68] show that DEFs are on the order of a few times the thermal energy (k_BT), which places the strength of DEFs around the level of traditional depletion and van der Waals forces (though these forces can reach larger values near 100 k_BT). DEFs can be measured by a potential of mean force and torque (PMFT) [68, 69]. The PMFT is an effective potential which describes the free energy associated with particles in a particular relative position and orientation. One consideration that arises out of this treatment [68] for the free energy on a particle pair basis is that there are two terms of importance for minimizing free energy: the entropy associated with a single particle pair in a configuration (*e.g.* aligned at their facets), and the entropy of all other particles in the system given the two particles in that configuration. In this way, it is possible to think of hard particle assemblies as something akin to "self-depletion" wherein entropy considerations for all other particles in a system creates a driving force for particles to align in this emergent fashion.

In the time since the notion of DEFs was first introduced, additional studies of hard polyhedra have helped push this theory. Teich *et al.* studied the packing of the platonic solids under spherical confinement [70]. They were able to show that the locally dense motifs of tetrahedra within the quasicrystal arise in these spherical packings. Geng *et al.* studied the inverse design of crystals from hard particles [71].

Their approach allows for particles to change shape within an extended, "alchemical" ensemble [72] such that the particle will take on the shape that maximizes entropy for a particular crystal structure. They found that shapes will develop facets and a corresponding entropic valence. Harper *et al.* investigated DEFs in two-dimensional systems and showed that these emergent, entropic forces can be viewed as *entropic bonds* similar to hydrogen bonding in molecular systems [73]. Particle facetting unquestionably plays a vital role in shaping DEFs and correspondingly directing particles' entropic valence, or how particles tend to arrange.

1.5 Thesis Overview

In this work, I use the theory of directional entropic forces to describe the entropy-driven behavior of hard particle systems. My overall aims are twofold: 1.) I want to explain unique phenomena of hard particles through this lens of DEFs, and 2.) I aim for the takeaway lessons from these systems to be general enough to be applied elsewhere for engineering specific behavior. In Chapter 2, I investigate the behavior of an anisotropic particle (the cuboctahedron) in the presence of penetrable hard sphere depletants. The faceting of the cuboctahedron allows for the colloid phase to form different crystal structures (in contrast to depletion with hard spheres) as a function of the depletant size and concentration. I extend Free Volume Theory [74] to anisotropic particles to rationalize this behavior. I also show how the depletant properties impact the directional entropic forces, allowing for the forces to become stronger at the larger facets when using smaller depletant sizes. In Chapter 3, I use the PMFT to explain the behavior in systems where the shape is continuously adjusted along a single parameter axis. I show how an optimally truncated tetrahedron best controls the local environment for the self-assembly of a diamond structure. I

further show how the rounding of a Voronoi particle suppresses the specific interactions necessary for the assembly of the target structure. Using depletion on the rounded shape can strengthen the DEFs to produce the target structure. In Chapter 4, I explore the behavior of plastic crystals: a phase in which there is positional order but orientational disorder. I focus on five different shapes that all form face-centered cubic crystals, and I develop tools to show how these systems display different behavior. I consider how these systems change as density increases, and I find three separate types of transitions: a first-order transition from the face-centered cubic plastic crystal to a body-centered tetragonal crystal, a smooth development of order without a change in the crystal phase, and the approach to a glass transition in orientation such that orientational rearrangements slow down and particles become locked into a few distinct orientations without long range orientational order. I further connect how the DEF valence corresponds with these distinct transition types. In Chapter 5, I analyze the phases that truncated dodecahedra self-assemble. In addition to face-centered cubic crystals, these particles assemble complex crystal phases (β-Mn and γ-brass) with multiple Wyckoff positions. I show that particles take on different local environments in the distinct Wyckoff positions. I propose β-Mn and γ-brass form as a result of "free volume exchange" between the different Wyckoff sites such that some particles adopt environments where movement is restricted and DEFs are stronger. The low free volume environments correspond with icosahedral coordination, which is a particularly effective local packing of dodecahedra, and it therefore provides space for other particles to have a greater average free volume. Finally in Chapter 6, I make concluding remarks and discuss some potential directions for future research.

CHAPTER II

Using Depletion to Modify Directional Entropic Forces

This chapter is adapted from a publication in *Soft Matter* authored by A.S. Karas, J. Glaser, and S. C. Glotzer [75].

2.1 Introduction

New, programmable materials can be realized from nanoparticles that form ordered solids to maximize their entropy. Recent studies have investigated how changes to particle shape affect the solids formed via self-assembly [67, 69, 26, 27, 54]. In such systems, directional entropic forces emerge upon crowding so that particles adopt locally dense configurations to maximize the system entropy [68]. In binary systems, the depletion interaction, in which the osmotic pressure of small polymers induces an effective attraction between colloids, provides another route to induce order via entropy [34]. When combined with shape, depletion is a powerful tool to control structure formation because it promotes facet-specific alignment of anisotropic particles even for low concentrations of colloids [38]. For example, in systems of roughened platelets, adjusting the depletant size allows one to selectively suppress or enhance specific bonding [76]. In three-dimensional crystalline assemblies of metallic nanoparticles, depletants have been used to control lattice spacings [77] and to stabilize exotic structures instead of densest packings [59]. The swelling of thermo-sensitive

depletants causes reversible transformations in cube-like superballs between a square lattice and a canted phase in a quasi-two dimensional system [64]. By calculating the probability of binding, or facet alignment, for hard facetted spheres with depletants, van Anders et al. [68] demonstrated how changing depletant concentration and facet size changes the strength of emergent directional entropic forces.

Cuboctahedra belong to a shape family in which a cube can be truncated into an octahedron. Simulations predict that cuboctahedra form a rotator body centered cubic (BCC) crystal at intermediate pressures while the cuboctahedra densest packing (CODP) formed at high pressures can be viewed as a sheared BCC crystal with a rhombohedral primitive cell [27]. Both rotator and sheared BCC (sBCC) structures are observed in self-assemblies of perfect octahedra, though no previous studies have shown hard cuboctahedra forming a simple cubic (SC) phase, as is known to form from cubes. Experimentally, silver nanoparticles with cuboctahedral shape have been grown with diameters of 150-200 nm [61]. Henzie et al. [59] used such particles in sedimentation-driven self-assembly studies and were able to form the densest-packed structure as well as a face-centered tetragonal (FCT) structure with depletion.

Here we show how depletion-induced effective shape change can control the self-assembly of polyhedral particles, using the specific example of cuboctahedra. Monte Carlo simulations that treat depletants as penetrable hard spheres demonstrate the ability to change the self-assembly of cuboctahedra into different colloidal crystals. We report that depletion can lead to the assembly of a simple cubic phase. Extending previous models for hard spheres [74], we incorporate the contributions of both colloid and depletant entropy into a consistent thermodynamic picture of the phase behavior of anisotropic colloids with depletants. Remarkably, we find that, although the contribution to the free energy is dominated (as expected) by the depletant entropy,

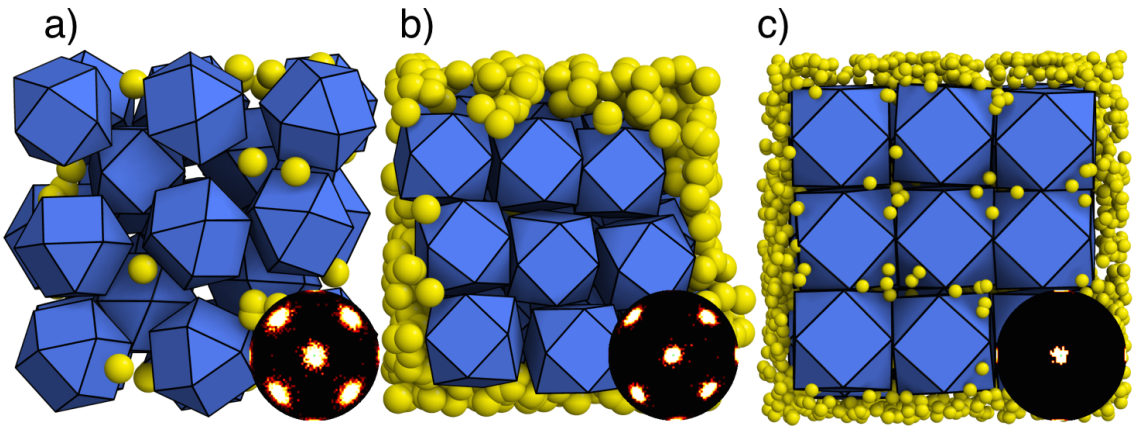

Figure 2.1: Example ordered configurations to represent the mechanisms by which depletant size and concentration affect colloid crystal structure. The pictured structures were selected from larger crystal grains that formed in self-assembly simulations with $\phi_{\text{col}} = 0.55$. In our simulations, depletants are implicitly modeled; here they are included as a visual aid. Representative bond order diagrams are also shown. **(a)** In the rotator BCC phase, the depletant concentration is low and the depletants (yellow, shown with $q = 0.25$ and $\phi^{\text{r}}_{\text{dep}} = 0.20$) sit in random void spaces throughout the structure. **(b)** In the sBCC phase, the cuboctahedra (blue) pack densely and the depletants (shown with $q = 0.25$ and $\phi^{\text{r}}_{\text{dep}} = 0.60$) exist outside of the crystal, providing osmotic pressure which causes the dense packing. **(c)** In the simple cubic phase, small depletants (shown with $q = 0.10$ and $\phi^{\text{r}}_{\text{dep}} = 0.10$) occupy octahedral void spaces throughout the SC crystal in addition to sitting outside of the crystal in large pockets of free volume. Image via Ref. [75]

the *colloid* entropy contribution must be included to rationalize the stability of the SC phase. We further show how varying depletion size and concentration changes the directional entropic forces acting upon the cuboctahedra, and we argue that these changes to entropic forces are akin to effective shape changes with anisotropic particles.

2.2 Methods

To study the behavior of cuboctahedra with depletants, we simulate their assembly across a range of depletant and colloid densities, for two depletant sizes. We use a recently developed Monte Carlo (MC) simulation method that implicitly treats arbitrarily shaped hard particles in osmotic equilibrium with a reservoir of penetrable hard sphere depletants [78]. This method is built on top of HPMC in HOOMD-blue

[29, 31]. In these simulations, we consider a semigrand ensemble where the system is kept at a constant volume with colloid density ϕ_{col} and depletant reservoir density $\phi^{\text{r}}_{\text{dep}}$. The depletant size is set by a parameter $q = \sigma_{\text{dep}}/\sigma_{\text{col}}$, the ratio of depletant radius to colloid circumsphere radius. Our MC method only stores information on the colloids; it accounts for depletion effects by sampling the free volume change in the local environment of a moved colloid in a statistically exact fashion.

We calculate the potential of mean force and torque (PMFT) in systems of cuboctahedra with depletants. These calculations were performed on dense fluid systems and they allow us to visualize the directional entropic forces (DEFs) that will ultimately result in solid formation [67, 69, 68, 79].

2.2.1 Free Volume Theory

We use a perturbative *ansatz* known from Free Volume Theory in order to predict coexistence of different cuboctahedra phases. Our implementation follows the framework of previous implementations [74, 80, 81], although a key difference is that we rely on numerical calculations of the cuboctahedra free energy whereas previous implementations of Free Volume Theory have focused on hard sphere systems where there are well developed analytical expressions for the equation of state and free volume. Free Volume Theory relies on a semigrand ensemble with the following full expression for free energy: [32]

$$F(N_{\text{col}}, \mu_{\text{dep}}, V, T) = F(N_{\text{col}}, \mu_{\text{dep}} \to -\infty, V, T) - \int_{-\infty}^{\mu_{\text{dep}}} N_{\text{dep}} d\mu_{\text{dep}} \tag{2.1}$$

Here, N_{dep} is the number of depletants in the system. According to the Widom insertion theorem [82], the chemical potential of depletants in the system is $\mu_{\text{dep}} = \text{const} + k_B T \ln(N_{\text{dep}}/\langle V_{\text{free}} \rangle)$ and, by definition, the chemical potential in the external

reservoir is $\mu_{\text{dep}} = \text{const} + k_B T \ln(n^{\text{r}}_{\text{dep}})$. Equating these terms leads to the result $N_{\text{dep}} = n^{\text{r}}_{\text{dep}} \langle V_{\text{free}} \rangle$. Substituting these expressions into the free energy relationship, and making the critical assumption of Free Volume Theory that $\langle V_{\text{free}} \rangle$ can be treated as a constant as the depletion concentration varies leads to:

$$F(N_{\text{col}}, \mu_{\text{dep}}, V, T) \approx A(N_{\text{col}}, V, T) - n^{\text{r}}_{\text{dep}} \langle V_{\text{free}} \rangle k_B T \tag{2.2}$$

$\langle V_{\text{free}} \rangle$ can be replaced by definition with αV. In doing our analysis with a common tangent construction, we work with the free energy density $f(\phi_{\text{col}}, \mu_{\text{dep}}) = F(N_{\text{col}}, \mu_{\text{dep}}, V) v_0 / V$ where v_0 is the volume of a single colloid. The purpose of the common tangent construction is to find densities at which two phases will coexist, meaning that they have equal pressures and chemical potentials. The pressure is defined as:

$$P = -\left[\frac{\partial F}{\partial V}\right]_{N,T} = -\frac{1}{v_0}\left[\frac{\partial (Vf)}{\partial V}\right]_{N,T} = -\frac{1}{v_0}\left[f - \phi_{\text{col}} \frac{\partial f}{\partial \phi_{\text{col}}}\right]_{N,T} \tag{2.3}$$

The chemical potential is:

$$\mu = [\frac{\partial F}{\partial N}]_{V,T} = \frac{1}{v_0}\left[\frac{\partial (Vf)}{\partial N}\right]_{V,T} = [\frac{\partial f}{\partial \phi_{\text{col}}}]_{V,T} \tag{2.4}$$

For more on common tangent construction use with Free Volume Theory, we refer the interested reader to reference [80].

We use two different means of computing the Helmholtz free energy of the unperturbed system. Frenkel-Ladd integration [83] was employed to calculate free energies for the bulk SC and sBCC crystals, using an implementation for anisotropic particles

described by Haji-Akbari et al. [53]. This implementation considers both the translational and rotational degrees of freedom by tethering particles to springs about their average positions and orientations in the lattice. We performed the calculations on bulk SC and sBCC crystals for a variety of different colloid densities, ϕ_{col}, up to the densest packings [27] (~ 0.833 for SC and ~ 0.917 for sBCC).

We rely on data from the cuboctahedra equation of state when calculating free energies of the other phases. We first ran NPT simulations of systems with 4096 particles. From this, we computed the compressibility factor $Z = PV/Nk_BT$. We then used Widom particle insertion [82] to determine the chemical potential of the system at a reference density of $\phi_{\text{col},0} = 0.20$. We calculate the chemical potential at the reference density as:

$$\mu_0(\phi_{\text{col},0}) = \ln(\phi_{\text{col},0}) - \ln(\text{B}_i) - \ln(2\pi^2) \tag{2.5}$$

where B_i is the probability of randomly inserting a particle without generating an overlap, and the last term is necessary to make the normalization of the fluid free energy consistent with the free energy computed in our Frenkel-Ladd calculations [53]. Because we express rotations using normalized quaternions $\mathbf{q}^2 = 1$, the factor of $2\pi^2$ measures the surface area of the 3-sphere.

This value for the chemical potential at a reference density allows us to determine the absolute free energy by integrating over the compressibility factor:

$$f(\phi_{\text{col}}) = \phi_{\text{col}}\left[\mu_0(\phi_{\text{col},0}) \; - \; Z_0(\phi_{\text{col},0}) + \int_{\phi_{\text{col},0}}^{\phi_{\text{col}}} \frac{Z(\phi_{\text{col}})}{\phi_{\text{col}}} d\phi_{\text{col}}\right] \tag{2.6}$$

We similarly integrate over the equation of state to describe the rotator BCC phase and part of the sBCC phase. When integrating the equation of state in these cases, we use an integration constant in order to match the pressure and chemical

potential for the unperturbed fluid-rotator BCC coexistence and the rotator BCC-sBCC coexistence from reference [27].

To calculate the depletant contribution to free energy, we used Monte Carlo integration to determine the free volume as a function of depletant size across different colloid densities and phases and in both the SC and sBCC crystals. This allowed us to have an expression for $\alpha = \langle V_{\text{free}} \rangle / V$ across the full range of colloid densities.

2.3 Results and Discussion

2.3.1 Self-Assembly

Figures 2.1 and 2.2 show examples of the ordered structures formed in our self-assembly simulations as we adjusted ϕ_{col}, $\phi^{\text{r}}_{\text{dep}}$, and q, and the phase diagram, respectively. We observe three types of ordered structures: a rotator BCC crystal, a sheared BCC crystal with similar features as the cuboctahedron's densest packing, and an SC crystal. We identify these structures based on visual inspection and their bond order diagram (Fig. 2.1, insets). A bond order diagram is a 3D histogram of vectors that connect neighboring particles' centers of mass, mapped to the unit sphere. Crystal phases, as opposed to isotropic fluids, show characteristic peaks in their bond order diagrams. When the sBCC or SC crystals formed, the system phase separated into a dense solid and a less dense fluid, while rotator BCC formation led to a single phase. For any point in Figure 2.2 labeled as a fluid, no ordered phase formed after 2.5×10^7 MC sweeps. In contrast, systems often formed solids after approximately 5×10^6 MC sweeps. We first probed the phase behavior by running two independent simulations at each state point with system sizes of $N_{\text{col}} = 512$. We then confirmed these results by running four replicates at state points along the phase boundaries with system sizes $N_{\text{col}} = 1000$. With depletant size ratios $q = 0.10$ and 0.25, the type of crystal formed at high depletant concentrations is consistent

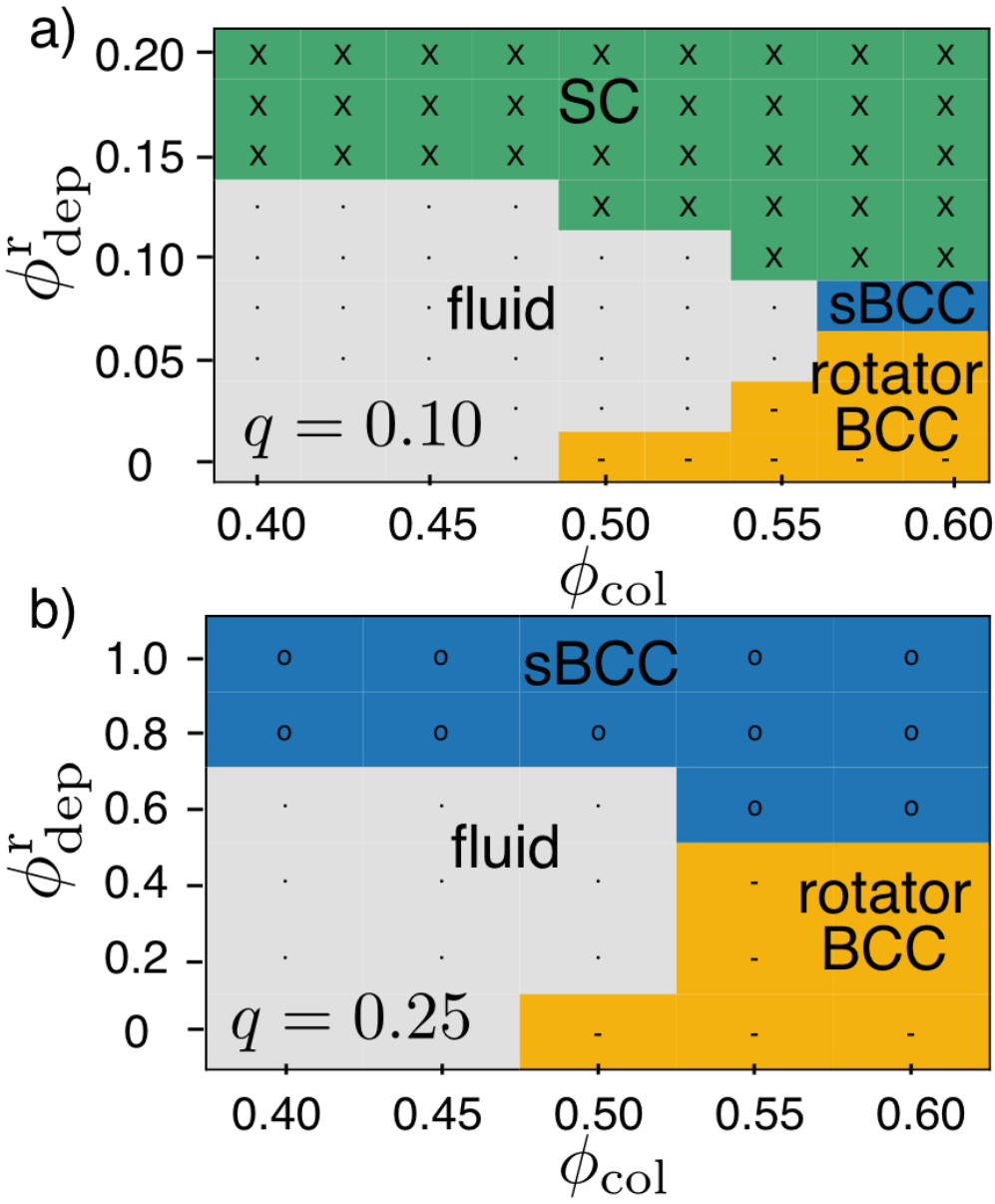

Figure 2.2: **(a & b)** Observed phase behavior of cuboctahedra in self-assembly simulations with depletants at size ratios of **(a)** $q = 0.10$ and **(b)** $q = 0.25$ for various colloid densities (ϕ_{col}) and depletant concentrations ($\phi^{\mathrm{r}}_{\mathrm{dep}}$). Image via Ref. [75]

among replicates. Overall, we observe the SC crystal to be the only ordered phase formed in simulations with $q = 0.10$ and $\phi^{\mathrm{r}}_{\mathrm{dep}} \geq 0.10$, and the sBCC crystal to form with $q = 0.25$ and $\phi^{\mathrm{r}}_{\mathrm{dep}} \geq 0.60$.

A simple scaling argument explains why the SC crystal is not stabilized by depletants with $q = 0.25$. Cuboctahedra in an SC crystal contain octahedral void space such that there is free volume available to depletants *within* the crystal. In a densely packed SC lattice, the void space is an octahedron with edge length equal to the cuboctahedron edge length, which equals the cuboctahedron's circumsphere radius σ_{col}. V_{free} can be approximated by a smaller octahedron with volume $V_{\mathrm{free}} \approx \sqrt{2}/3 * \sigma^3_{\mathrm{col}} * (1 - 2\,q)^3$. The free energy contribution from the depletants is $V_{\mathrm{free}}(q) * \phi^{\mathrm{r}}_{\mathrm{dep}} * k_B T / v_{0,\mathrm{dep}}$ where $v_{0,\mathrm{dep}}$ is the volume of a single depletant. According to these relationships, depletants with size $q = 0.25$ will require $\phi^{\mathrm{r}}_{\mathrm{dep}} > 1$ to make a contribution on the order of the thermal energy $k_B T$. In other words, larger depletants would require unphysically large depletant concentrations to stabilize the octahedral voids of the SC lattice. For reference, when $q = 0.10$, $\phi^{\mathrm{r}}_{\mathrm{dep}} = 0.02$ results in one $k_B T$ of free energy from the void space under this simplified scaling model.

From the phase diagram, we identify three regimes that lead to the cuboctahedra ordering. These different behaviors are visually represented with explicit depletants in Figure 2.1. The cuboctahedra behave as they would in a one-component system regardless of the depletant size when $\phi^{\mathrm{r}}_{\mathrm{dep}}$ is sufficiently small (Fig. 2.1**a**). Under these conditions, there is no preferential facet alignment as the particles are able to freely rotate. When $\phi^{\mathrm{r}}_{\mathrm{dep}}$ increases, the assembly behavior of the cuboctahedra depends on the depletant size in the following way. With large depletants $q = 0.25$, the cuboctahedra behave as they would in the high pressure limit for one-component systems and pack into a dense sBCC crystal (Fig. 2.1**b**). This dense arrangement

contains significant contact among facets wherein both the square and triangular facets of a cuboctahedra are in contact with neighboring particles. With small depletants $q = 0.10$, however, the cuboctahedra form an SC lattice that maximizes facet-to-facet alignment of the large square facets (Fig. 2.1**c**). By presenting our results in terms of the dimensionless concentration $\phi^{\mathrm{r}}_{\mathrm{dep}} \propto n^{\mathrm{r}}_{\mathrm{dep}} q^3$, the effect of depletant size q on the critical concentration required for self-assembly into SC or sBCC becomes apparent. Since the critical $\phi^{\mathrm{r}}_{\mathrm{dep}}$ required for assembly into SC or sBCC depends on depletant size, this indicates that the assembly is *qualitatively* different for different depletant sizes, and that, in addition to decreased void space volume, many-body effects likely become important for larger depletant radii [84].

2.3.2 Free Volume Theory

We validate our phase diagrams from simulations in Figure 2.2 by predicting phase behavior using the perturbation relationship in Equation (2.2). With this expression, which accounts for contributions from both the colloid and depletant entropy, we are able to predict whether the system can minimize its free energy by remaining in one single phase or separating into two separate phases that are at mechanical and chemical equilibria. We include example plots for free energy, pressure, and chemical potential as function of density in Figure 2.5 at the end of this subsection.

Figure 2.3 shows phase diagrams as a function of ϕ_{col} and $\phi^{\mathrm{r}}_{\mathrm{dep}}$ for both depletant sizes of interest. We denote single phase regions using a single letter, and we show regions of coexistence as those contained within the solid curves between two regions. In the two-phase regions, the system is able to minimize its free energy by separating into the two phases of different densities. We additionally represent phases predicted to be metastable using dashed lines. The observed phase behavior represented in Figure 2.2 is also included as symbols.

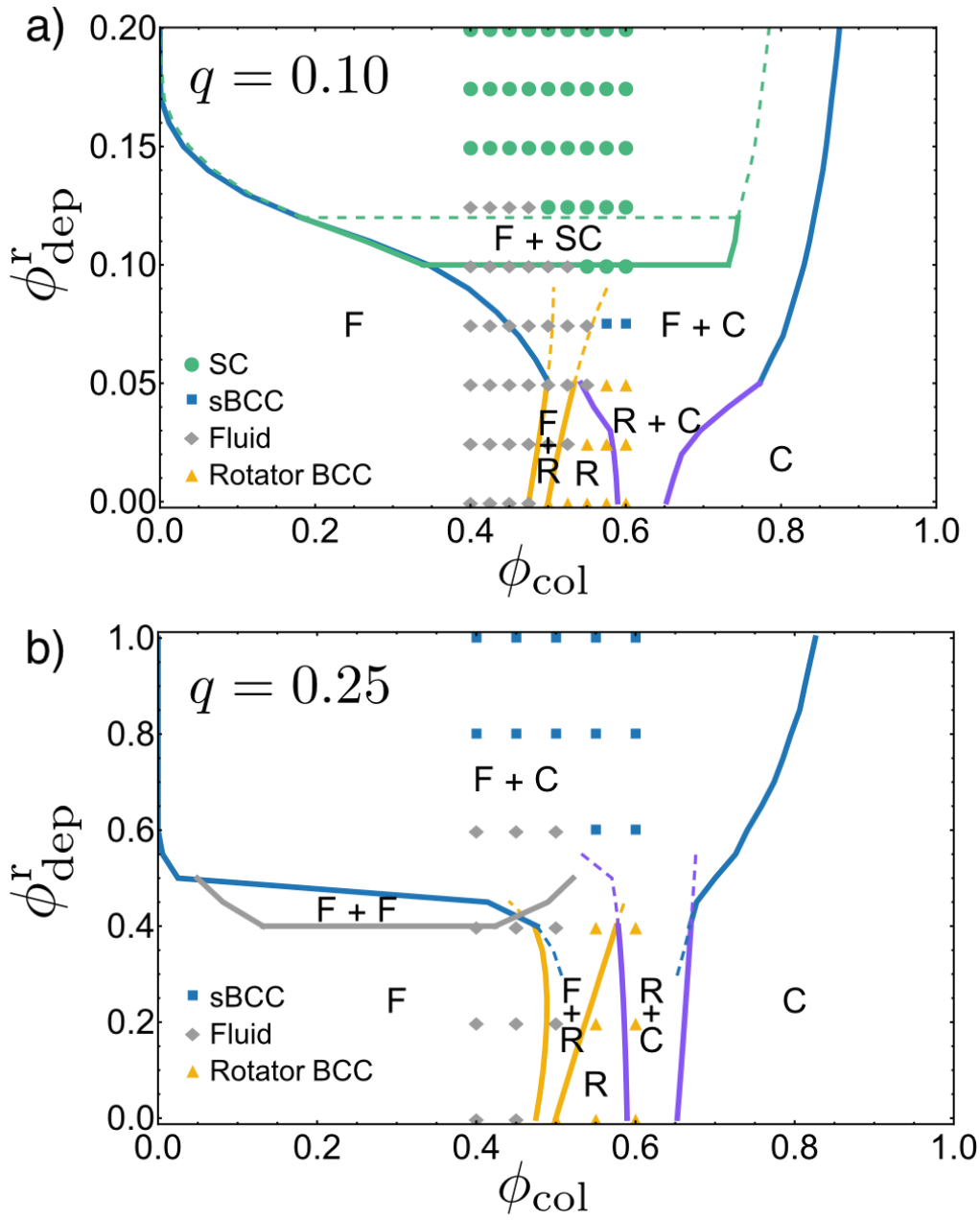

Figure 2.3: Phase diagrams of cuboctahedra with penetrable hard sphere depletants at size ratios **(a)** $q = 0.10$ and **(b)** $q = 0.25$ as a function of ϕ_{col} and $\phi^{\mathrm{r}}_{\mathrm{dep}}$. Predictions of the phase behavior from free energy calculations are noted with via text and the curves. The observed phase behavior from self-assembly simulations are noted with markers. F denotes a fluid phase, R denotes a rotator BCC phase, C denotes the sBCC phase, and SC denotes the simple cubic phase. Regions of coexistence between two phases are noted with a +. Metastable phases are denoted with dashed lines. In **(a)**, our calculations predict the F+SC coexistence to be stable for $0.10 \leq \phi^{\mathrm{r}}_{\mathrm{dep}} < 0.12$ and metastable for $\phi^{\mathrm{r}}_{\mathrm{dep}} \geq 0.12$. Image via Ref. [75]

In both Figures 2.3**(a & b)**, we find the same behavior at low depletant concentrations: as the colloid concentration increases, the system transitions from a fluid to a rotator BCC crystal, and then to the sBCC crystal. The behavior with $\phi^{\mathrm{r}}_{\mathrm{dep}} = 0$ is in agreement with prior calculations of cuboctahedra phase behavior in Ref. [27]. At low $\phi^{\mathrm{r}}_{\mathrm{dep}}$, the fact that the F+R coexistence curve possesses a positive slope with increasing $\phi^{\mathrm{r}}_{\mathrm{dep}}$ indicates that a higher ϕ_{col} is needed for nucleation of the rotator BCC phase, which is what we observe from simulation. This reentrant phase behavior is a novel feature of cuboctahedra not readily observed in prior phase diagrams of hard spheres with depletion. The effect is not observed in Free Volume Theory [74] or direct simulations [85, 86], though it was predicted for perturbation theories of hard sphere systems [87]. In our present study, the low-ϕ_{col} branch of the F+R coexistence curve slopes to the right because our calculations of $\alpha = V_{\mathrm{free}}/V$ show that the rotator BCC crystal contains less V_{free} compared to the fluid phase at an identical density. We interpret these results as evidence that even low depletion concentrations will destabilize rotator phases of anisotropic particles.

For $q = 0.10$ (Fig. 2.3**a**), increasing the depletant concentration so that $0.05 \leq \phi^{\mathrm{r}}_{\mathrm{dep}} < 0.10$ will completely destabilize the rotator BCC crystal and bring about coexistence between a fluid and the sBCC crystal. When $0.10 \leq \phi^{\mathrm{r}}_{\mathrm{dep}} < 0.12$, we predict the fluid-SC coexistence to be stable as compared to the fluid-sBCC coexistence. Further increases to $\phi^{\mathrm{r}}_{\mathrm{dep}}$ cause the fluid-SC coexistence to become metastable under our predictions. We note that we do not observe the predicted stable sBCC phase in simulations at $\phi^{\mathrm{r}}_{\mathrm{dep}} > 0.12$, which could be a consequence of metastability or because the perturbative estimate for the metastability limit only represents a lower bound.

The reason for this predicted fluid-SC metastability is that high depletant concentrations favor denser packings. Though the sBCC crystal lacks V_{free} within the

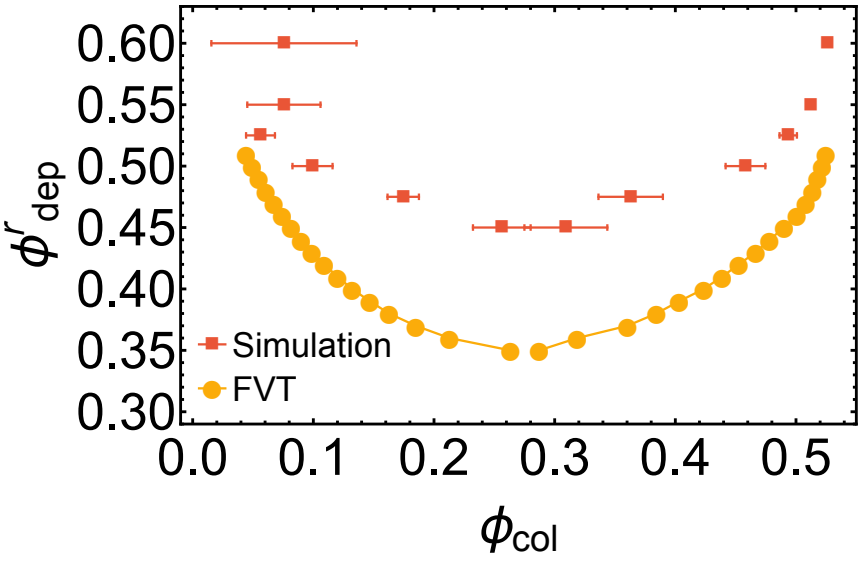

Figure 2.4: Coexistence curves for gas-liquid phase separation observed in simulation and predicted from Free Volume Theory. For the simulations, we employ a Gibbs ensemble with a total $N = 250$ cuboctahedra at an initial packing fraction $\phi_{col} = 0.275$. Simulation data was averaged across four independent runs. Image via Ref. [75]

crystal, the fact that it can pack more densely than the SC crystal means that it can maximize the amount of V_{free} outside of the crystal phase (Fig. 2.1**b**). These results indicate that performing a ground state analysis, i.e. the formal limit $n^r_{dep} \to \infty$ that only incorporates the depletant entropy as based on the amount of V_{free} in the system, will not properly resolve the phase behavior observed in our simulations. It is only by considering the entropy of the colloids that we are able to predict the stability of the simple cubic crystal. This contrasts recent work on the quasi-2D assembly of rounded cubes wherein a ground state analysis was sufficient in predicting phase behavior [64].

For $q = 0.25$ (Fig. 2.3**b**), the rotator BCC crystal destabilizes when $\phi^r_{dep} > 0.40$, and the fluid-sBCC coexistence is the dominant phase for high depletant concentrations. Our simulations and calculations differ on the critical ϕ^r_{dep} above which the fluid-sBCC coexistence is observed. Previous comparisons of Free Volume Theory to simulations show that Free Volume Theory tends to underestimate such critical

depletant concentrations [85]. Our calculations also predict a gas-liquid coexistence for a narrow range of depletant densities. We confirm this phase behavior with simulations in the Gibbs ensemble [88]. In this method, two systems are able to exchange volume and particles with one another, but the total volume and number of particles is held constant. The exchange of volume and particles ensures that the two linked systems will be at the same pressure and chemical potential. The results from these simulations are summarized in Figure 2.4. As we observed with fluid-crystal coexistence, theory tends to underestimate the critical depletant concentration needed for phase separation.

2.3.3 Effect on Directional Entropic Forces

The results presented so far speak to the system-wide behavior and the balance between colloid and depletant entropy. They do not, however, provide information on how depletion changes the behavior of the colloidal particles within their local environment. In order to understand these local environment changes, we have calculated the PMFT in the dense fluid state. The PMFT quantifies the *effective* forces on the cuboctahedra's facets arising from the system's entropy. These forces are scaled in terms of the thermal energy k_BT. We calculated the PMFTs on both the six large, square facets and the eight smaller, triangular facets by averaging across ten unique simulation trajectories at a density $\phi_{\text{col}} = 0.55$ before any noticeable crystals formed. The figures depict a two-dimensional slice through the first neighbor shell directly next to these facets. We ran these calculations for the two separate depletant-to-cuboctahedra size ratios, $q = 0.10$ and $q = 0.25$. For both ratios, we considered depletant concentrations that will lead to formation of a rotator crystal and a non-rotator crystal so as to capture the differences of the three separate self-assembly regimes.

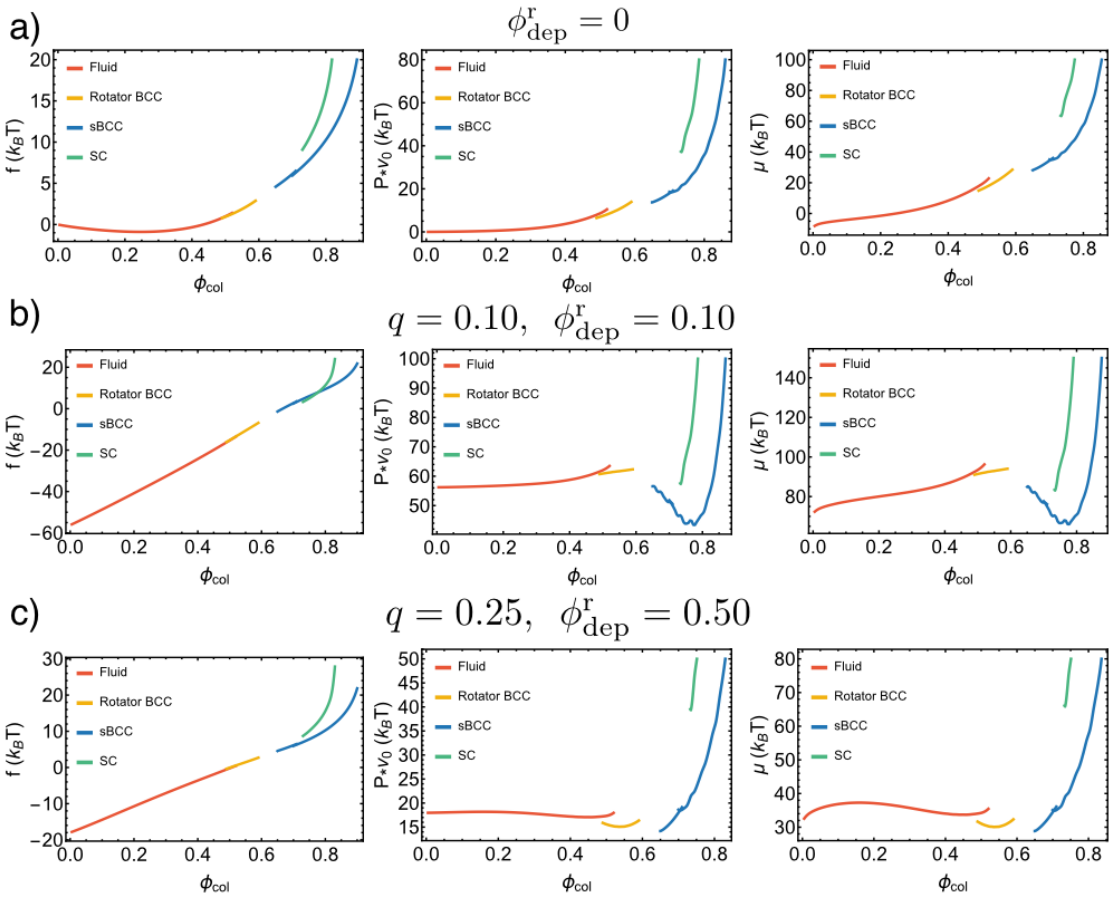

Figure 2.5: Plots showing the free energy density, pressure, and chemical potential in the fluid, rotator BCC, sBCC, and SC phases at different depletant conditions. **(a)** With no depletants, the SC phase is never stable and the sBCC phase is only stable at high ϕ_{col}. **(b)** At $q = 0.1$ & $\phi^{\mathrm{r}}_{\mathrm{dep}} = 0.10$, the fluid-SC coexistence becomes stable. **(c)** At $q = 0.25$ & $\phi^{\mathrm{r}}_{\mathrm{dep}} = 0.50$, the system will phase separate into a fluid and sBCC crystal. Image via Ref. [75]

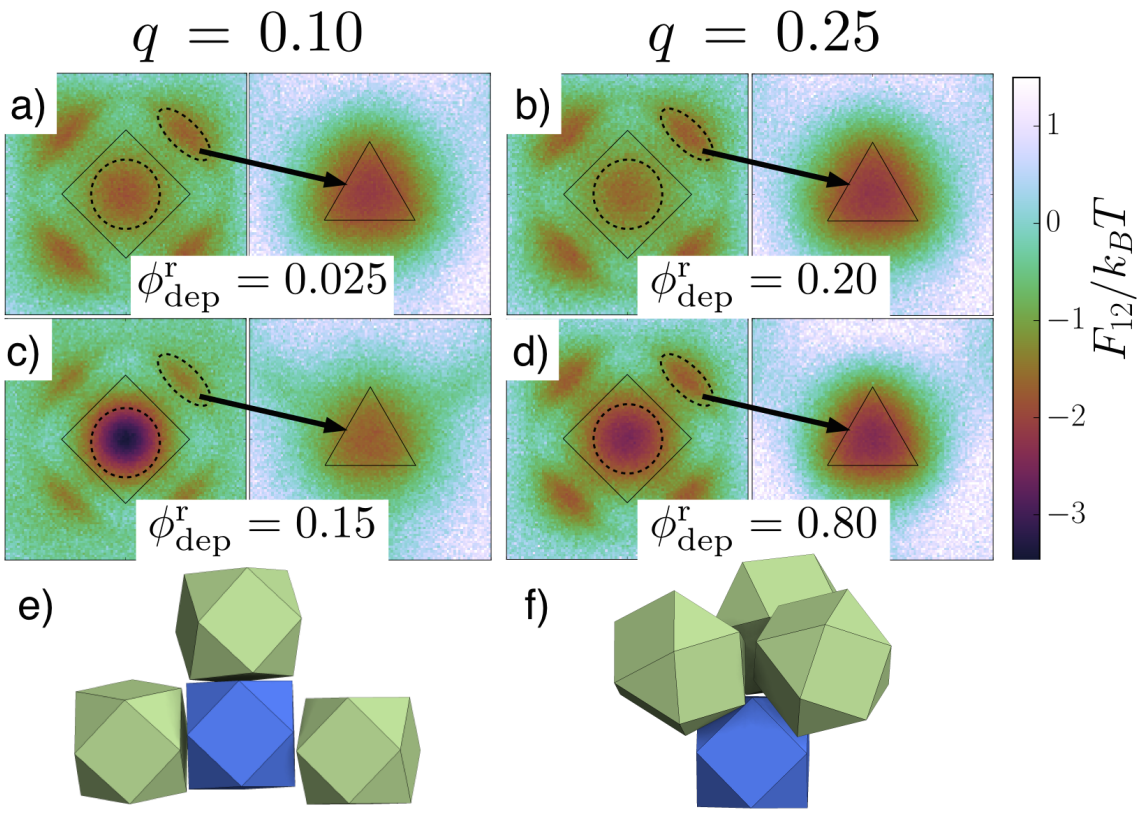

Figure 2.6: 2D slices of the PMFT through the first neighbor shells located next to both the square and triangular facets of the cuboctahedra for various depletant conditions. Calculations were performed for system sizes of $N = 1000$ at $\phi_{\mathrm{col}} = 0.55$. Each column uses depletants of different sizes, with $q = 0.10$ in the left column and $q = 0.25$ in the right column. For the PMFT across the square facet, it is possible to see the energy well along one of the square facets as well as four energy wells associated with different triangular facets. For the PMFT along the triangular facet, only the single energy well is visible. **(a & b)** Under conditions that lead to formation of a rotator BCC crystal, the DEFs along the square facets are $> -2\,k_BT$, and the DEFs along the triangular facets are $\approx -2\,k_BT$. **(c)** For conditions that lead to formation of the SC crystal, the average DEFs are $-3.2k_BT$ at the center of the square facets and $-1.7\,k_BT$ at the center of the triangular facets. **(d)** For conditions that lead to formation of the sBCC crystal, the average DEFs are $-2.4\,k_BT$ at the center of the square facets and $-2.3\,k_BT$ at the center of the triangular facets.**(e & f)** Representative configurations for a reference particle (blue) and a selection of its nearest neighbors (green). **(e)** The low coordination bonding along the large facets that is more likely to occur when $q = 0.10$. **(f)** The high coordination bonding that occurs when $q = 0.25$ and which leads to sBCC crystal nucleation. Image via Ref. [75]

Figure 2.6 illustrates how the emergent DEFs that lead to crystal assembly depend upon the depletant conditions. In Figures 2.6**(a & b)**, the PMFT shows only moderate DEFs at both the square and triangular facets. At these low depletant densities, the driving force for facet alignment is weak. In Figure 2.6**c**, the high depletant concentration for $q = 0.10$ leads to significantly stronger DEFs at the square facets and a reduction in DEFs at the triangular facets; thus there is a strong driving force for the square facets to align. In the conditions that will lead to the sBCC crystal depicted in Figure 2.6**d**, the DEFs on the square facets increase substantially while there is also a slight increase in the forces on the triangular facets. These conditions make alignment along all facets more favorable as compared to the depletant-free system.

From analyzing these PMFTs, we infer that depletion can change the effective particle shape when we consider hard particle assembly as being driven by directional entropic forces. As a general rule, increasing the size of a particle facet increases the strength of its directional entropic forces [67, 69, 68]. Since depletion increases the amount of crowding in the system, it is no surprise that the addition of depletants can increase DEFs and hence make particles have effectively larger facets. However, it is a remarkable result that depletants increase the DEFs on the large facets while decreasing the DEFs on the smaller facets. In this manner, depletants have the ability to make cuboctahedra effectively behave as cubes.

2.4 Conclusion

The ability to adjust bonding specificity via depletion size has ample opportunity to be used in controlling colloidal assemblies. van Anders et al. [69] showed how increasing the facet size of truncated spheres will increase the specificity of DEFs.

Here we achieve a similar effect in a different way: by adjusting depletant size, with smaller depletants increasing the specificity of DEFs. Thus, depletion can alter the effective shape of anisotropic particles due to the enhanced anisotropy of the DEFs with small depletants. We expect this knowledge to be useful for experiments because it is far easier to adjust assembly behavior by adding depletants or shrinking/swelling polymer coils compared to producing particles with a shape that can be varied *in situ*. We stress that the trends we observe with cuboctahedra are not likely to depend on the penetrable hard sphere model of depletion used here, and we would expect similar results for other models such as hard sphere depletants[80], soft depletants [89], or interacting polymers [85, 90]. Our results show how the entropic assembly of anisotropic particles is affected by a second component with a variable concentration and characteristic length. The additional design knobs presented by depletion interactions promise to be simple, powerful tools to increase assembly possibilities of faceted particles.

CHAPTER III

Shape Modifications and Their Effect on Directional Entropic Forces

The contents of this chapter are adapted from two different publications. This chapter focuses on the contributions of A.S. Karas in these publications. The material on chiral crystals appeared in *Physical Review Letters* in a paper authored by P.F. Damasceno, A.S. Karas, B.A. Schultz, M. Engel, and S.C. Glotzer [91]. The material on the optimal shape for diamond formation appeared in *ACS Nano* in a paper by G. van Anders, D. Klotsa, A.S. Karas, P. Dodd, and S.C. Glotzer. Figure 3.1 was prepared by P.F. Damasceno, Figure 3.3 was jointly prepared by P.F. Damasceno and A.S. Karas, and Figures 3.2, 3.4, and 3.5 were prepared by A.S. Karas.

3.1 Introduction

Because experimentalists can control nanoparticle shape, it is useful for computer simulations to inform the effect of shape on the self-assembly of those particles. Control over particle shape can be achieved through means such as growing silver nanocrystals and stabilizing specific facets with capping polymers [92], through the length and rigidity of ligands attached to cubes [93], and through silica deposition on hematite cubes [64]. Computer simulation has informed both self-assembly and packing behavior for polyhedra systems continuously adjusted in their shape [27, 67,

94]. Changes in shape can lead to either first-order or continuous transitions in terms of the equilibrium crystal structure [95].

One way of thinking about the role of shape change is how it affects the entropic bonds that particles form. van Anders *et al.* introduced the idea of a controllable, entropic valence resulting from the introduction of facets to a sphere [69]. This chapter is based on work in a similar vein in that I consider how discrete changes in particle shape affect DEFs and the self-assembly propensity. In this chapter, I describe the effect of shape change on two types of systems: the rounding of a chiral Voronoi particle and the truncation of a tetrahedron. I pay particular attention to how shape impacts the entropic valence in these systems, using the PMFT to quantify this effect.

3.2 Results and Discussion

3.2.1 Effect of Rounding on Chiral Crystal Assembly

This section focuses on the ability of rounded Voronoi particles (VPs) [96] to self-assemble the simple chiral cubic (SCC) crystal [91]. Figure 3.1 provides an example of an assembled SCC. The VP of SCC is primarily composed of six large facets, and the assembly of the target SCC crystal is reliant on each of the facets aligning with a corresponding facet from a neighboring particle. Intuitively, it is known that a maximally rounded particle that approaches the shape of a sphere will behave in the same way as a sphere. Here, I seek to find the rounding levels at which the shape stops acting like the original VP and when it begins to behave like a sphere. In order to study the effect of shape, I perform self-assembly simulations at various densities and levels of rounding. I define the rounding level through the isoperimetric quotient (IQ). IQ is a ratio between particle volume, V, and surface area, S, that measures how close a shape is to a sphere. IQ is defined as: $IQ = \frac{36\pi V^2}{S^3}$.

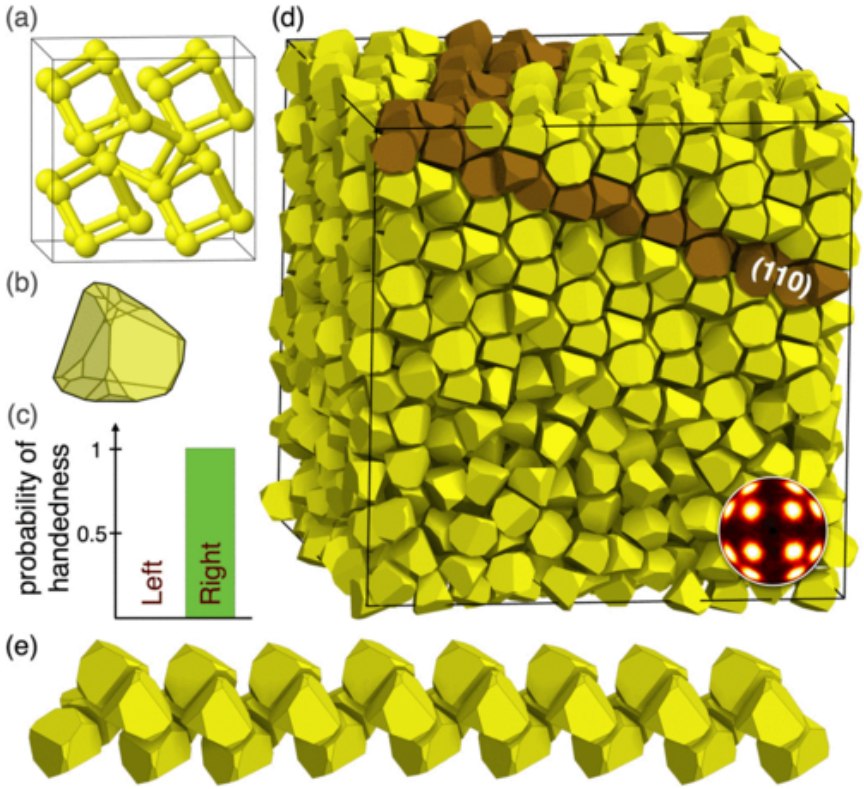

Figure 3.1: Assembly of the simple chiral cubic (SCC) crystal structure from its VPs. **(a)** A 2-by-2 patch of the unit cell with 4 particles. The bonds indicate chiral square helices (pitch length four). **(b)** A single VP with its six symmetry-equivalent big faces. **(c)** The assembled crystal is homochiral with handedness determined by the building block. **(d)** A snapshot of the assembled crystal structure. **(e)** A right-handed helix cut out from the assembled crystal. The VPs align their big faces in the square helix [see (a)]. As the crystal is cubic, similar square helices are found along the other two fourfold axes. This figure was prepared by Pablo Damasceno and appeared in Ref. [91].

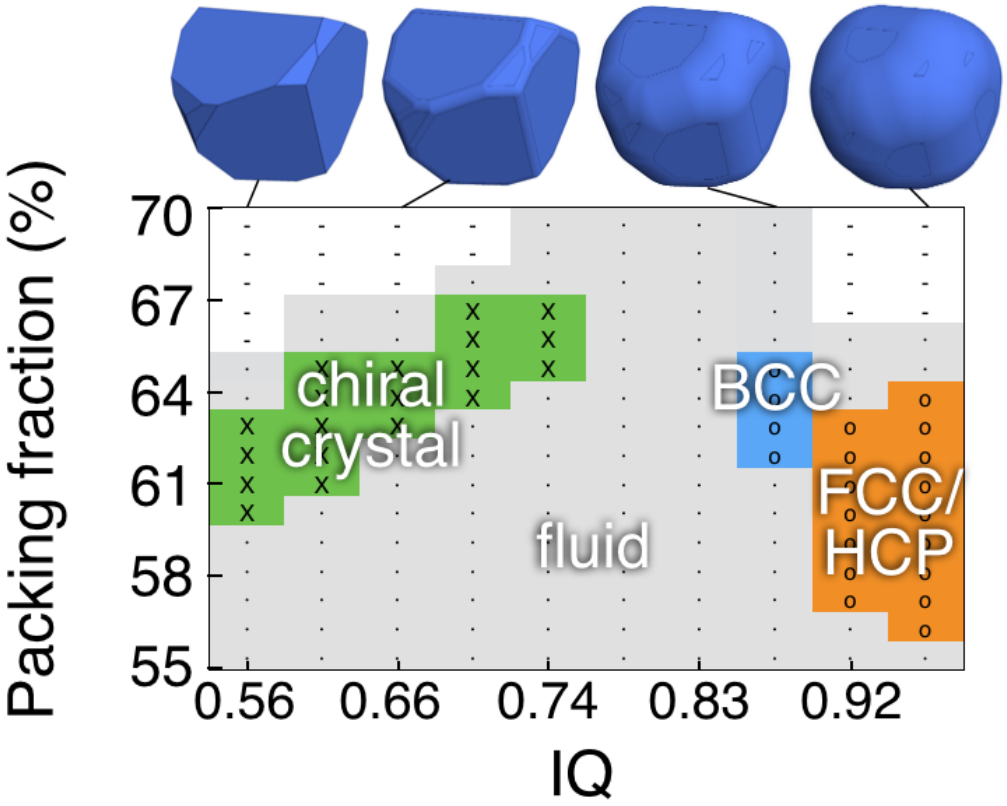

Figure 3.2: Phase diagram for the self-assembly of rounded chiral VPs as a function of rounding level and packing fraction. IQ is the Isoperimetric Quotient, a measure of how similar a shape is to a sphere based on the ratio between surface area and volume. Grey regions denote packing fractions for which no assembly was achieved. Green, blue and orange regions denote simulations where SCC, body-centered cubic (BCC) and face centered cubic (FCC) assemblies were observed, respectively. As roundedness increases, higher densities are required for assembly of the SCC. This figure was prepared by Andrew Karas and appeared in the supplementary information in Ref. [91].

Figure 3.2 summarizes the results of the self-assembly propensity as a function of shape. For low levels of rounding, it is possible for the rounded shape to form the SCC. Higher packing fractions are needed in order to induce the SCC assembly with these rounded shapes. An interpretation of this result for small rounding levels is that as facet size decreases, increased crowding (in the form of a higher system density) is required for the DEFs to be strong enough for self-assembly.

When the level of rounding increases beyond $IQ > 0.74$, the rounded VPs do not self-assemble the SCC crystal. For the moderately rounded shapes with $0.78 \leq IQ \leq 0.83$, no ordered structures forms. As the rounding further increases, BCC and FCC phases result from self-assembly. BCC and FCC assemblies are characterized by higher coordination numbers (14 and 12 for BCC and FCC, respectively, while the SCC has a coordination number of 6) and correspondingly less alignment of the facets. Such high coordination phases are associated with weaker DEFs [69].

The results from the single-component self-assembly simulations demonstrate how changes to particle shape control structure formation. In the spirit of materials-by-design, one might wonder if it is possible to control assembly such that a single particle can form different structures based on the environment. As one might suspect from section 2.3.1 and as Fig. 3.3 illustrates, depletion can induce the assembly of the SCC phase in particles that would otherwise form an achiral, plastic crystal. I find that a rounded VP with $IQ = 0.87$ is capable of forming the SCC in simulations with penetrable hard sphere depletants having a radius one tenth of the rounded VP's circumscribing sphere.

In order to describe how changes to shape and the addition of depletion changes the DEFs in these systems, I compute PMFTs as shown in Fig. 3.4. Rounding of the shape (and thus decreasing facet size) has the effect of spreading out the forces across

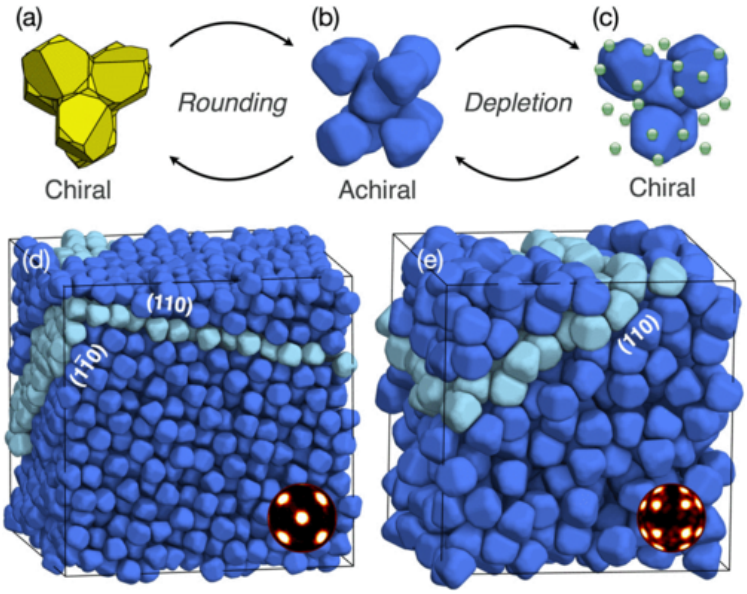

Figure 3.3: The effects of rounding and depletion can be used to modulate between the SCC and a plastic crystal. The original, non-rounded VP **(a)** assembles the chiral crystal. Rounding the edges and vertices **(b)** results in an achiral crystal, but introducing depletants to the rounded VPs **(c)** can induce the specific interactions needed for the chiral crystal. **(d)** An example of the plastic BCC crystal formed with no depletants, and **(e)** the SCC that assembles with depletion effects. Image via Ref. [91]

the entire facet rather than localizing forces at the facet center. Further rounding significantly weakens the strength of the forces and spreads them much more evenly across the shape when a plastic crystal is formed with $IQ \geq 0.87$. Depletion re-strengthens the DEFs on the facets. In this way, depletion is able to restore the chiral valency that was lost with the rounding of the shape.

3.2.2 Effect of Truncation for Optimizing Local Neighborhood for Diamond Self-Assembly

This next section focuses on systems of truncated tetrahedra which are known to form diamond crystal structures. Digital alchemy is a technique for finding optimal particle attributes through computer simulation. In Ref. [72], a test case for digital alchemy is finding the best truncation of a tetrahedron for diamond formation. While digital alchemy can identify *what* is optimal, it does not explain *why* something is optimal. In this work, I set out to explain why a shape is optimal in terms of its

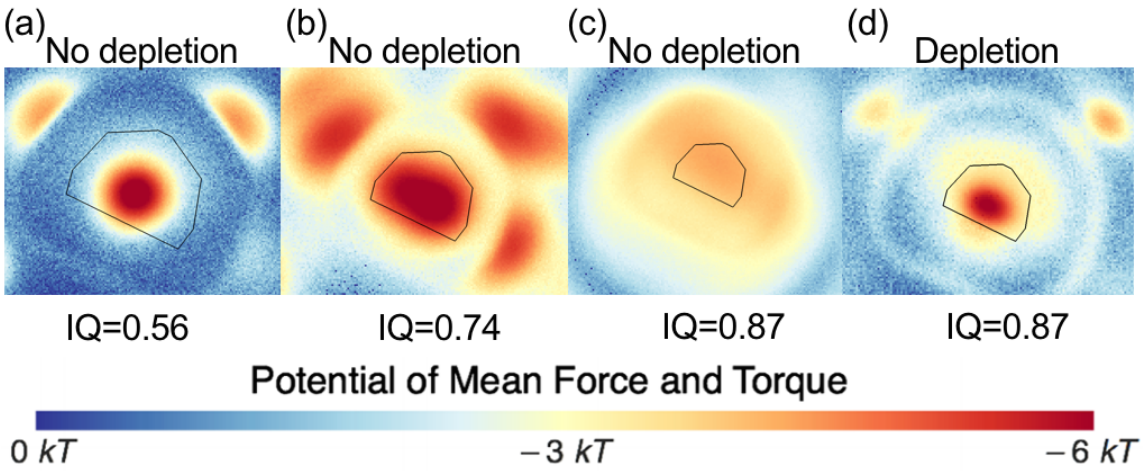

Figure 3.4: Examples of the Potential of Mean Force and Torque (PMFT) opposite a facet for different conditions. **(a)** For the non-rounded VP, the DEFs as computed by the PMFT are strongly localized at the center of the facet location. **(b)** For the most rounded shape that self-assembled the SCC without depletion, the forces at the facet are still strong though they have become more spread out across the facet as compared to **(a)**. **(c)** When the plastic BCC crystal forms in the absence of depletion, the strength of the DEFs are significantly weakened corresponding with a diminished probability of the facet aligning with a neighboring particle. **(d)** When using depletion with the same shape as in **(c)**, the forces are strengthened and re-localized at the facet center. All the PMFTs were obtained at the lowest densities at which each crystal was observed to self-assemble. Image adapted from Ref. [91]

directional entropic forces.

The formation of a diamond crystal structure from hard particles relies on the formation of specific entropic bonds. There are two primary considerations of the bonding environment that accounts for some shapes being better diamond formers than others. In diamond, the truncated dodecahedra must form four nearest-neighbor bonds. This consideration prefers larger facets (and thus lower truncation levels). However, the non-truncated tetrahedra cannot exist in diamond at densities $\phi \geq 0.50$ because the vertices would overlap with a next-to-nearest neighbor. These steric hindrances put an upper bound on the optimal facet size.

Figure 3.5 compares the optimal shape for diamond against two different non-optimal shapes. In the crystal phase, the optimal facet leads to lower free energies for the entropic bonding locations in diamond. The comparison in the fluid phase at density $\phi = 0.5$ against a tetrahedron is also enlightening. In Fig. 3.5 **c** & **d**, the PMFT is displayed for a slice through the next-to-nearest neighbor well. For the shape capable of forming diamond, the location of the free energy wells (the cyan spots) is in the necessary position for diamond. For a tetrahedron, these wells are rotated by $\pi/6$ which means that the next-to-nearest neighbors cannot be arranged in diamond. In this way, the optimal shape can be seen as the one that best dictates the valence for diamond formation.

3.3 Conclusion

I have shown the effect of facet size on the directional entropic forces in two types of systems through the use of a PMFT. When rounding the edges of a Voronoi particle that assembles its target structure because of six strong entropic bonds, low levels of rounding require higher densities to induce DEFs sufficiently strong for assembly.

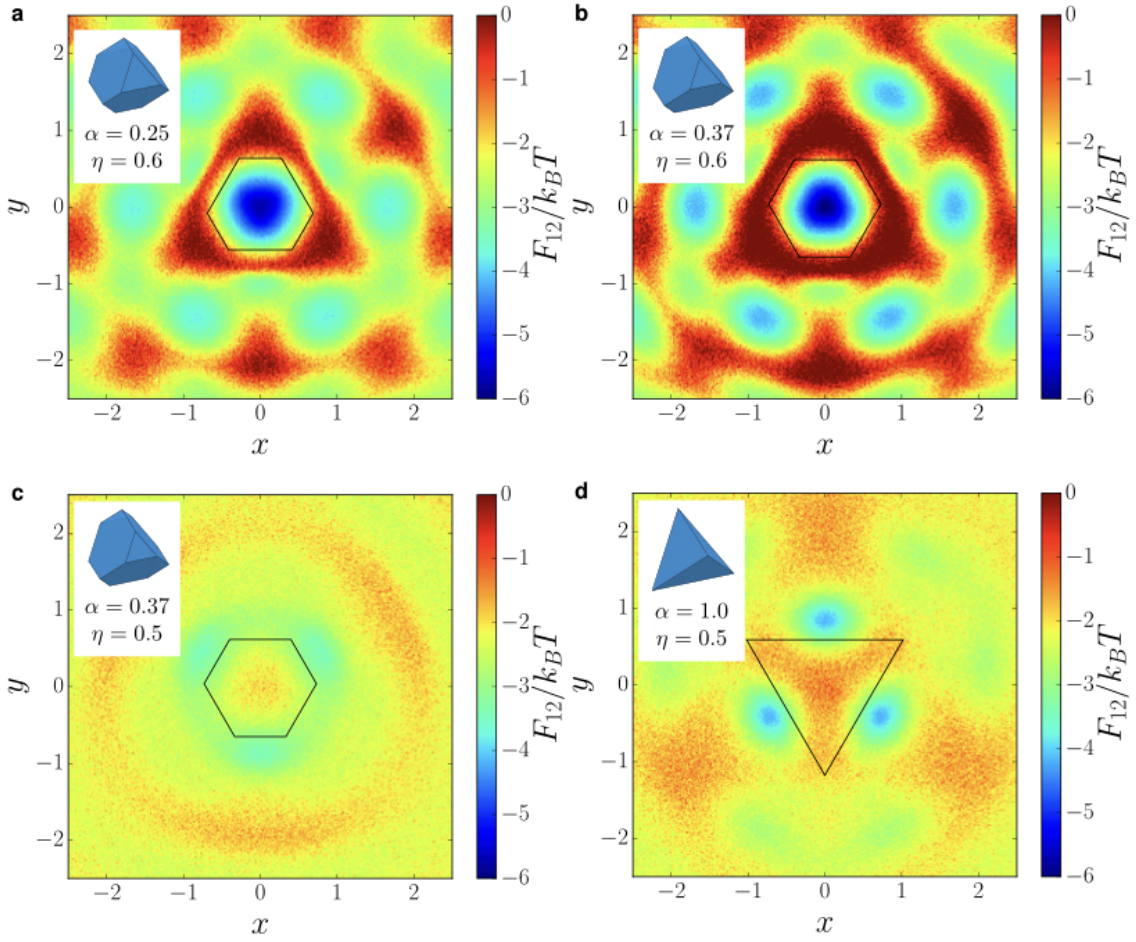

Figure 3.5: Emergent valence encoded in the PMFT for truncated tetrahedra for a crystal at density $\phi = 0.6$ (a: $\alpha = 0.25$, b: $\alpha = \alpha^* \approx 0.37$) and a fluid at density $\phi = 0.5$ (c: $\alpha = \alpha^* \approx 0.37$, d: $\alpha = 1.0$). In the crystal we see that the particle at the optimal truncation α^* (b) shows greater specificity of tetrahedral valence than at lower α (a), as expected. However, at fluid densities, we see that if the particle is too tetrahedral (d), the second neighbor shell is rotated by $\pi/6$ compared with lower truncations (c) and is incommensurate with the diamond lattice. Image via Ref. [72]

Higher levels still of rounding will result in plastic crystals with significantly weaker DEFs. Depletion strengthens the DEFs and induces the assembly of the chiral crystal instead of the plastic crystal. I have also computed the PMFT in systems of truncated tetrahedra in order to explain why an optimal shape is better than others for forming a diamond crystal. In order to induce DEFs that best support the entropic valence for diamond, there need to be four large facets. However, when facets are too large the next-to-nearest neighbors will not be properly arranged.

CHAPTER IV

Properties of Plastic Crystals and Their Phase Behavior

The contents of this chapter are adapted from an in-progress manuscript being prepared by A.S. Karas, J. Dshemuchadse, G. van Anders, and S.C. Glotzer.

4.1 Introduction

Anisotropic molecules, colloids, and hard particles are known to exhibit two types of thermodynamically stable mesophases between a liquid and a crystal: the liquid crystal and the plastic crystal. The liquid crystal, in which particles have orientational order but lack long-range translational order, has been thoroughly studied for many kinds of systems [23, 97, 98]. Much less is known about the plastic crystal, in which particles have translational order but lack long-range orientational order. Our understanding of plastic crystals originates from observations of molecular systems. In 1930, Pauling presented a statistical mechanics argument explaining how molecules in a crystalline phase could undergo a transition from oscillatory motion to rotational motion as a way to explain temperature-dependent phenomena in thermodynamic properties [99]. Timmermans later coined the term 'plastic crystal' to describe phases formed by globular compounds which are far easier to deform than lower-temperature phases [100]. These plastic crystal phases typically have cubic symmetry, they lead to a significantly lower entropy of melting as compared to non-

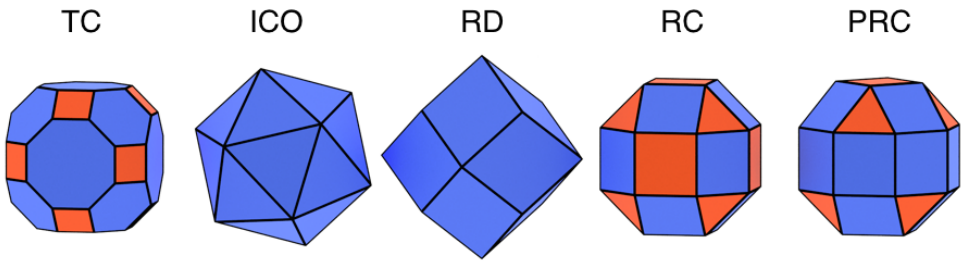

Figure 4.1: The five shapes used in the study: Truncated Cuboctahedron (TC), Icosahedron (ICO), Rhombic Dodecahedron (RD), Rhombicuboctahedron (RC), and Pseudorhombicuboctahedron (PRC). We are able to identify that some facets are more important than others in dictating how neighbors align with respect to one another: the relevant bonding facets are shown in blue, and the other facets are colored red.

globular compounds, and they can form with many different organic or inorganic systems [101, 102]. It is also possible to quench a plastic crystal into an orientational glass wherein the system maintains a higher-symmetry unit cell, the rotational motion undergoes a vitrification process, and long-range orientational order is absent [103, 104, 105, 106].

Entropic plastic crystals have recently been reported in systems of nanoparticles [66, 63] and in computer simulations of hard particles [25, 26, 54, 27, 55, 56]. Existing literature on Monte Carlo simulations shows that hard particle plastic crystals are a thermodynamic state distinct from the orientationally ordered crystal phase [25, 55], that plastic crystals are typically formed by spheroidal particles [25, 26, 55], that the existence of a plastic crystal phase lowers the free energy barrier for crystallization from a fluid [56], and that particle orientations in the plastic crystal phase are not random but rather some orientations are more likely to occur than others [55, 56, 107]. The recent development of the theory of directional entropic forces [67, 69] and the quantification of these forces through the potential of mean force and torque (PMFT) [68] provide a new approach to the analysis of plastic crystal systems.

Here, we observe the development of orientational order in hard particle systems

that form plastic face-centered cubic (pFCC) crystals. We develop new techniques that allow us to characterize the orientational coupling in orientationally ordered and disordered states. We study five shapes that all form pFCC crystals, but exhibit different plastic crystal-to-crystal transitions: first-order phase transitions, continuous orientational order development without a thermodynamic phase transition, and an approach to an orientational glass transition. Fig. 4.1 shows the shapes investigated, and Fig. 4.2 shows the phases that they form. We develop an order parameter based on the similarity of particle orientations within a system as compared to those of a perfect crystal. The order parameter captures the discontinuous change in orientational order across a first-order transition for shapes of arbitrary symmetry. We characterize the local environments of particles by calculating the potential of mean force and torque and orientational-orientational correlations between a reference particle and its neighbors. Through this analysis, we identify the relationship between relevant shape features and plastic crystalline behavior. We also use rotational autocorrelation functions to reveal the dynamical behavior of particle orientation as a function of density.

4.2 Model and Methods

We focus on five shapes that each self-assemble FCC crystals at moderate densities: truncated cuboctahedron (TC), icosahedron (ICO), rhombic dodecahedron (RD), rhombicuboctahedron (RC), and pseudorhombicuboctahedron (PRC; also known as the elongated square gyrobicupola). Particle shapes are depicted in Fig. 4.1. We will show below that, based on the size and location of a shape's facets, some facets are more important than others for the formation of entropic bonds [73], and play a key role in disrupting plastic crystal behavior. These facets are colored blue in Fig.

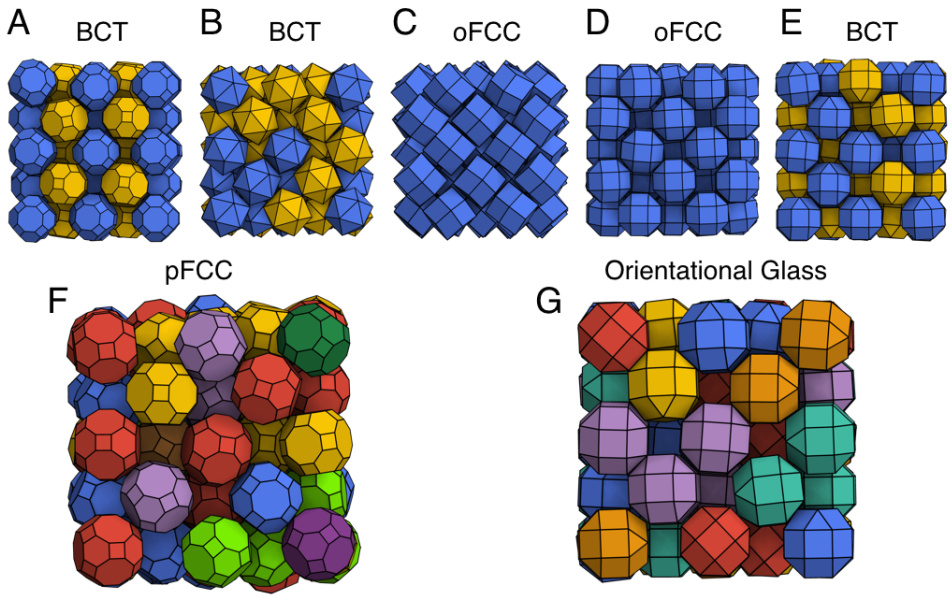

Figure 4.2: Representative images of different phases studied in this work, with particles colored based on their orientation. (**a**–**e**) The high-density phase for each shape. (**a & b**) Both TC and ICO form BCT crystals upon compression of the pFCC. (**c & d**) RD and RC maintain FCC order, but they develop strong orientational order and exist in this ordered FCC (oFCC) at high density. (**e**) PRC can pack in a BCT crystal, however this phase is not readily accessible *via* self-assembly. (**f**) An example of the plastic crystal formed by TC. Note that some orientations are more prevalent than others, but long-range orientational order does not exist. (**g**) The orientational glass formed by PRC contains particles in one of six distinct orientations. Unlike in a plastic crystal, particles cannot readily change their orientation.

4.1. TC has six octagonal facets and eight hexagonal facets which primarily drive the entropic bonding plus an additional 12 square facets. ICO is a Platonic solid with 20 identical triangular facets. RD is the Voronoi particle [96] for FCC, and thus tiles space. Its 12 facets align with the nearest-neighbor directions of the FCC crystal. RC can be constructed from truncation of RD's vertices, leaving 12 square facets that align with the FCC environment, plus an additional 6 square and 8 triangular facets from the truncations. The 12 facets that align with the FCC environment are the most important ones for entropic bonding. PRC is a Johnson solid with the same number and types of facets as RC, but the facets are arranged differently to produce a reduced, tetragonal symmetry. One can construct PRC from RC by taking a square cupola portion of RC and rotating it by 45°. While RC has a set of 12 square facets that align with all bonding directions in an FCC environment, only eight square facets of PRC can align with the FCC bonding directions at a given time. The remaining directions line up with four triangular facets.

We use a number of techniques to characterize the behavior of plastic crystals and their phase transitions. We perform all simulations with the hard particle Monte Carlo (HPMC) package of HOOMD-blue [29, 30, 31]. We compute the equation of state as the primary indicator of phase behavior. Systems with $N = 864$ particles were simulated in a floppy-box NVT ensemble with the volume kept constant while allowing for box shearing and changes in box aspect ratios [108]. We compute pressure *via* the scale distribution function (SDF) in HPMC [31]. For systems that exhibit evidence of first-order transitions in NVT simulation, we validate the character of the putative transition through NPT simulations for systems of $N = 2048$ to test for the existence of hysteresis. We present data using the reduced pressure $p^* = \beta p v_0$ where $\beta = (k_B T)^{-1}$ and v_0 is particle volume. Data were collected by

both compressing the system from a pFCC crystal and expanding the system from a dense crystal with long-range orientational order. We note that we do not necessarily initialize expansion simulations from the densest packing (except for RC and RD, which pack most densely in an FCC lattice). Instead, we initialize the systems in body centered tetragonal (BCT) phases that were found to form via compression of the plastic crystal phase. We find that densest packing phases do not readily arise from the plastic crystal phases. The BCT phases used for initialization each have a two-particle unit cell wherein the particles have different orientations.

We quantify global orientational order by measuring the orientation of particles relative to global reference orientations. To do so, we note that if we represent particle orientations as quaternions, the difference in orientation between a particle described by an orientation q_0 to a reference orientation q_{ref} is given by

$$Q_{net} = q_{\text{ref}}^{\dagger} q_0 = \exp(\frac{i}{2}\theta\hat{n}\cdot\vec{\sigma}) = \cos(\frac{\theta}{2}) + i\hat{n}\cdot\vec{\sigma}\sin(\frac{\theta}{2}) \,, \tag{4.1}$$

where we use Pauli matrices $\vec{\sigma}$ to give an explicit representation of the rotation of an angle θ in a plane perpendicular to $\hat{n}$. The trace of $\frac{1}{2}\text{Tr}(Q_{net})$ is a global rotational invariant with values between -1 and 1.

To construct the order parameter, we first select a set of q_{ref} from a set of j quaternions corresponding to orientations found in the dense, orientationally ordered crystal ($j = 1$ for RD and RC, and $j = 2$ for TC, ICO, and PRC). Next, we determine the average $\text{Tr}(Q_{net})$ for a randomly oriented particle, which we denote by Ψ_r, by integrating over the group manifold of SO(3) modulo the particle's point group symmetry Γ,

$$\Psi_r = \frac{1}{2}\int_{SO(3)/\Gamma} dq \max_j \text{Tr}(q_{\text{ref},j}^{\dagger}, q) \tag{4.2}$$

For simplicity, we compute Ψ_r *via* Monte Carlo integration by sampling 500,000 random quaternions. We compare Ψ_r against the quantity

$$\Psi_s = \frac{1}{2N} \sum_{i}^{N} \max_{j} \mathrm{Tr}(q_{\mathrm{ref},j}^{\dagger}, q_i) \ , \tag{4.3}$$

which we measure when simulating dense systems of shapes. From this, we construct the order parameter

$$\Theta = \frac{\Psi_s - \Psi_r}{1 - \Psi_r} \ . \tag{4.4}$$

For a crystal with perfect global orientational order, $\Theta = 1$ since for each particle q will be one of the $q_{\mathrm{ref},j}$ and so $\Psi_s = 1$ by construction, and for a crystal with random orientations, $\Theta = 0$.

We use this measure to define how similar, on average, a system's orientations are to those of a perfect, dense crystal. This order parameter shares similarities with the frequently used cubatic order parameter [25, 55, 109, 110], but it differs in a few key respects. Most notably, it does not require that the particles have cubic symmetry. In addition, this order parameter does not compare the orientation of all particles against a single, global orientation.

We calculate the potential of mean force and torque (PMFT) to show how the local particle environments depend on particle shape and system density. The PMFT, which we compute with the *freud* software toolbox [111], uses a three-dimensional probability distribution function to determine the free energy associated with a neighboring particle in some position relative to a fixed orientation for a reference particle. Thus, when particles freely rotate between all orientations with an equivalent likelihood, there are no preferred locations for neighboring particles relative to the freely rotating reference particle. Isotropic free energy isosurfaces in the PMFT result from such free rotations. When particles adopt preferred relative orientations, *e.g.*,

facet-to-facet, an anisotropic PMFT results, revealing the distribution of directional entropic forces (DEFs) [69, 68].

To further describe the orientational order present in the particles' local environments, we calculate the relative misalignment of neighboring particles to provide a one-dimensional representation of orientation-orientation coupling of nearest neighbors. We compute the minimum angle required to rotate a particle into an orientation identical to each of its neighbors, and we represent this information as a histogram. The angle separating two orientations is extracted as laid out in Eqn. 4.1, and we check against equivalent orientations based on the point group symmetry. By measuring this orientation-orientation coupling, we can identify when neighboring particles tend to align with parallel orientations, when they take on orientations that span specific angles, or when they appear to adopt random orientations with respect to one another.

The dynamics of particle translations is frequently characterized through the self-part of the intermediate scattering function, which is the Fourier transform of the Van Hove function. To characterize rotational dynamics, we seek a similar description, however, whereas the space of possible translations is described by $\mathbb{R}$, the space of possible rotations is described by the manifold of the rotation group, SO(3), requiring a different form of Fourier transform. For convenience, we note that SU(2) is the double cover of SO(3), and that SU(2) has the group manifold S^3, so we can study rotational dynamics by doing a Fourier transform in terms of spherical harmonics on S^3. In particular we define

$$F_l(t) = \frac{1}{N} \sum_i \sum_{m_1 m_2} Y^*_{l m_1 m_2}(0) Y_{l m_1 m_2}(q_i(0)^\dagger q_i(t)) \ , \tag{4.5}$$

where $Y_{l m_1 m_2}$ are spherical harmonics, q_i is the orientation of particle i, and m_1 and m_2 are magnetic quantum numbers.

To compute $F_l(t)$ we used conventions for $Y_{lm_1m_2}$ similar to those given in Ref. [112]. In particular, we embed S^3 in $\mathbb{R}^4$ using the complex coordinates ξ and ζ. For a unit quaternion defined by $q = w + xi + yj + zk$, we follow Ref. [112] and use the parameterization:

$$\begin{aligned} \xi &= x + iy \\ \zeta &= z + iw \end{aligned} \tag{4.6}$$

If we sum over all possible quantum numbers and use $a = -(m_1 - \frac{l}{2})$ & $b = -(m_2 - \frac{l}{2})$, we represent the spherical harmonics by summing over all non-negative exponents for the following expression [112]:

$$Y_{l,\frac{l}{2}-a,\frac{l}{2}-b} = \sqrt{\frac{a!(l-a)!b!(l-b)!}{l+1}} \sum_k \frac{(\xi^*)^k \zeta^{b-k} (\zeta^*)^{a-k} (-\xi)^{l+k-a-b}}{k!(l+k-a-b)!(a-k)!(b-k)!} \,. \tag{4.7}$$

4.3 Results

4.3.1 First-Order Transitions

Two of the shapes that we investigate (TC and ICO) show a first-order transition from a plastic crystal to a crystal. Such first-order transitions upon compression of the plastic crystalline phase have been observed in related work [54, 55]. An apparent hallmark of these transitions is a change in orientational order that coincides with a change in translational order. For both TC and ICO, we find that compression of the pFCC crystal leads to formation of a BCT structure with two preferred particle orientations in the unit cell. The preferred orientation of the crystal directly determines the unique axis of the simulation box as it undergoes tetragonal symmetry breaking. For TC, the BCT structure shows strong orientational order wherein the two particle orientations repeat in a specific manner. Systems of ICO show weaker orientational order wherein the BCT phase leads to particles preferentially adopting

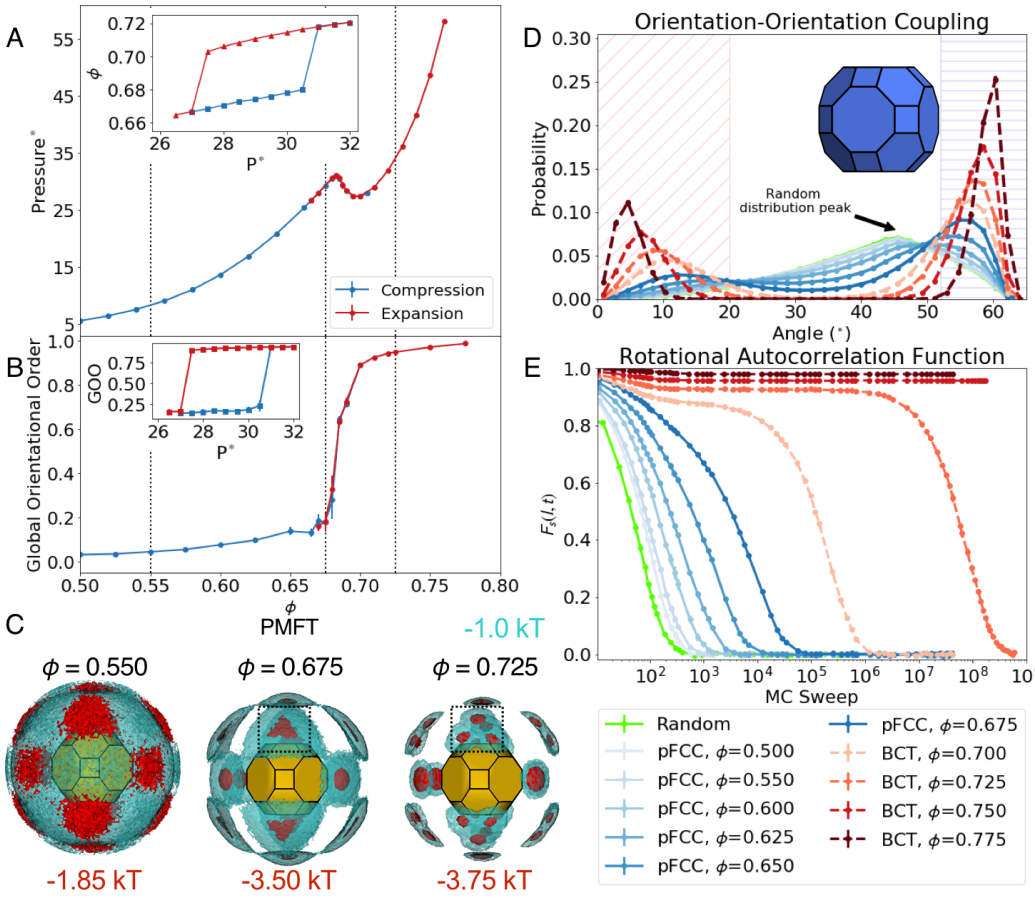

Figure 4.3: Phase behavior of the truncated cuboctahedron (TC). **(a)** The equation of state shows a van-der-Waals loop in the NVT ensemble (main plot) and hysteresis between the pFCC crystal and the BCT crystal in the NPT ensemble (inset). Both of these features indicate a first-order transition. **(b)** The orientational order parameter displays a mild increase within the pFCC phase and is significantly higher in the BCT phase; it also exhibits hysteresis in the NPT ensemble (inset). **(c)** PMFTs at three state points. As the density increases in the plastic crystal phase ($\phi = 0.550$ & $\phi = 0.675$), the strength of the primary bonding wells increases, but the basic shape persists and the higher free energy isosurface ($-1k_BT$) remains connected. After the transition to a BCT phase ($\phi = 0.725$), the bonding wells at the hexagonal facets split into three unique minima (see dashed-line box), and the $-1k_BT$ isosurface does not connect across the different wells. **(d)** The plot of the orientation-orientation coupling as a function of density shows the development of two peaks. In the BCT crystal, neighboring particles either have similar orientations (separated by $< 20°$, marked with red diagonal lines in the background) or they exhibit a misalignment close to 60° (marked with blue horizontal lines in the background). This trend develops in the pFCC phase and strengthens after the transition to the BCT crystal. **(e)** The rotational autocorrelation function shows a relatively steady decay in the pFCC crystal, and an initial plateauing before an eventual decay in the BCT crystal.

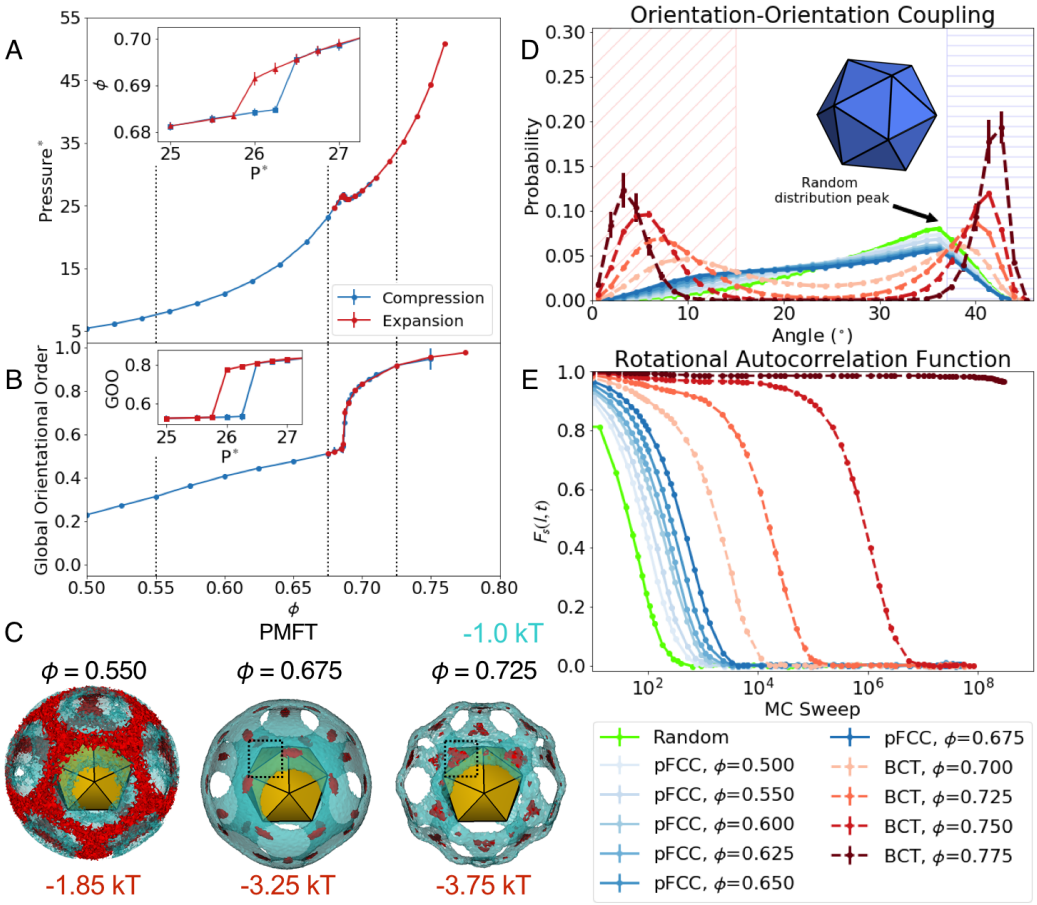

Figure 4.4: Phase behavior of the icosahedron (ICO). **(a)** The equation of state shows a small van-der-Waals loop in the NVT ensemble (main plot) and hysteresis between the pFCC crystal and the BCT crystal in the NPT ensemble (inset). Both of these features indicate a first-order transition. **(b)** The orientational order parameter rises steadily with density throughout the plastic crystal phase, and its value jumps at the transition to the BCT crystal; it also exhibits hysteresis in the NPT ensemble (inset). **(c)** For a lower-density pFCC crystal (*e.g.*, $\phi = 0.550$), the energy wells of the PMFT are connected in a dodecahedron-shaped cage. At higher densities ($\phi = 0.675$), the lowest-energy configurations are centered at the ICO's edges. In the BCT crystal, the strongest preference for a neighboring particle position is centered at the ICO's facets (see dashed-line box). **(d)** In the BCT crystal, particles tend to preferably adopt parallel orientations (marked with red diagonal hatch lines) or misalign by $\approx 42°$ (marked with blue horizontal hatch lines). In the plastic crystal, there is only a slight preference towards the parallel orientations, and the high-angle misalignments occur with a lower frequency than a random sampling of orientations. **(e)** The rotational autocorrelation function monotonically decreases for the pFCC crystal and a BCT crystal at $\phi = 0.70$. At higher densities, the decay will initially occur very slowly.

two specific orientations, but the arrangement of these two orientations is not strictly periodic. Examples of this difference in orientational order can be seen in Fig. 4.2. We note that the BCT structures that form upon compression of the plastic crystal do not correspond to the densest packing phase for TC or ICO.

We see that the pFCC-to-BCT crystal transition is first-order from the equation of state. In NPT simulations (the zoomed insets of Figs. 4.3**(a)** & 4.4**(a)**), the hysteresis between the two states is clear: for a single pressure, the system will be in one of the two states depending on its initial state. For NVT simulations in the vicinity of the transition, a Mayer-Wood loop occurs with the transition from the pFCC to BCT crystal [113]. Fig. 4.5**(a)** shows that the height of this loop decreases with system size. A Mayer-Wood loop appears as a result of coexistence between the two phases, and the height of the loop decreases because a smaller proportion of the system exists at the interface with larger systems [114]. Figs. 4.5**(b & c)** show coexistence behavior based on local density for two different system sizes of TC. Phase coexistence occurs over a wider range of densities when $N = 16384$, and this further helps decrease the size of the Mayer-Wood loop as compared to smaller system sizes. Coexistence of the pFCC and BCT crystals is identified when there are two distinct peaks in the local density of a system.

A discontinuity in an order parameter's first derivative with respect to density is yet another way to show a first-order transition. Our orientational order parameter (OOP) displays such behavior, showing a clear jump in its value between the pFCC and BCT crystal phases. This response in the OOP occurs because of the spontaneous change in the distribution of orientations as the cubic symmetry breaks. Once the system shows tetragonal symmetry, the individual particles preferentially adopt two orientations.

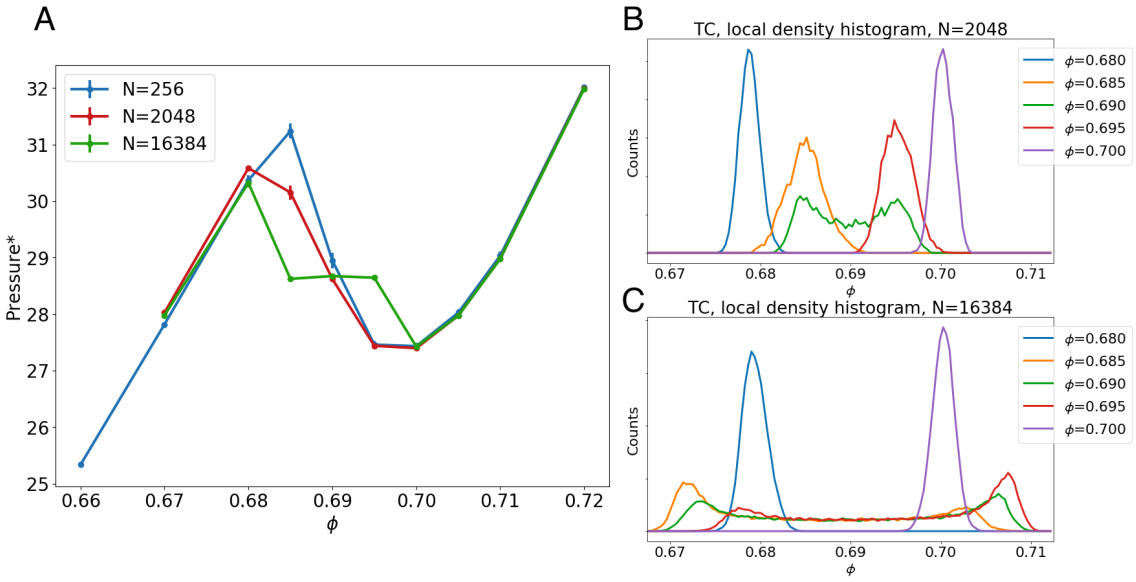

Figure 4.5: Evidence of a first-order phase transition for TC. **(a)** Equation of state from NVT simulations as a function of system size. The decrease in the size of the Mayer Wood loop with increasing system size is the result of two-phase coexistence and comparatively fewer particles being at the interface. **(b)** For system sizes $N = 2048$, coexistence is only observed at a density $\phi = 0.69$. **(c)** For system sizes $N = 16384$, the system will separate into the pFCC and BCT phases when the total density is $0.685 \leq \phi \leq 0.695$.

The PMFT likewise displays discontinuous behavior across the transition. The PMFT shows the propensity for a neighboring particle to arrange in any position relative to a fixed orientation of a reference particle. The dotted boxes in Figs. 4.3**(c)** & 4.4**(c)** highlight a change in the shape of the lowest free energy wells in the PMFT across the phase transition. For TC, the free energy well opposite each hexagonal facet is connected as one continuous isosurface for the pFCC crystal, but this free energy well separates into three distinct isosurfaces in the BCT crystal. In ICO's pFCC phase, the lowest energy sites occur opposite the particles' edges. In ICO's BCT phase, the lowest free energy sites occur opposite the particles' facets. Increasing the density within the plastic crystal phase decreases the free energy in these wells, but does not significantly change the shape of these wells.

The orientation-orientation coupling further describes the particles' local environment. Because of the rotational symmetry of the particles, random orientations do not lead to a normal distribution, but rather to a 'sharkfin'-shaped distribution described elsewhere [115]. The shape of this distribution arises because there become more paths to rotate a particle to a symmetrically equivalent orientation for higher misorientation angles. At lower densities (*e.g.*, $\phi \approx 0.50$), the neighbor misalignments for plastic crystalline systems resemble a random distribution. Figs. 4.3**(d)** & 4.4**(d)** depict histograms of the minimum angle that separates the orientations of neighboring particles. In the BCT phase, TC and ICO systems show similar behavior: one peak develops for small angles corresponding to neighboring particles aligning (marked in Figs. 4.3**(d)** & 4.4**(d)** red diagonal hatch lines) and a second peak develops around a larger angle corresponding to particles misaligning in a specific manner (marked with blue horizontal hatch lines). These two shapes however show distinct behavior in the plastic crystal phase. For TC, the two separate peaks begin

to develop with increasing density in the plastic crystal. This indicates that the local environment in the plastic crystal will take on features resembling the BCT phase before any long-range, system-wide symmetry breaking occurs. For ICO, increasing the density of the pFCC phases only increases the likelihood of aligned orientations; high levels of misalignment between neighbors are always less likely than a random distribution for ICO in a plastic crystal. It is only after the transition to a BCT crystal that it becomes likely for the minimum angle between two particles to exceed 40°. A potential explanation for this behavior can be gleaned from the PMFT: after the transition to a BCT phase, it becomes much more favorable for two neighboring ICOs to be aligned facet-to-facet (see dotted box in Fig. 4.4**(c)**, $\phi = 0.725$). When contacting at their facets in this manner, neighboring particles will adopt either a similar orientation or the complementary one for the BCT packing.

Information from the equilibrium behavior of particle local environments helps to explain dynamical properties. The development of two-step relaxation in the rotational autocorrelation functions (Figs. 4.3**(e)** & 4.4**(e)**) does not necessarily coincide with the phase transition from pFCC-to-BCT. Such behavior does occur for TC, but lower density BCT crystals of ICO do not exhibit an initial plateau. Instead, the plateau appears to correlate with the orientation-orientation coupling. Once it becomes very unlikely to find the orientations of neighboring particles to be separated by an intermediate angle (*i.e.*, the probability in the middle of a neighbor misalignment curve is near zero), particles in these systems begin to display two-step relaxation in their rotational autocorrelation functions.

4.3.2 Gradual Order Development

We study two shapes that show a gradual development of orientational order and do not exhibit a thermodynamically distinct plastic crystal phase: the rhombic

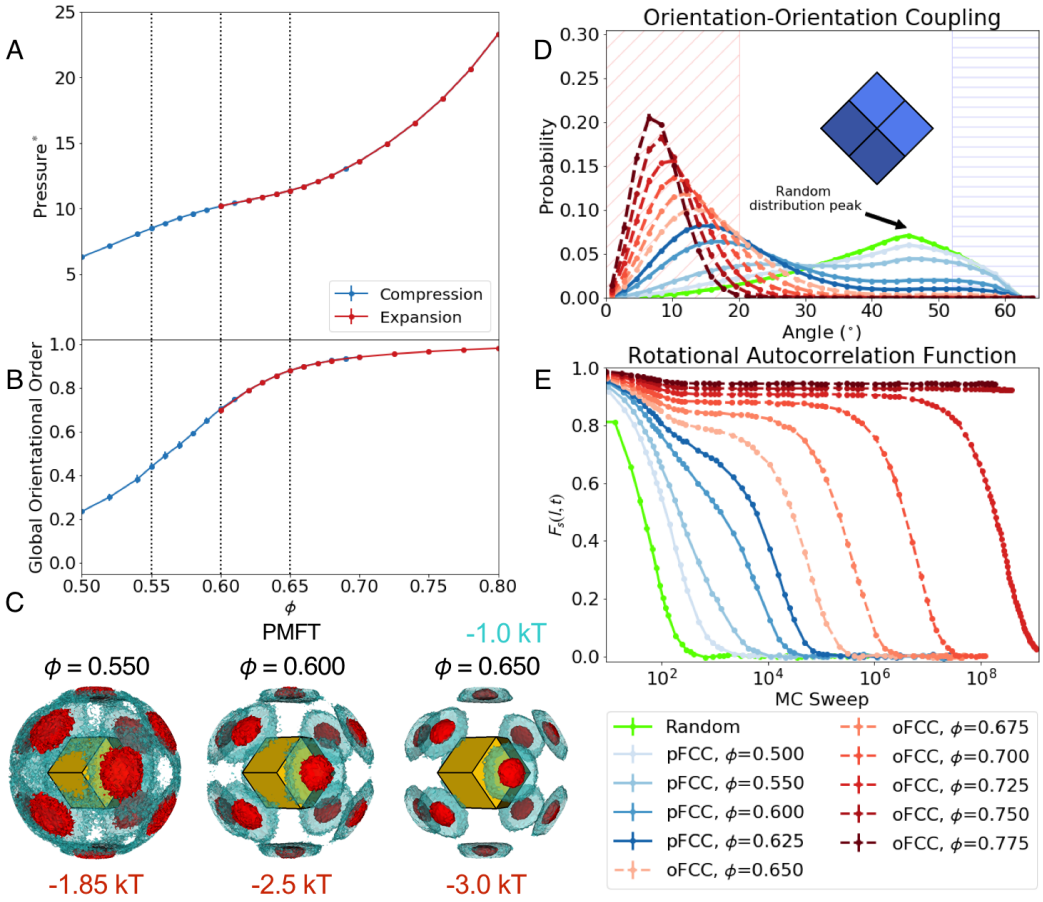

Figure 4.6: Phase behavior of the rhombic dodecahedron (RD). **(a)** The equation of state shows no distinct features of a phase transition or dependence on the initial state. **(b)** The global orientational order parameter begins with a value above zero and shows a rapid rise between densities of $\phi = 0.50$ and $\phi = 0.65$ before it begins to converge to 1.0 more slowly. **(c)** At all densities, the energy wells of the PMFT are located at the 12 facets of the RD. The relative spread of the $-1.0k_BT$ isosurface decreases with increasing density while the depth of the free energy wells increases. **(d)** Increasing the density of the system results in increasing the likelihood of particles to have progressively similar orientations (region with red diagonal hatch lines), as the likelihood of a large misalignments shows a monotonic decrease (region with blue horizontal hatch lines). **(e)** The two-step relaxation in the rotational autocorrelation function begins to appear at $\phi = 0.65$, and we use this behavior to approximate the transition from pFCC to oFCC behavior.

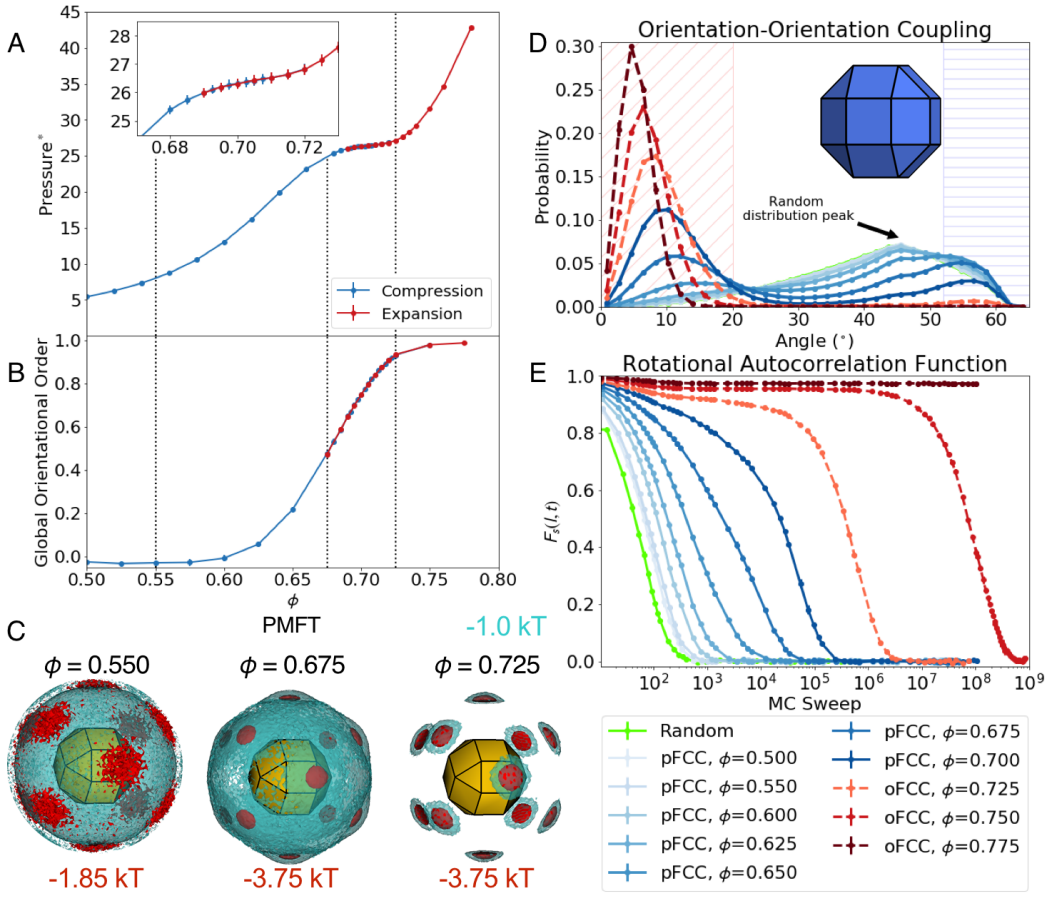

Figure 4.7: Phase behavior of the rhombicuboctahedron (RC). **(a)** The equation of state lacks a first-order signature, although it does nearly flatten around a density of $\phi = 0.70$. **(b)** The global orientational order parameter does not increase for densities $\phi < 0.60$, but then begins to display a steady rise. **(c)** The location of the lowest-energy wells remains the same across all densities. However, the relative strength of the lowest-energy sites compared to the intermediate locations between these sites changes. **(d)** With increasing density, neighboring particles become more likely to adopt equivalent orientations (region with red diagonal hatch lines). For densities $\phi \leq 0.70$, large misalignments between neighboring particles (*e.g.*, separation angles of $\approx 55°$; marked with blue horizontal hatch lines) occur more frequently than in a random distribution of orientations. **(e)** The rotational autocorrelation function displays two-step behavior after strong orientational order develops.

dodecahedron (RD, Fig. 4.6) and the rhombicuboctahedron (RC, Fig. 4.7). Both these shapes pack in an FCC crystal; although, the larger number of facets of RC (18 square and 8 triangular facets) affects the development of orientational order as compared to RD (12 identical, rhombic facets). The equations of state for both shapes lack the signature of a first-order transition: they show no hysteresis, and no coexistence between orientationally ordered and disordered phases is observed.

The equation of state for RC does show a distinctive near-flattening in the density range $0.68 < \phi < 0.73$. We have run simulations at various system sizes to show that this feature does not correspond with a continuous phase transition. In a second-order phase transition, we would expect to see discontinuities in a derivative of free energy, F [116]. In an NVT ensemble wherein $P = -(\frac{\partial F}{\partial V})$, the bulk modulus, K, is a second-order derivative:

$$K = -V\frac{\partial P}{\partial V} = V\frac{\partial^2 F}{\partial V^2} \tag{4.8}$$

Fig. 4.8 shows the bulk modulus plotted against density for $N = 256,\ 864,\ \&\ 16384$. We do not find any change to the bulk modulus as a function of system size. If there were a critical phenomena associated with a higher order phase transition, one would expect to see divergence as the system approached the thermodynamic limit. This region with the decreased bulk modulus corresponds with when strong orientational order develops without a phase transition.

While neither of these shapes show a distinct, thermodynamic plastic crystal phase, we can identify properties of these systems that differentiate 'plastic crystal-like behavior' at lower densities as compared to the 'crystal-like behavior' at higher densities when the system is in an orientationally ordered FCC (oFCC) state. Based on our results, we argue that RD and RC systems show plastic crystalline behavior up

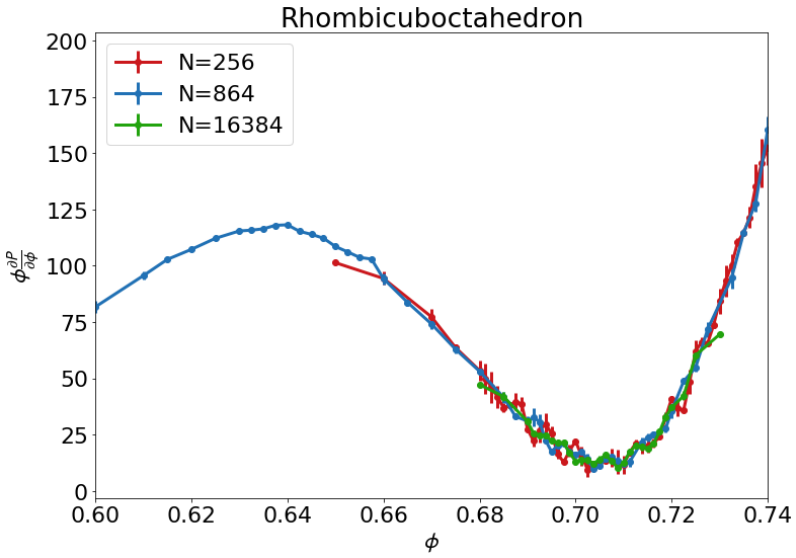

Figure 4.8: Bulk modulus of RC for system sizes $N = 256,\ 864,\ \&\ 16384$. The value of the bulk modulus does not depend on system size, which indicates that there is not a continuous phase transition.

to densities of approximately $\phi \leq 0.63$ and $\phi \leq 0.70$, respectively. These values are approximate because we cannot define a clear transition point; however, we observe notable differences in behavior above and below these densities.

The behavior of global orientational order (Figs. 4.6**(b)** & 4.7**(b)**) and the rotational autocorrelation functions (Figs. 4.6**(e)** & 4.7**(e)**) distinguish plastic crystal from crystal behavior. At densities low enough to observe plastic crystal behavior, our order parameter increases rapidly with respect to density. After the change from plastic crystal to crystal behavior, the slope decreases as the order parameter trends towards 1.0, *i.e.*, the densest packing value. As is the case with the first-order transition, the rotational autocorrelation function shows two general types of behavior as a function of density. At lower densities, a rapid drop-off occurs in the rotational autocorrelation function. At high densities, the two-step behavior occurs due to particles generally displaying only a slight deviation from the preferred orientation of the densest packing.

Descriptors of the local particle environment—the PMFT and orientation-orientation coupling—also show characteristics of plastic crystal behavior. When the system acts as a plastic crystal, the PMFT is only weakly anisotropic (Figs. 4.6**(c)** & 4.7**(c)**). At the lowest densities, the free-energy isosurface corresponding to $-1k_BT$ is continuously connected across all the bonding sites, indicating that particle alignments other than facet-to-facet are not strongly penalized and changes in particle orientation are relatively easy. With the gradual development of orientational order, we cannot necessarily use the PMFT to identify the changeover density towards an oFCC state. Instead, the 12 PMFT free energy wells congruent with a local FCC environment become increasingly lower in free energy compared with other arrangements. When this free energy disparity is large enough, plastic crystal characteristics vanish. The orientation-orientation coupling does, however, offer a guideline. The strongest feature of Figs. 4.6**(d)** & 4.7**(d)** is how it becomes increasingly likely for particles to align as the density increases, and connected with this development is the probability of non-aligning orientation pairs decreasing. To distinguish plastic crystal behavior from crystal behavior in these systems, one can use the density at which the probability of finding intermediate angles between particles goes to zero.

While there are similarities in the transition behavior for these two shapes, the additional facets in RC lead to the plastic crystal behavior occurring over a wider range of densities as compared to RD. Figs. 4.9 and 4.10 compare the probability of particles adopting specific orientations as a function of density. The effect of RD having only the 12 bonding facets *vs.* RC having an additional 14 non-bonding facets can be seen in these comparisons. For both RD and RC, the probability of particles adopting particle orientations corresponding to the densest packing structure shows a monotonic increase with density. For RC, however, the non-bonding facets lead

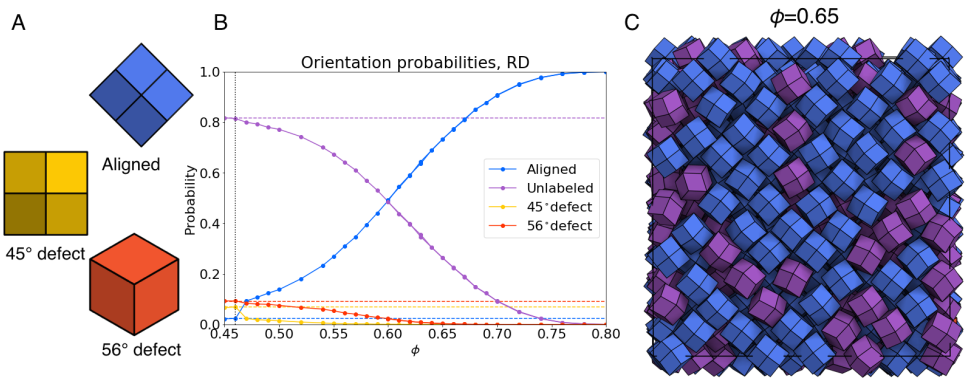

Figure 4.9: **(a)** Examples of the three types of orientations that we distinguish for RD. We classify whether a particle fits into one of these categories if its orientation is within a 15° cutoff. 'Aligned' refers to particles with the orientation that occurs in the densest packing. '45° defect' refers to particles rotated by 45° about one of the three principle axes of the particle relative to the 'aligned' orientation. '56° defect' refers to orientations in which a 3-fold vertex has replaced a 4-fold vertex relative to the 'aligned' orientation. 'Unlabeled' refers to all other particles whose orientations do not fit within the 15° cutoff of these orientations. **(b)** The probability of finding these different orientations as a function of density. The dotted lines signify the probability of finding such an orientation in a random distribution. For RD, only the 'aligned' orientations appear more frequently than would be expected in a random distribution. At $\phi = 0.46$, the increase in probability for 'aligned' particle orientations corresponds to the transition from a fluid to the pFCC crystal. **(c)** An example snapshot of a system at $\phi = 0.65$ with the particles colored by orientation.

to the existence of additional orientations (the '63° defect' orientations in Fig. 4.10) that are incommensurate with the oFCC arrangement, but that occur more often in the pFCC than would be expected from a random set of orientations. For RD, we are unable to find such an orientation that preferentially exists in the pFCC but not oFCC through simple geometric reasoning.

Understanding the additional preferential orientations arising when RC displays plastic crystal behavior explains some further discrepancies between RD and RC in Figs. 4.6 and 4.7. RC equation of state shows a distinctive near-flattening between the densities $0.675 < \phi < 0.725$ (the inset region of Fig. 4.7**(a)**). This density range corresponds to when additional preferred orientations vanish from the equilibrium system. In the global orientational order, the additional orientations suppress the value of the calculated order parameter. In Fig. 4.7**(b)**, the value of the global order

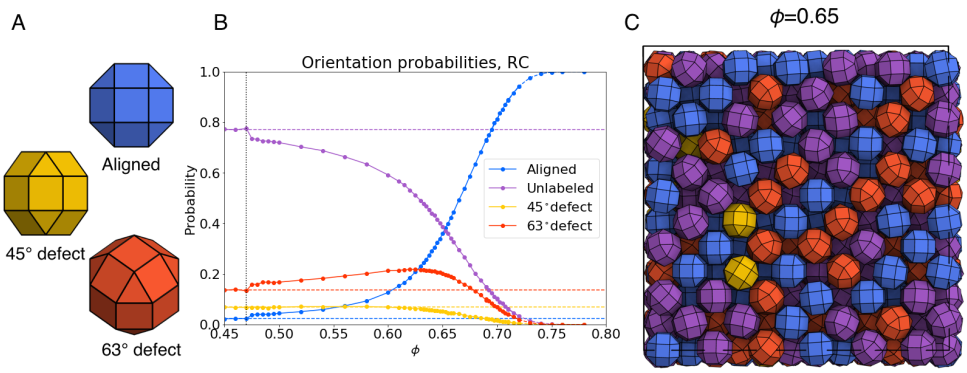

Figure 4.10: **(a)** Examples of the three types of orientations that we distinguish for RC. We classify whether a particle fits into one of these categories if its orientation is within a 15° cutoff. 'Aligned' refers to particles with the orientation that occurs in the densest packing. '45° defect' refers to particles rotated by 45° about one of the three principle axes of the particle relative to the 'aligned' orientation. '63° defect' orientations can be attained *via* two separate 45° rotations about separate axes. 'Unlabeled' refers to all other particles. **(b)** The probability of finding these different orientations as a function of density. The dotted lines signify the probability of finding such an orientation in a random distribution. At $\phi = 0.475$, there is an increase in probability for 'aligned' and '63° defect' corresponding to the transition from a fluid to the pFCC crystal. Below a density $\phi = 0.67$, '63° defect' orientations occur more frequently in a system of RC than would be the case in a random distribution of orientations. **(c)** An example snapshot of a system at $\phi = 0.65$ with the particles colored by orientation.

does not begin to rise above a value of 0 until a density of $\phi \approx 0.60$. The trend also affects local environment in the orientation-orientation coupling: when RC still exhibits plastic crystal behavior, the probability of finding high-angle misalignments between neighbors is greater than that of a random distribution of orientations (marked with a blue horizontal hatch lines in Fig. 4.7**(d)**).

4.3.3 Orientational Glassy Behavior

When compressing a plastic crystal of pseudorhombicuboctahedra (PRC), the system is unable to adopt a phase with long-range orientational order. We find that PRC densely pack in a BCT structure similar to that of TC or ICO. However, PRC do not spontaneously undergo tetragonal symmetry breaking with compression wherein two orientations are preferred over all others. The equation of state (shown in Fig. 4.11**(d)**) reflects this behavior: when initialized in the BCT phase, the PRC

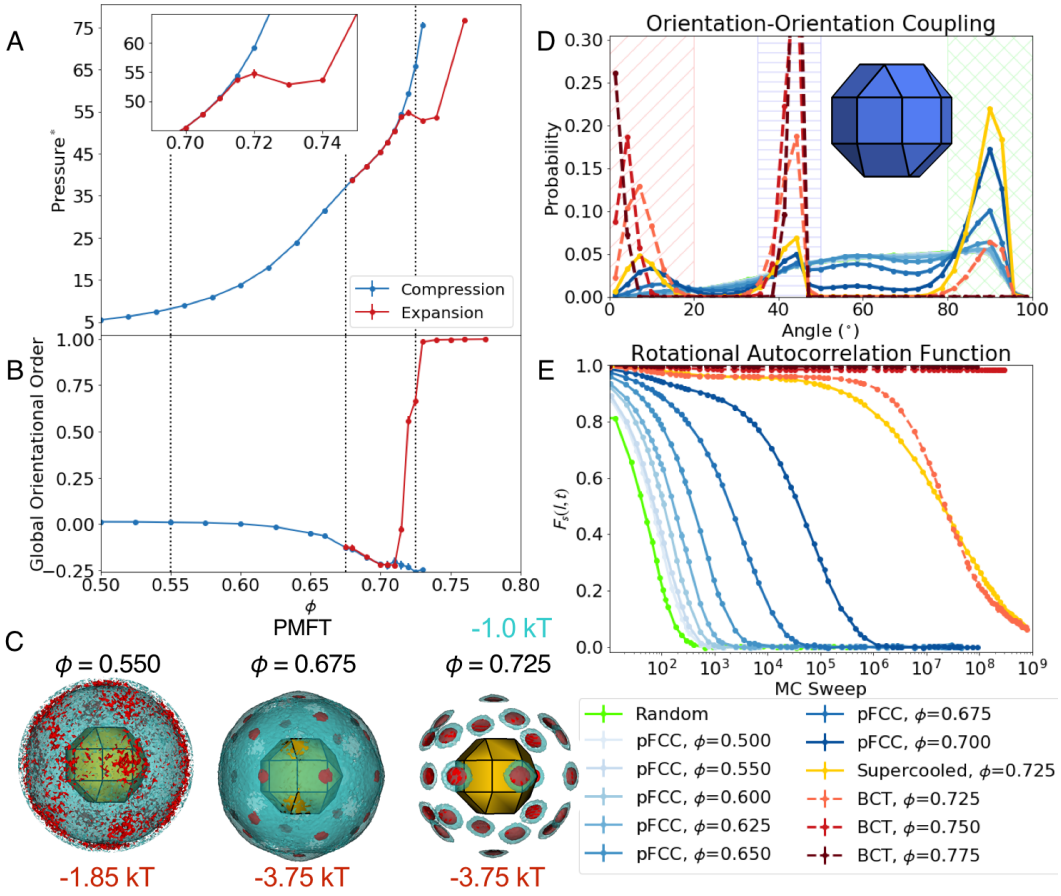

Figure 4.11: Phase behavior of the pseudorhombicuboctahedron (PRC). **(a)** PRC melt to a pFCC crystal when initialized in the BCT structure and relaxed to lower densities. However, no phase transition occurs when initialized in a plastic crystal and compressed; FCC translational order persists and particles adopt six orientations in a random manner. In the BCT structure, particles preferentially adopt two orientations. **(b)** As the density of the plastic crystal increases, the global orientational order parameter goes below zero because particles increasingly adopt one of six separate orientations. In the BCT crystal, the global order is near one because the particles predominantly have just one of two orientations. **(c)** PMFT for pFCC at $\phi = 0.550$ and $\phi = 0.675$ and BCT at $\phi = 0.725$. At the lowest densities, the PMFT is highly isotropic. At a density $\phi = 0.675$, 24 distinct free-energy wells develop, but the $-1k_BT$ isosurface is still relatively isotropic. For the BCT phase at $\phi = 0.725$, the connectivity of this $-1k_BT$ isosurface disappears. **(d)** Upon compression, three distinct peaks develop in the orientation-orientation coupling. The largest peak corresponds to an $\approx 90°$ misalignment in these cases (marked with checkered green hatch lines). When the system is initialized in a BCT structure with two types of orientations, the highest peaks correspond to aligning orientations (marked with red diagonal hatch lines) or $\approx 45°$ misalignments (marked with blue horizontal hatch lines). **(e)** The rotational autocorrelation function shows a supercooled FCC phase and BCT crystal will have slightly different behavior at a density $\phi = 0.725$, though they both show two-step relaxation.

crystal will melt into the pFCC crystal at a sufficiently low density. However, when a pFCC crystal is compressed to higher densities, no phase transition is observed. To apply the typical language of glassy systems, the system enters a "supercooled plastic crystal," or alternatively "supercompressed," whenever the equation of state for FCC-initialized systems does not match with BCT-initialized systems. As can be seen in Fig. 4.11**(e)**, the supercooled state with FCC translational order shows clear two-step behavior in the rotational autocorrelation, and particle orientations relax on a timescale of 500 million MC sweeps. Fig. 4.11**(e)** does not include a bona fide glass with FCC order (the rotational autocorrelation would not decay at any time scale), but we expect such behavior to occur with maximally compressed systems of PRC on an FCC lattice.

The global order of PRC shows a distinctive behavior that is dictated by the particle shape and the orientational glassy transition. In Fig. 4.11**(b)**, the primary result to note is that global order does not develop upon compression of the system. Instead, the order parameter becomes negative at densities $\phi > 0.62$. We rationalize this behavior by understanding the orientations that appear in the BCT packing. The unit cell of the BCT packing contains two particles in an alternating arrangement that are separated by a 45° rotation. The BCT packing can break cubic symmetry along three separate directions, resulting in six distinct orientations. In the supercooled FCC state or the orientational glass, particles will adopt these six orientations (as can be seen in Fig. 4.2), and the higher-density plastic crystals begin to preferentially contain particles with these six orientations. For each of these six distinct orientations, there is the one complementary orientation separated by a 45° rotation and the four other orientations that are separated by a 90° rotation. When these six orientations preferentially occur, the order parameter (Eqn. 4.4) takes on

a negative value because of the abundance of these large separation angles relative to the reference state of a random distribution of orientations.

The orientation-orientation coupling of Fig. 4.11**(d)** further clarifies the above description on the behavior of the six orientations. When the system adopts the BCT crystal structure, most neighboring particles have orientations separated by less than 20° (*i.e.*, approximately aligned in parallel; marked with red diagonal hatch lines) or ≈ 45° (*i.e.*, alternating orientations compatible with the BCT structure; marked with blue horizontal hatch lines). In the higher-density structures that retain cubic translational symmetry, neighboring particles are approximately 4 times more likely to be misaligned by ≈ 90° (marked with green, checkered hatch lines) than they are to align or adopt the specific, alternating orientation.

The difference in behavior between PRC and RC is clearly illustrated by the PMFTs in Fig. 4.11**(c)**. Both shapes have the same numbers and shapes of facets; however, PRC has a lower group symmetry. One can construct the location of the lowest energy wells in PRC by duplicating the PMFT of RC and applying a 45° rotation. The PMFT helps us to understand the apparent approach towards an orientational glass: the lower symmetry of PRC leads to many distinct bonding configurations that all have comparable energies. By having so many configurations with degenerate energies, the system is unable to undergo a long-range symmetry breaking wherein particles preferentially adopt one of two orientations required for the transition to a BCT crystal.

4.4 Discussion

Through our analysis, we identify a few characteristic behaviors in systems of hard polyhedra that form plastic crystalline phases with varying levels of orientational

order. Some of these properties appear to be universal, while others depend on the phase behavior with respect to increasing density.

When measuring the global orientational order, a comparison against the orientation(s) that appear in the denser, orientationally ordered phase is paramount. When a system gradually develops orientational order, measures of global orientational order also increase gradually as the particles progressively adopt the orientation corresponding to the densest packing. In these cases, the transition away from plastic crystal behavior can roughly be defined by the flattening of the global orientational order measure with respect to density (see Figs. 4.6**(b)** & 4.7**(b)**) as it subsequently approaches 1.0, *i.e.*, the fully ordered state. When the plastic crystal is a distinct phase, global measures of orientational order will exhibit a jump at the transition as global symmetry is broken.

Descriptors of the local environment appear to be effective at distinguishing whether or not orientational order develops. In our study, we characterize local environments *via* the PMFT and by computing orientation-orientation correlations between neighboring particles based on angles of separation. These two descriptors capture information about orientational order development, but express it in slightly different ways. In terms of the PMFT (which expresses the effective free energy of different pair configurations), the loss of plastic behavior in all cases we studied coincides with system densities at which intermediate configurations between different bonding wells become associated with high energies. The orientation-orientation coupling leads to a similar conclusion: the loss of plastic crystal behavior and development of orientational order corresponds with the probability of finding angles not associated with the packing structure going to zero.

These trends also fit with the results on the rotational dynamics of the system.

Across all systems studied, we find that the rotational autocorrelation function develops two-step behavior at high densities. We explain the plateauing behavior as occurring at densities where particles experience cage-like rotational motion: they are able to make small rotational moves about an average orientation. A set of rotational moves that take particles outside of this cage can occur, but this happens very infrequently (as evidenced by the fact that local environment measures show a vanishing of intermediate orientations). This transition from a relatively rapid decline in the rotational autocorrelation without the short time scale plateauing can be used to help identify the transition away from plastic crystal behavior.

This work can be seen as an extension of rules identified for the orientational order in two-dimensional systems of hard polygons [107]. Polygons that possess the same symmetry as the two-dimensional lattice in which they crystallize are found not to display a distinct plastic crystal phase. On the other hand, shapes that share a subset of symmetry elements with their translation lattice will exhibit a plastic crystal – with preferred polygon orientations. These exact rules do not hold in three dimensions because particle symmetry does not dictate bonding symmetry in the same way (*e.g.*, RC and TC have identical symmetry, but due to different faceting, their PMFTs show 12 and 14 bonding sites, respectively). Instead, one must compare the alignment of a shape's largest facets (and therefore its bonding preferences) to its crystal environment to arrive at similar rules.

When the bonding symmetry does not align with the local particle environment in the crystal (*i.e.*, the vertices of a crystal's coordination polyhedron) particles must inherently have equivalent facets pointing in different directions relative to the positions of their neighbors (*e.g.*, TC's pFCC crystal has 14 unique bonding wells, as evidenced by the PMFT, but particles have a coordination number of 12). There are

a few distinct, preferred orientations that a particle will adopt in the plastic crystal (for TC, there are three orientations that occur with the highest probabilities). At the orientational ordering transition, symmetry is broken whereby a smaller number of these preferred orientations occur as the translational order shifts to a phase that packs more effectively.

When bonding symmetry does align with the crystal, order develops gradually without a distinct phase transition. In these cases, it is possible for each individual particle to adopt an orientation wherein a facet points in the direction of a neighbor. For lower-density crystals, it is unlikely for long-range orientational order to exist because there are still many other orientations that are sterically accessible. As the density increases, more and more particles adopt the orientation that maximizes having their largest facets aligned with their neighbors, and long-range order develops as a result.

The final case that we studied possesses a subtle tweak to the bonding symmetry because of the gyrated nature of the PRC. Whereas the RC contains a single symmetrically distinct orientation that maximizes facet-to-facet contacts between neighbors in an FCC environment, systems of PRC become orientationally frustrated upon an increase in density, and the resulting configuration contains six distinct orientations compared with the expected two in an ideal structure. Long-range order fails to develop because there are too many distinct particle arrangements that are all energetically very similar.

These results can be used towards more general designs of plastic crystal properties in anisotropic colloidal systems. If the facets of a particle are not congruent with the local environment in a plastic crystal, then a first-order transition (and the hysteresis that comes with it) can be expected upon changing the density (or pressure). If

one desires to achieve a more continuous control over the orientational order, then a building block with facets that do align with a crystalline environment will be necessary. The difference in behavior between RD and RC further offers design knobs for controlling a system's behavior. By decreasing the size of the bonding facets (and concurrently adding additional facets), the plastic crystal behavior can be accentuated and allowed to occur over a wider range of pressures or densities.

4.5 Conclusion

In this work, we have investigated a number of model hard particle systems that exhibit the characteristic behavior of plastic crystals: translational order, but orientational disorder. The behavior in these systems can be studied through equations of state, global order measures, local environment measures, and dynamical properties of particles' rotations. We find that orientational order can develop with increasing density in three ways. A plastic crystal can undergo a first-order phase transition when long-range orientational order develops with a change to the translational order. Plastic crystals can undergo other transitions that are not distinct, thermodynamic transitions. They can gradually develop long-range orientational order as the system transitions to packing behavior without a change to its translational order, or they can undergo a rotational vitrification process, wherein translational order does not change and particles become stuck in a few distinct orientations that occur at random. The behavior of these systems can most readily be understood through the lens of the theory of directional entropic forces. When plastic behavior occurs in a system of hard particles, DEFs will show some preferences, but the entropic forces are not too strongly anisotropic. If DEFs align with a crystal's coordination geometry, order can be expected to gradually develop. If the DEFs show there to

be many equivalent bonding states, it can be expected for the system to randomly adopt these different bonding states. Otherwise, a first-order transition will occur as a structure re-arranges to pack more effectively.

CHAPTER V

Complex Crystal Behavior from Truncated Dodecahedra

The contents of this chapter are adapted from an in-progress manuscript being prepared by A.S. Karas, J. Dshemuchadse, N. Minsk, G. van Anders, and S.C. Glotzer.

5.1 Introduction

Many crystal phases that form under entropic assemblies are highly symmetric with all particles having equivalent local environments. In particular, the high coordination face-centered cubic (FCC) and body-centered cubic (BCC) crystal structures are frequently reported in both simulations [26, 54] and physical experiments [63, 66]. Based on ideas of directional entropic forces, achieving a specific valence for a system's entropic bonds through facets is possible to an extent [68, 69]. However, many lower-symmetry crystals cannot be achieved through entropic assembly even when targeting a crystal through its Voronoi particle. At moderate densities, Schultz *et al.* showed that systems typically favor higher symmetry crystals wherein particles favor degeneracy [96]. In this chapter, I will detail an instance wherein hard particles acting only through entropy can form phases that do not show typical degeneracy and instead particles have separate local environments based on the crystal lattice site.

A regular dodecahedron and its truncations are the focus of this study. The dodecahedron is a shape where the naive entropic bonding valence (*i.e.* assume the particle forms an entropic bond at the center of each facet) has icosahedral symmetry and is therefore not commensurate with forming periodic structures. It has been shown [26] that low levels of truncation can lead to β-Mn and γ-brass crystal structures, which possess large unit cells and are typically associated with intermetallic systems [117, 118, 119, 120, 121]. One feature that sets β-Mn and γ-brass apart from typical entropic assemblies is that they possess multiple Wyckoff sites, which are symmetrically inequivalent positions within a crystal.

In this work, I investigate the behavior of truncated dodecahedra capable of self-assembling either FCC, β-Mn, or γ-brass. I show that truncated dodecahedra in β-Mn and γ-brass contain different coordination environments for the different Wyckoff sites which leads to different local free volume. This transfer of free volume for the different Wyckoff sites shows similarities to arguments used to rationalize such behavior in other systems, such as charge transfer in atomic systems [122, 123] and mass transfer in soft matter systems of diblock copolymers [124].

One way to understand the differences between FCC, β-Mn, and γ-brass is through the coordination polyhedra of the Wyckoff sites, which can be seen in Fig. 5.1. A coordination polyhedron represents the geometric pattern of a particle's nearest neighbors. Coordination polyhedra can tell us about the directionality of the bonds that form in a system. A coordination number is the number of neighboring particles in a first-nearest neighbors shell, and it corresponds to the number of vertices in a coordination polyhedron. The coordination polyhedra for a crystal structure are related to Voronoi polyhedra: they are duals of one another. A smaller facet in a Voronoi polyhedron corresponds to a further bond distance in the coordination geometry. FCC is

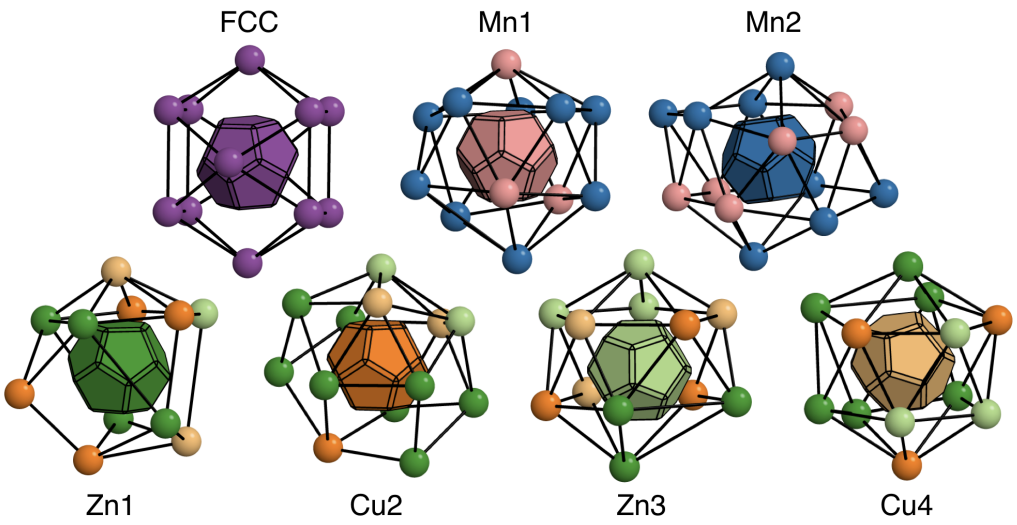

Figure 5.1: The coordination polyhedra for the unique Wyckoff sites in FCC, β-Mn, and γ-brass. The 12 nearest neighbors for FCC are arranged at the vertices of a cuboctahedron. In β-Mn, the Mn1 site has 12 neighbors arranged in a distorted icosahedron, while the Mn2 site has a coordination number of 14. In γ-brass, the Zn1 and Cu2 sites have 11 and 13 nearest neighbors, respectively, and Zn3 and Cu4 both have a distorted icosahedron as their coordination polyhedron.

the simplest of structures that form in systems of truncated dodecahedra, with four particles per unit cell and only a single Wyckoff site. FCC's coordination polyhedron is the cuboctahedron, a shape with 12 identical vertices that has octahedral point group symmetry, which does not match that of the dodecahedron.

Both β-Mn and γ-brass are structures that share similarities with Frank-Kasper phases in that they contain asymmetric icosahedral coordination [125]. β-Mn is a cubic structure with a 20-particle unit cell with two symmetrically inequivalent Wyckoff sites. It is composed of 8 Mn1 particles and 12 Mn2 particles. These two Wyckoff sites have different coordination polyhedra: a distorted icosahedron for the Mn1 position and a 14-vertex coordination polyhedron at Mn2 [117, 121]. The Mn1 positions form a chiral tetrahelix structure like that shown in Fig. 3.1, and the Mn2 positions form a network of corner-sharing triangles akin to a three-dimensional version of a Kagome lattice [119]. In addition to pure elemental Mn, β-Mn structures

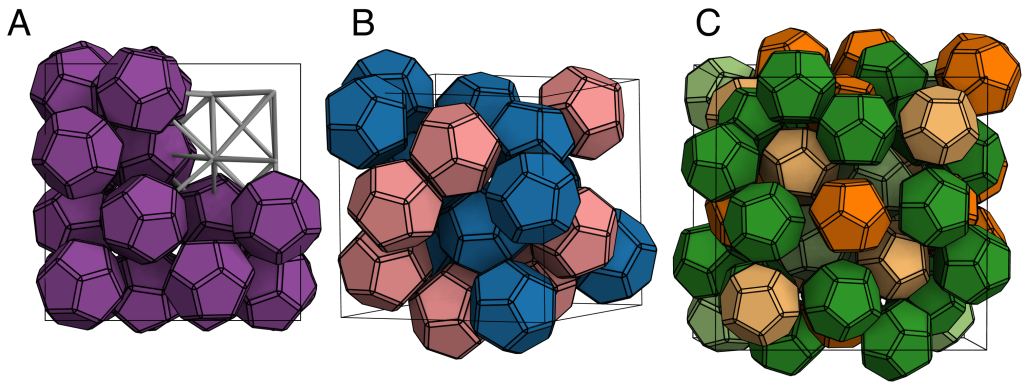

Figure 5.2: Examples of the structures in this study. **(A)** Dodecahedra in an FCC crystal. **(B)** The β-Mn unit cell. The 8 Mn1 sites are filled with light blue particles and the 12 Mn2 sites are filled with dark blue particles. **(C)** The 52-particle unit cell of γ-brass. The Zn1 and Zn3 sites are colored dark and light green, respectively, and the Cu2 and Cu4 sites are colored dark and light orange.

have been found in intermetallic systems such as $Mn_{1-x}Al_x$ [119] and $Co_{8+x}Zn_{12-x}$ [121].

γ-brass has a 52-particle unit cell, and the canonical intermetallic compound is Cu_5Zn_8. The unit cell can be constructed from a body-centered arrangement of two 26-particle clusters composed of four, nested polyhedral shells. Working from the innermost layer, the Zn3 Wyckoff site corresponds to four particles arranged in an inner tetrahedron, and these are flanked by four more particles that form an outer tetrahedron, the Cu4 site. The Cu2 site corresponds to six particles in an octahedral arrangement. These are surrounded by 12 more particles forming a cuboctahedron and corresponding to the Zn1 site. Both Zn3 and Cu4 sites have a distorted icosahedron for their coordination polyhedra, while the Cu2 and Zn1 sites have 13-and 11-particle coordination environments, respectively [120]. Examples of truncated dodecahedra colored by their Wyckoff site for FCC, β-Mn, and γ-brass are shown in Fig. 5.2.

5.2 Methods

I generate raw data in two separate ways. One is via self-assembly simulations wherein a large system is slowly compressed in an NVT simulation with flexible box shape from a disordered fluid and equilibrated at the desired density. In this protocol, the structure is allowed to form with no bias. The other way is by initializing particles in a specific crystal structure and slowly compressing the system while only allowing the particles to rotate. Once at the desired density, particles are able to make translation moves. By initializing the system in the structure, I am able to label particles by their Wyckoff site in order to compare particles based on their Wyckoff site. For these simulations, I use $N = 2048$ for FCC (4-particle unit cell), $N = 10240$ for β-Mn (20-particle unit cell), and $N = 11232$ for γ-brass (52-particle unit cell).

All comparisons of the particle behavior for the different Wyckoff sites were performed for the same shape at a density $\phi = 0.575$. I compute the rotational autocorrelation function and the minimum angle that separates neighboring particles in the same way as described in section 4.2. Calculation of the PMFT, the icosahedron coordination root mean squared distance (RMSD, which describes the minimum distance to move a particle's coordination environment onto the vertices of an icosahedron), Voronoi cells, radial distribution function, and the number of neighbors were performed with the *freud* software toolbox [111].

5.3 Results

5.3.1 Self-Assembly Propensity

I studied the self-assembly propensity for dodecahedra with two kinds of truncation: at the vertices and at the edges. Figures 5.3 & 5.4 summarize the probability

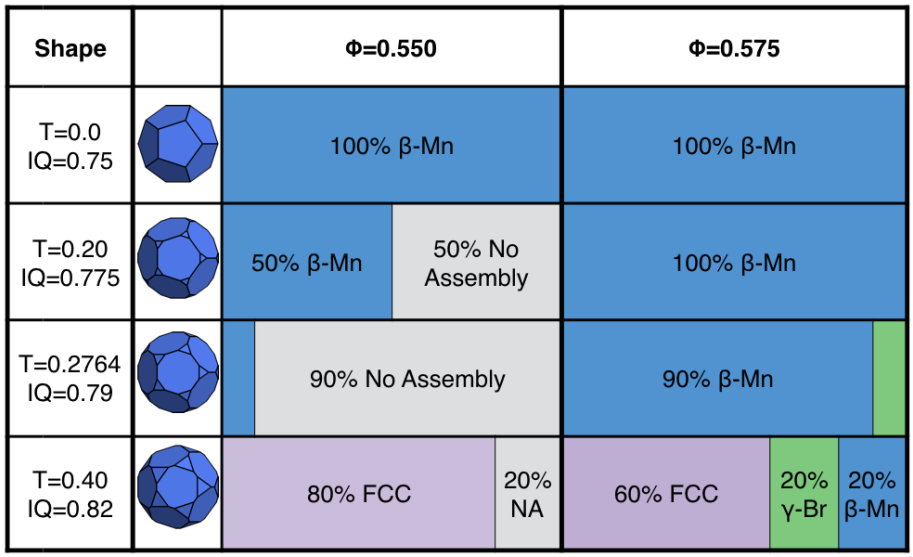

Figure 5.3: Statistics from self-assembly simulations at ϕ=0.55 & ϕ=0.575 for various levels of vertex truncation. The truncation parameter, T, ranges between 0 for a regular dodecahedron and 0.5 for an icosidodecahedron for vertex truncations. IQ is the isoperimetric quotient, which describes how close a shape is to a sphere. β-Mn forms at lower truncation (T) levels, while FCC and γ-brass can form at higher levels of truncation.

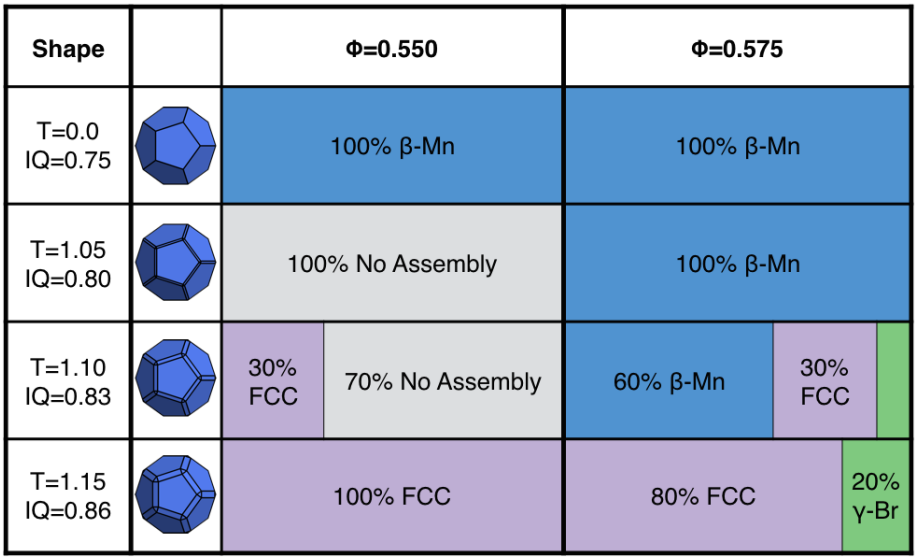

Figure 5.4: Statistics from self-assembly simulations at ϕ=0.55 & ϕ=0.575 for various levels of edge truncation. The truncation parameter, T, has $T > 1.0$ for edge truncations, and $T = 1.5$ corresponds to a rhombicosidodecahedron. IQ is the isoperimetric quotient, which describes how close a shape is to a sphere. β-Mn forms at lower truncation (T) levels, while FCC and γ-brass can form at higher levels of truncation.

of the different phases self-assembling at various density and truncation (T) state points. Vertex truncations correspond to $T \leq 0.5$ and edge truncations correspond to $1.0 < T \leq 1.5$. This data is based upon 10 independent replicates for system sizes $N = 10240$ or $N = 11232$.

The trends that occur for the two types of truncation are similar when comparing shapes by isoperimetric quotient (IQ). With no truncation, β-Mn was found to assemble in all 20 simulations at densities $\phi = 0.55$ & 0.575. At the density $\phi = 0.55$, truncation will first decrease the probability of β-Mn assembling, and further truncation leads to the assembly of an FCC crystal. At the density $\phi = 0.575$, truncation decreases the probability of β-Mn forming, and instead other crystals are capable of assembling for the independent simulations. The general trend that I find is that shape truncation and lowering density (which one expects to reduce strength of DEFs) can lead to structures other than β-Mn forming.

5.3.2 Local Environments in Different Structures

The results of the prior section show that three separate crystal structures (β-Mn, γ-brass, and FCC) are able to form via self-assembly for these truncated dodecahedra. At some state points, the systems were even capable of assembling all three structures in separate replicates. This leads to the questions: what is different about how truncated dodecahedra behave in these three different structures, and what might account for one structure preferably forming over another? In this section, I apply a variety of analysis techniques in order to describe the local environments in these crystal structures, with an emphasis on what is different for different Wyckoff sites. As was discussed in this chapter's introduction, the Wyckoff sites of β-Mn and γ-brass in atomic systems contain separate coordination polyhedra and bonding distances. I intend to show how this behavior extends to hard particle systems. The data for

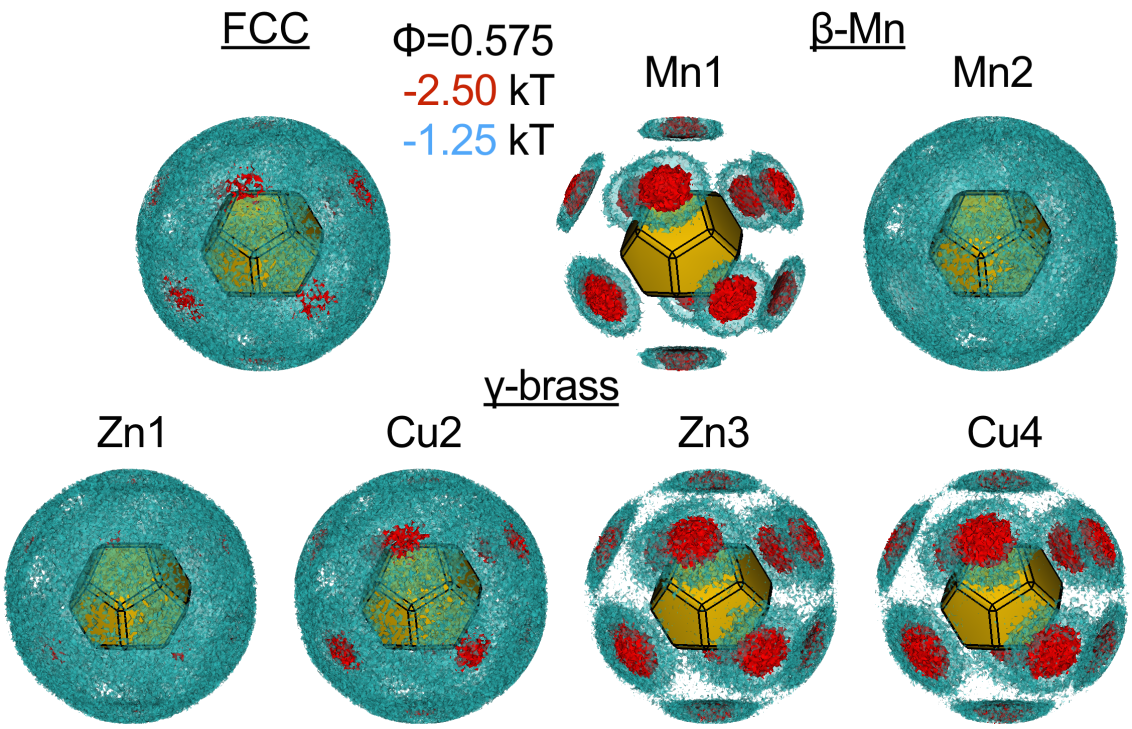

Figure 5.5: The potential of mean force and torque (PMFT) computed for all Wyckoff positions in FCC, β-Mn, and γ-brass with the shape truncation $T = 1.10$ and density $\phi = 0.575$. The different Wyckoff sites experience different directional entropic forces. When the blue isosurface corresponding to $-1.25k_BT$ is connected (FCC, Mn2, Cu2, and Zn1), the entropic forces are only weakly anisotropic. When the blue isosurface is not continuous and the red, $-2.50k_BT$ isosurface is large (Mn1, Zn3, Cu4), these Wyckoff sites experience strongly directional entropic forces with an icosahedral coordination that matches the particles' facets.

this analysis was generated by initializing particle positions in the crystal structures of interest. For simplicity, I confine my analysis to a single state point, $T = 1.10$ and $\phi = 0.575$, which is a truncation level and density at which all the crystal structures were observed to self-assemble.

As a first means of comparison, I compute the PMFT associated with each Wyckoff site. The PMFT provides information on the strength of entropic bonding. These results are shown in Fig. 5.5, and they clearly show that particles in different Wyckoff sites within a crystal structure can experience different DEFs. The Mn1, Zn3, and Cu4 sites experience stronger DEFs as evidenced by the disconnected isosurface

corresponding to $-1.25\,k_BT$ and the larger size of the $-2.50\,k_BT$ isosurfaces. In contrast, the Mn2, Zn1, Cu2, and the lone site for FCC all have weaker DEFs, indicating that there are no preferred alignments (include face-to-face) of these Wyckoff sites with their neighbors. Based on the differences in these PMFTs, I refer to the Mn1, Zn3, and Cu4 sites with stronger DEFs as "anisotropic sites," and I refer to the other sites as "isotropic" because of the diminished role of the facets.

The PMFT for the anisotropic sites shows an icosahedral coordination corresponding to the locations of the free energy wells. The icosahedral coordination makes intuitive sense: the icosahedron is the dual of the dodecahedron (which means that one can construct an icosahedron by placing vertices at the center of the dodecahedron's facets and facets at the location of the dodecahedron's vertices). These anisotropic Wyckoff sites correspond to the crystallographic sites with a distorted icosahedron for the coordination polyhedron.

The PMFT shows that the Mn1, Zn3, and Cu4 sites experience comparatively stronger directional entropic forces with an icosahedral coordination. In order to further quantify this icosahedral coordination and to show the effect that it has on a particle's environment, I compute a pair of quantities that summarize the difference in the local environments for the different Wyckoff sites: the Voronoi cell volume and the icosahedron coordination root mean squared distance (RMSD). The volume of a particle's Voronoi cell is a simple value to compute that will correlate with the amount of local free volume for that particle. The icosahedron coordination RMSD is a measure of the minimum distance required to align a particle's 12 nearest neighbors with an icosahedron. These two measures are plotted in two-dimensional kernel density estimation (KDE) plots in Figs. 5.6 & 5.7. KDE is a nonparametric scheme for estimating a probability density function [126].

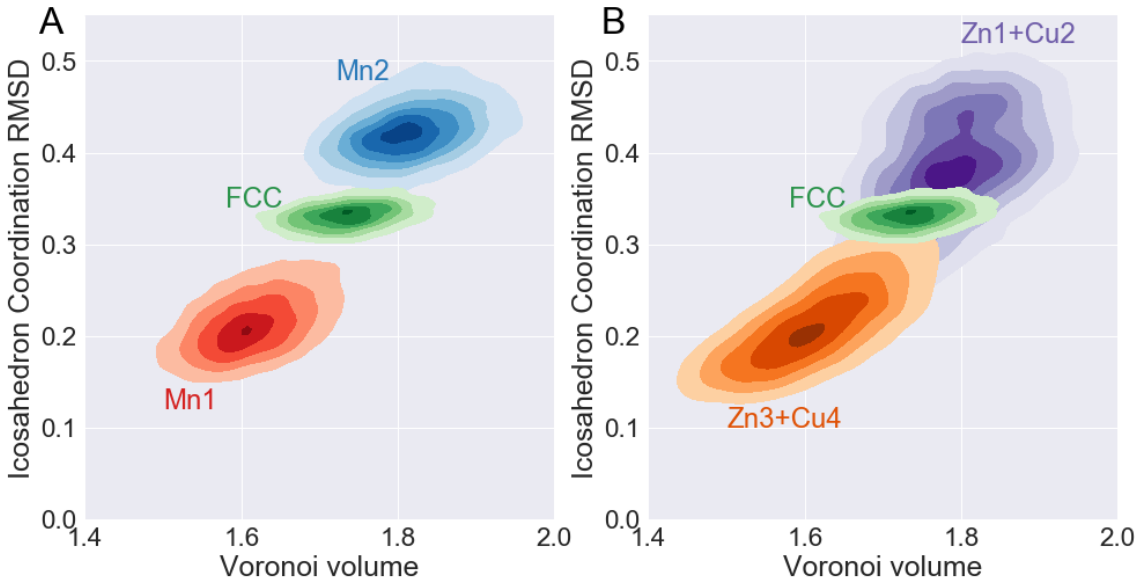

Figure 5.6: Local environment descriptors in terms of the most likely Voronoi cell volumes and icosahedron coordination RMSD for all Wyckoff sites. The color corresponds to contour lines showing the most probable values for these two quantities for each Wyckoff site. **(A)** The two Wyckoff sites of β-Mn have distinct local environments as compared to FCC. Particles in the Mn1 Wyckoff site have a smaller Voronoi cell volume and their 12 nearest neighbors are arranged in a manner more similar to an icosahedron. Particularly in terms of the Voronoi cell volume, the environments in FCC are in between that of the Mn1 and Mn2 sites. **(B)** A similar trend exists in γ-brass when comparing the anisotropic Wyckoff sites (Zn3 and Cu4) with stronger DEFs against the isotropic sites (Zn1 and Cu2). The difference between the environments is not as stark as in β-Mn.

By focusing attention on the x-axis of Fig. 5.6, one can compare the most likely Voronoi cell volumes (which relates to local free volume) for the different Wyckoff sites in these systems. It is clear that in β-Mn and γ-brass, the different Wyckoff sites can correspond to different average Voronoi cell volumes. The anisotropic sites (Mn1, Zn3, and Cu4) occupy smaller Voronoi cells (and will thus have less local free volume) as compared to the isotropic sites (Mn2, Zn1, and Cu2). We observe that the average Voronoi cell volume in the FCC environment is between that of the anisotropic and isotropic sites for the complex crystal structures.

By considering the data from the y-axis along with the x-axis, one sees how a particle's Voronoi cell volume correlates with how similar that particle's coordination environment is to an icosahedron. In β-Mn and γ-brass, the Wyckoff sites with smaller Voronoi cells clearly correspond to environments where the 12 nearest neighbors have a smaller icosahedron coordination RMSD. That the Mn1, Zn3, and Cu4 sites have coordination environments more similar to an icosahedron is expected based on their PMFTs. The Wyckoff sites with a greater average amount of Voronoi volume have coordination environments less similar to an icosahedron. For FCC, the coordination polyhedron is a cuboctahedron, which has little to do with an icosahedron. I find that a particle's Voronoi cell volume has little-to-no correlation with the icosahedron coordination RMSD.

Fig. 5.7 contains the information of Fig. 5.6**(B)** separated out for each Wyckoff site of γ-brass. The Zn1 site has the largest average Voronoi cell volume, and the arrangement of the 12 nearest neighbors is typically the farthest from an icosahedron. The Cu2 site has a moderate average Voronoi cell volume. The two anisotropic Wyckoff sites (Zn3 and Cu4) have very similar distributions. The main exception is that 12.5% of Zn3 sites will have icosahedron coordination RMSD values greater

than 0.4. Visual inspection showed that particles with these outlier coordination environments appear to be randomly distributed throughout space.

One may wonder how the different environments affect the ability of a particle to explore different orientational states within the confines of its lattice position. To address this question, I compute the rotational autocorrelation function for the separate Wyckoff sites. In Fig. 5.8 the difference in behavior for the Wyckoff sites is again readily apparent. The anisotropic Wyckoff sites of Mn1, Zn3, and Cu4 take approximately an order of magnitude longer to decay than the isotropic sites in terms of the rotational autocorrelation function. The behavior in the rotational autocorrelation function for the isotropic sites of β-Mn and γ-brass is similar to that observed in FCC.

The results thus far have shown that the different Wyckoff sites take on different local environments, and these different environments affect the dynamical behavior. Further analysis can provide a fuller picture of how the environments are different across the Wyckoff sites. The first comparison I make is the number of neighbors in the coordination shell for the unique Wyckoff sites. To do so, I compute the histogram of the number of neighbors at each Wyckoff site with a cutoff distance set by the minimum value of the RDF. These results are shown in Figure 5.9. Essentially all particles in FCC and the Mn1 position of β-Mn will have 12 nearest neighbors, in strong agreement with the expected coordination polyhedra. The anisotropic Wyckoff sites of γ-brass (Zn3 and Cu4) have a preference to 12 nearest neighbors, but higher numbers of neighbors will occur approximately 40% of the time. The isotropic, Mn2 Wyckoff site almost always corresponds to 13 or more nearest neighbors, while the isotropic sites of γ-brass (Cu2 and Zn1) can have 11, 12, 13, or 14 nearest neighbors with appreciable probability.

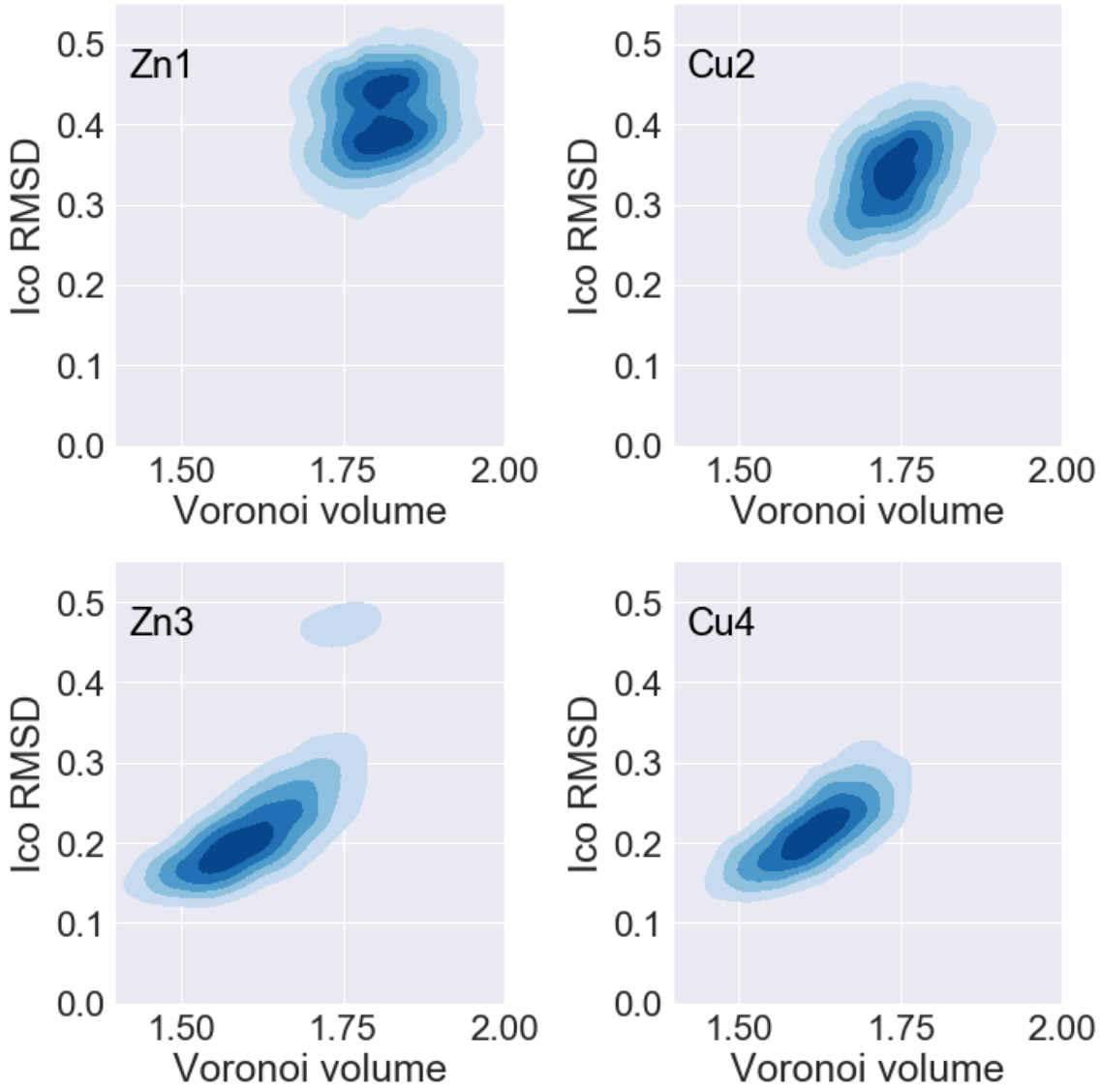

Figure 5.7: Local environment descriptors in terms of the most likely Voronoi cell volumes and icosahedron coordination RMSD for the four Wyckoff sites of γ-brass.

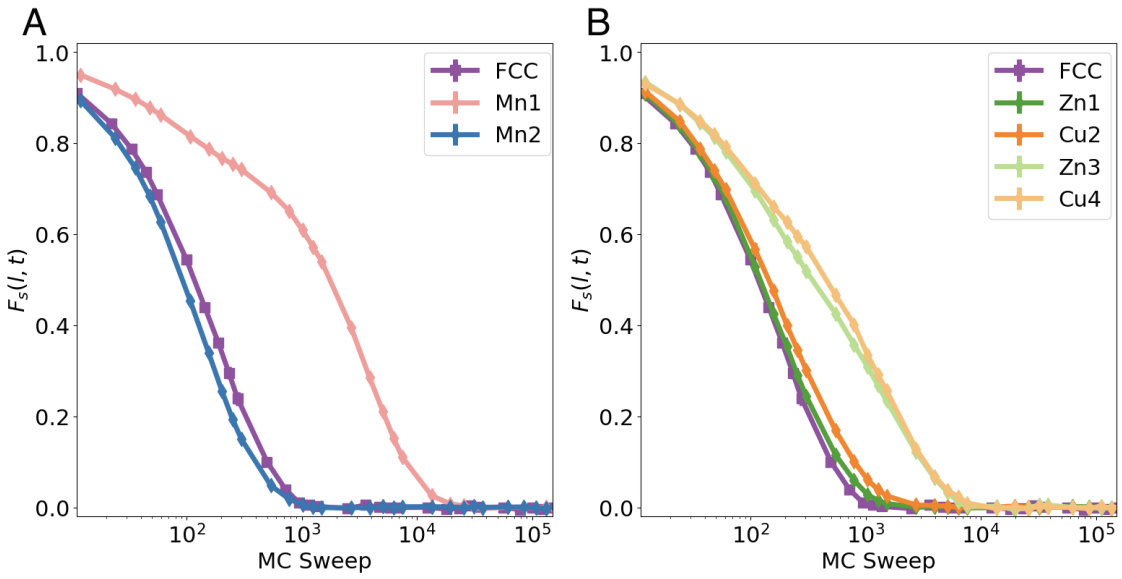

Figure 5.8: The rotational autocorrelation function computed for all Wyckoff sites in FCC, β-Mn, and γ-brass with the shape truncation $T = 1.10$ and density $\phi = 0.575$. **(A)** The lone Wyckoff site of FCC and the Mn2 site of β-Mn show a relatively quick decay in the rotational autocorrelation function. The Mn1 site takes approximately 10,000 more MC sweeps on average for orientations to decouple. **(B)** For γ-brass, the Zn1 and Cu2 sites show similar behavior as the FCC site. The Zn3 and Cu4 sites have longer autocorrelation times.

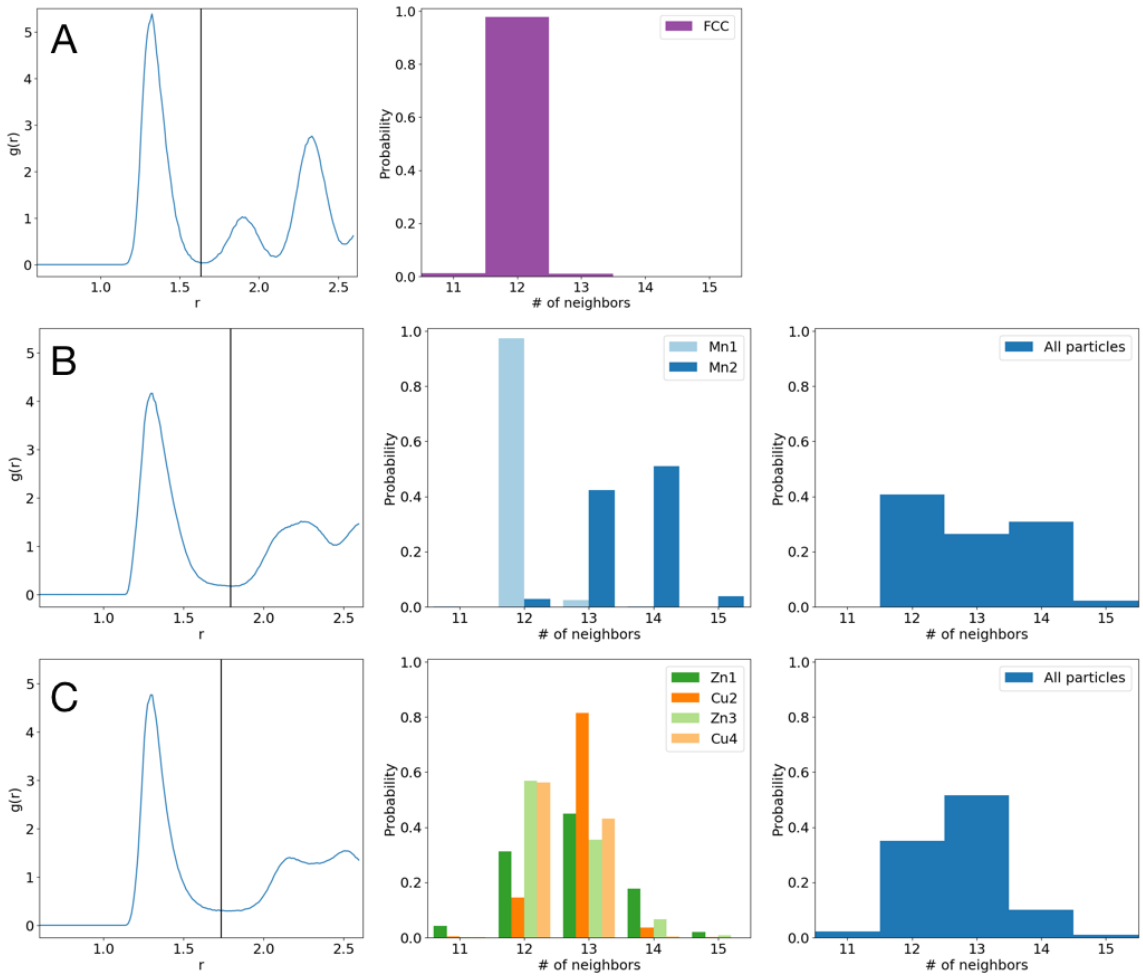

Figure 5.9: The number of neighbors of each Wyckoff site's nearest neighbor coordination shell with the shape truncation $T = 1.10$ and density $\phi = 0.575$. The cutoff in computing the number of neighbors is the location of the minimum value in the radial distribution function (RDF). **(A)** In FCC, all particles have 12 nearest neighbors. **(B)** For β-Mn, nearly all of the anisotropic sites (Mn1) have just 12 nearest neighbors, while the isotropic sites (Mn2) predominantly have 13 neighbors in their first coordination shell. **(C)** For γ-brass, each Wyckoff site is liable to a variable number of neighbors. With the two anisotropic Wyckoff sites (Zn3 & Cu4), it is more likely for such a particle to have 12 nearest neighbors than 13 nearest neighbors. The Zn1 site can potentially have 11, 12, 13, or 14 nearest neighbors, and the Cu2 site predominately has 13 nearest neighbors.

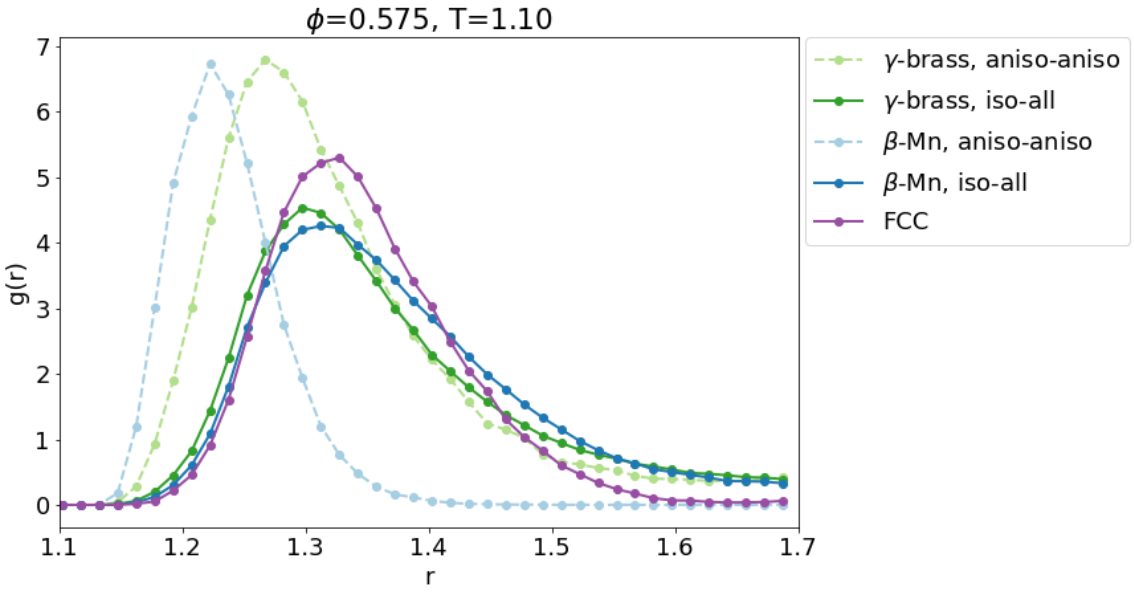

Figure 5.10: The radial distribution function, g(r), over the first neighbor shell for selected comparisons of Wyckoff sites with the shape truncation $T = 1.10$ and density $\phi = 0.575$. For β-Mn and γ-brass, the dotted lines represent the g(r) for the anisotropic sites and other neighboring anisotropic sites, and the solid lines represent g(r) for the isotropic sites computed with all of their neighboring particles. This figure shows that the distances between first neighbor anisotropic sites of β-Mn and γ-brass are shorter than other types of entropic bonds that form at this state point.

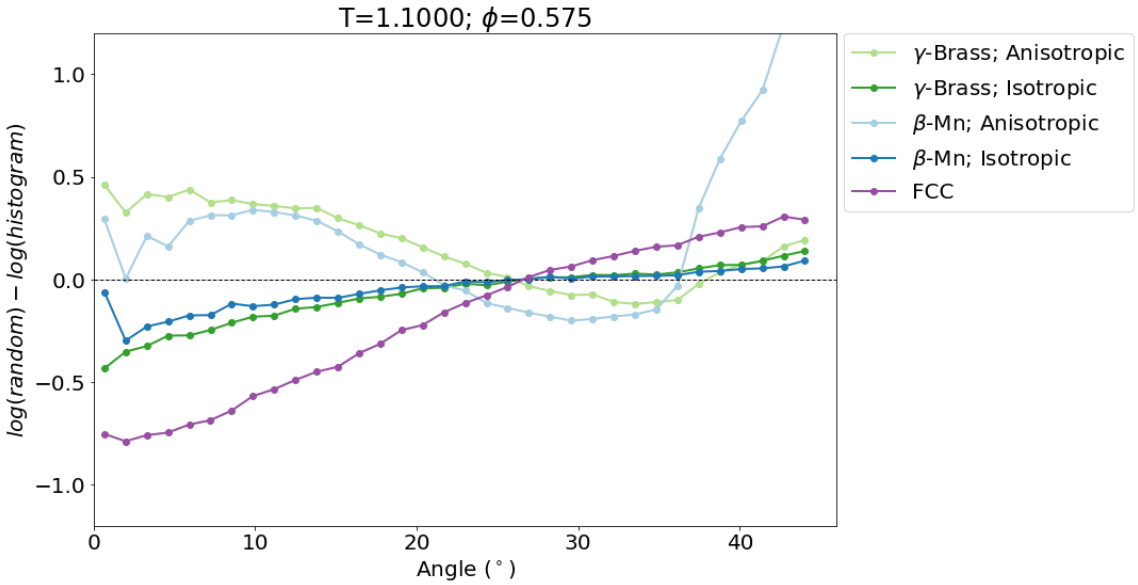

Figure 5.11: A comparison of the most probable minimum angle that separates neighboring particles with the same type of Wyckoff site with the shape truncation $T = 1.10$ and density $\phi = 0.575$. The value plotted is the log of the minimum separation angle histogram for a random distribution subtracted by that of the histogram computed from simulation data. Under this scheme, a negative value corresponds with that angle of separation appearing more frequently than would be expected in the random distribution. I find that separating angles of 25° or less will preferentially occur among particles in FCC or the isotropic Wyckoff sites of β-Mn and γ-brass. Between anisotropic Wyckoff sites of β-Mn and γ-brass, relative orientations offset by an angle between 25° and 38° preferentially occur.

We can also compare how far apart particles are by computing a radial distribution function computed for specific groups of particles. In Fig. 5.10, I compare the radial distribution function for just the anisotropic Wyckoff sites with other anisotropic sites against the isotropic sites with all other particles. I zoom in on the region corresponding to the first neighbor shell. This comparison shows how likely it is to find particles separated by some distance. This figure shows that the anisotropic particles are separated from each other by distances smaller than those between the isotropic sites.

I am also interested in comparing how particles in the different Wyckoff sites are oriented with respect to their neighbors. If the anisotropic Wyckoff sites form

different kinds of entropic bonds with one another as compared to the isotropic Wyckoff sites, then there are likely to be differences in how the neighbors align with each other. Figure 5.11 provides such a comparison by measuring the minimum angle that separates neighboring orientations and plotting the log normalized probability for each angle with respect to the log normalized probability of a random distribution of dodecahedron orientations. In Fig. 5.11, a negative value on the y-axis corresponds to an angular separation occurring more frequently in the system than it does for a random distribution. I find that particles in the anisotropic Wyckoff sites do in fact align differently as compared to the isotropic Wyckoff sites. The anisotropic particles will preferentially be separated by an angle between 25° and 38°. This is significant because in order for the pentagonal facets of two particles to fully align, the particles need to be separated by 36°. These most probable misorientation angles between particles in the anisotropic Wyckoff sites indicates that they arrange with one another to maximize their facet matching area.

5.4 Discussion

From these results, I have shown that dodecahedra are capable of self-assembling phases (β-Mn and γ-brass) in which sets of individual particles behave differently. Most of particles enter into effectively isotropic Wyckoff sites. In comparing particles at the isotropic sites versus the anisotropic ones, the isotropic sites experience weaker DEFs as measured through the PMFT, and they have more local free volume as indicated by their Voronoi cells. Accordingly, the rotational autocorrelation function shows that particles at these isotropic sites can rotate more easily.

Particles in the anisotropic Wyckoff sites of β-Mn and γ-brass (Mn1, Zn3, and Cu4) do not rotate as easily. They occupy lattice positions that correspond to less free

volume, shorter entropic bond distances with particles in other anisotropic sites, and icosahedral coordination environments. In addition to the complex phases, truncated dodecahedra are capable of forming an FCC phase in which there is only a single type of particle environment, and all particles are able to rotate fairly easily. From the results of self-assembly, I have found that FCC is more likely to form than β-Mn and γ-brass when directional entropic forces are expected to be comparatively weak (*i.e.*, when the facets are smaller and/or when the density is lower).

In order to rationalize this behavior, I hypothesize that the complex structures β-Mn and γ-brass form from hard truncated dodecahedra due to a *free volume exchange* of the different Wyckoff sites that is analogous to proposed *charge exchange* observed in atomic systems of Mn atoms [123, 127] and the *mass exchange* mechanism in diblock copolymer systems that form Frank-Kasper phases [124]. This idea relies on a spontaneous symmetry breaking such that previously indistinguishable components take on different characteristics to better minimize free energy. Linus Pauling and Fred Ewing first proposed that something of this nature occurs with Mn atoms occupying the two distinct Wyckoff sites in β-Mn by concluding that the Mn1 atoms have greater electron valence than Mn2 atoms based upon interatomic bond distances [122]. Reinhard Nesper later contended that Mn1 atoms are anionic in nature while the Mn2 atoms are cationic [118]. Calculations of the magnetic properties of Mn atoms in both the α- and β- phases of manganese (with four and two unique Wyckoff positions, respectively) have shown that the electron density of states depends on the Wyckoff position [123, 127]. A related mechanism based on mass exchange has been used to explain the formation of the σ-phase (with five unique Wyckoff positions) from diblock copolymer micelles [124]. In these systems, micelles with uniform mass form a BCC crystal at $28 \leq T \leq 48^{\circ}$ C. Upon cooling, the system transitions to a

σ-phase that requires polymers to diffuse between micelles such that distinct Wyckoff sites are populated by micelles of distinct masses, *i.e.*, the micelles contain different numbers of block copolymers. This crystal symmetry breaking and mass exchange allows the micelles to maximize their average sphericity with decreasing temperature.

To clarify the analogy to atomic systems with metallic bonding: shorter interatomic distances between Mn1 sites suggest a locally higher electron density and thus stronger bonding [118]. With hard dodecahedra, the shorter distance between the anisotropic Wyckoff sites within β-Mn and γ-brass are the result of comparatively stronger directional entropic forces. The same crystallographic sites (*i.e.*, Mn1 in the case of the β-Mn-type structures) exhibit these more strongly bonded particles, despite the fact that the particles themselves, the bonding mechanism, and the nature of the assembled systems as a whole are completely disparate (*i.e.*, atoms *vs.* hard polyhedra, the metallic bond *vs.* directional entropic forces, hard condensed matter *vs.* a model system of colloidal particles).

But *why* would dodecahedra form these phases with fluctuations in the local free volume? We propose the reason for some particles to adopt lower levels of free volume is the result of the icosahedral bonding coordination of the anisotropic Wyckoff sites in β-Mn and γ-brass. Teich *et al.* [70] showed that a dodecahedron surrounded by 12 dodecahedra with icosahedral coordination is a highly favored packing arrangement. Such a configuration corresponds with a particle packed against each of the central dodecahedron's facets. Icosahedral environments are not commensurate with forming periodic structures, but they can exist in high numbers in topologically close-packed structures [125]. As mentioned earlier, the β-Mn and γ-brass structure types contain Wyckoff sites with distorted icosahedra for local coordination polyhedra. As a result, this means that β-Mn and γ-brass are structures that facilitate the

preferred, icosahedrally coordinated, locally dense packing of dodecahedra. These dense local motifs provide greater free volume for the other particles in the system that will occupy the isotropic Wyckoff sites. In other words, a subset of particles (the anisotropic sites) sacrifice their free volume in order to maximize the total entropy of the system.

5.5 Conclusion

I have investigated phases that can self-assemble from truncated dodecahedra: FCC, β-Mn, and γ-brass. FCC is a structure with a single Wyckoff site wherein particles have a coordination polyhedron with cubic symmetry, while β-Mn and γ-brass contain icosahedrally coordinated Wyckoff sites. The multiple coordination environments for β-Mn and γ-brass lead to hard particles behaving differently within a single structure. Particles in an icosahedrally coordinated environment take on more anisotropic characteristics by forming shorter and stronger entropic bonds that lead to longer rotational autocorrelation times. The other particles in the system take on more isotropic characteristics: they experience weaker directional entropic forces and are able to rotate more easily.

I have proposed the idea that β-Mn and γ-brass form as a result of a free volume exchange between the particles such that the icosahedrally coordinated particles (which represents a preferred local dense packing) enter a configuration where movement is restricted. The locally dense configurations of some particles grant a greater amount of free volume to the other particles in the system, which has the effect of increasing the system's entropy. These fluctuations in the local density of complex crystals with multiple Wyckoff sites have analogies with both intermetallics (with symmetry breaking *via* electron charge transfer in elemental metals)[122] and soft-

matter crystals from micelles (with symmetry breaking *via* mass transfer) [124].

CHAPTER VI

Conclusion and Future Outlook

This work expands on the growing field of study into how particle shape affects the self-assembly of hard particles. These hard particle systems can serve as a model for colloidal behavior, and they isolate entropy as the sole driving force in phase behavior. In my work, I examine the connections between particle shape and the bonding valence that arises from directional entropic forces. At the simplest level, directional entropic forces are not terribly hard to understand: particles tend to arrange such that they can maximize the amount of locally accessible free volume. By diving into a few model systems, I have shown how these DEFs operate in practice: they depend on factors such as particle shape, density, and depletion.

In Chapter 2, I showed how depletion can be used to control the self-assembly of cuboctahedra into either a sheared BCC or a simple cubic crystal based on the depletant size. I rationalized this behavior on the grounds of Free Volume Theory wherein I calculated how the different crystal structures affect the entropy of both the colloids and the depletants. I further showed how depletant size will affect the DEFs at the largest facets more strongly when the depletants are sufficiently small. This ability to preferentially increase DEFs should be kept in mind when designing assemblies for particles with multiple facet types.

Depletion is a well known phenomenon in the colloids community, and it has been employed in numerous creative ways. Examples include the separation of different particles [38, 41], control of roughened platelet aggregation based on depletant size [39], and the reconfigurability of rounded cubes between two-dimensional square and rhombic lattices as a result of changing depletant size by cycling temperature [64]. In my work in three-dimensional assemblies, I did not observe complete reconfigurability in both directions: I found that cuboctahedra in a simple cubic crystal would transform into the sheared BCC structure upon increase of depletion size, but decreasing depletion size could not transform the system from sheared BCC to simple cubic. Perhaps this behavior could be a way to impart a sort of memory into a material: if a system contains small depletants and cuboctahedra are in a simple cubic lattice, then it would be known that the system assembled from a previously disordered phase, but if there are small depletants and cuboctahedra are in the sheared BCC packing, then it would be known that the system had previously been in the same packing configuration before the depletants were introduced/decreased in size.

In Chapter 3, I showed how shape changes impact the DEFs in a system. The rounding of a particle and decreasing facet sizes has the effect of reducing and spreading out the DEFS a particle experiences. For low levels of rounding, increasing system density is suitable for maintaining the self-assembly behavior of an unrounded shape. For higher levels of rounding, depletion can be used to enhance the DEFs. My examination of the entropic forces on systems of truncated tetrahedra also showed how there can be competing effects when trying to optimize the valence for a specific crystal. Further work in the "alchemical" ensemble continues to drive home the connections between optimal shape features and the ensuing entropic forces [128, 71].

In Chapter 4, I used new methods to analyze the behavior of plastic crystals,

and I showed how certain shape features will impact the phase behavior. In particular, I showed how three different types of entropic bonding valence connect with density-induced transitions. i.) When bonding valence aligns with coordination set by the crystal, orientational order gradually develops and no thermodynamic phase transition will occur. ii.) When bonding valence does not align with the crystal coordination, a first-order phase transition that coincides with long-ranged orientational order development can be expected. iii.) When bonding valence has many degenerate states, a system behaves as though approaching an orientational glass transition wherein particles adopt a few orientations, but they do not show long-ranged orientational order.

One comparison that I would be interested to see worked out in the future is how the different components of entropy (translational and rotational) compare in a plastic crystal phase versus the fluid phase. Does one of these entropy contributions tend to increase more significantly upon crystallization? If so, how does this depend on the features of the plastic crystal forming shape? Is it possible that some systems undergo translationally driven transitions while others undergo rotationally driven ones? In my limited investigation, I found that rhombic dodecahedron rotate more easily, as evidenced by the rotational autocorrelation function, in a plastic crystal as compared to the fluid. This result indicates that the plastic crystal behavior provides greater rotational entropy. One conclusion that I drew from this project was that when the valence of the entropic bonding does not match the coordination environment dictated by the crystal lattice, a first-order transition will occur. Is there perhaps a related feature with the fluid-to-plastic crystal transition such that these particles do not see as significant of an increase in rotational entropy? Answering these questions would rely on untangling the relationship between translational and

rotational entropy.

In chapter 5, I showed an instance where the DEF valence of truncated dodecahedra can lead to the complex crystals of β-Mn and γ-brass. For these phases, I determined that particles in the different Wyckoff sites rotate at different rates as a result of their different coordination environments. I have proposed that the way in which identical hard particles will take on different amounts of free volume is similar to how previously indistinguishable atoms can take on different charge [122, 123] or diblock copolymer micelles take on different mass [124] in their formation of crystals with multiple Wyckoff sites. I further argued that this behavior specifically occurs because the preferred packing around a single dodecahedron leads to certain particles experiencing strongly icosahedral DEFs. Future work in soft matter systems could attempt to replicate this behavior by applying a bias to icosahedral coordination. Perhaps this behavior could occur with tethered nanoparticles [129]. Some particles could enthalpically bond their tethers in an icosahedral fashion and this could allow other particles to adopt higher free volume configurations.

A future direction for this work on hard dodecahedra would be to study the nucleation and growth of the different crystals. In β-Mn and γ-brass, I showed that particles have different local environments based on the lattice position: how do these environments compare to one another in the growing nucleus? I can envision that the formation of the icosahedrally coordinated sites could be a rate limiting step in this process while the sites with a higher free volume would quickly fill out because these sites do not require neighbors to be arranged in too specific of a manner. Furthermore, comparisons of the growth of the complex crystals with FCC would be interesting. How do factors such as the growth rates and critical nucleus size compare?

BIBLIOGRAPHY

BIBLIOGRAPHY

[1] G. B. Olson, "Designing a new material world," *Science*, vol. 288, no. 5468, pp. 993–998, 2000.

[2] K. F. Jensen, *Chemical Vapor Deposition*, ch. 5, pp. 199–263.

[3] G. M. Whitesides and J. C. Love, "The art of building small," *Scientific American*, vol. 285, no. 3, pp. 38–47, 2001.

[4] G. M. Whitesides and M. Boncheva, "Beyond molecules: Self-assembly of mesoscopic and macroscopic components," *Proceedings of the National Academy of Sciences*, vol. 99, no. 8, pp. 4769–4774, 2002.

[5] G. M. Whitesides and B. Grzybowski, "Self-assembly at all scales," *Science*, vol. 295, no. 5564, pp. 2418–2421, 2002.

[6] G. M. Whitesides, J. P. Mathias, and C. T. Seto, "Molecular self-assembly and nanochemistry: a chemical strategy for the synthesis of nanostructures," *Science*, vol. 254, no. 5036, pp. 1312–1319, 1991.

[7] J.-M. Lehn, "Supramolecular chemistry: receptors, catalysts, and carriers," *Science*, vol. 227, no. 4689, pp. 849–856, 1985.

[8] Q. Chen, S. C. Bae, and S. Granick, "Directed self-assembly of a colloidal kagome lattice," *Nature*, vol. 469, no. 7330, p. 381, 2011.

[9] C. M. Dobson, "Protein folding and misfolding," *Nature*, vol. 426, no. 6968, p. 884, 2003.

[10] S. Colodrero, M. Ocana, and H. Míguez, "Nanoparticle-based one-dimensional photonic crystals," *Langmuir*, vol. 24, no. 9, pp. 4430–4434, 2008.

[11] C. G. Schäfer, D. A. Smolin, G. P. Hellmann, and M. Gallei, "Fully reversible shape transition of soft spheres in elastomeric polymer opal films," *Langmuir*, vol. 29, no. 36, pp. 11275–11283, 2013. PMID: 23947686.

[12] T. S. Ahmadi, Z. L. Wang, T. C. Green, A. Henglein, and M. A. El-Sayed, "Shape-controlled synthesis of colloidal platinum nanoparticles," *Science*, vol. 272, no. 5270, pp. 1924–1925, 1996.

[13] G. Zhang, D. Wang, Z.-Z. Gu, and H. Möhwald, "Fabrication of superhydrophobic surfaces from binary colloidal assembly," *Langmuir*, vol. 21, no. 20, pp. 9143–9148, 2005.

[14] S. C. Glotzer and M. J. Solomon, "Anisotropy of building blocks and their assembly into complex structures," *Nat. Mater.*, vol. 6, no. 8, pp. 557–562, 2007.

[15] Y. Wang, Y. Wang, D. R. Breed, V. N. Manoharan, L. Feng, A. D. Hollingsworth, M. Weck, and D. J. Pine, "Colloids with valence and specific directional bonding," *Nature*, vol. 491, no. 7422, p. 51, 2012.

[16] X. Peng, "Mechanisms for the shape-control and shape-evolution of colloidal semiconductor nanocrystals," *Advanced Materials*, vol. 15, no. 5, pp. 459–463, 2003.

[17] A. Kuijk, A. van Blaaderen, and A. Imhof, "Synthesis of monodisperse, rodlike silica colloids with tunable aspect ratio," *Journal of the American Chemical Society*, vol. 133, no. 8, pp. 2346–2349, 2011.

[18] C.-Y. Chiu, Y. Li, L. Ruan, X. Ye, C. B. Murray, and Y. Huang, "Platinum nanocrystals selectively shaped using facet-specific peptide sequences," *Nature chemistry*, vol. 3, no. 5, p. 393, 2011.

[19] W. van der Stam, A. P. Gantapara, Q. A. Akkerman, G. Soligno, J. D. Meeldijk, R. van Roij, M. Dijkstra, and C. de Mello Donega, "Self-assembly of colloidal hexagonal bipyramid- and bifrustum-shaped zns nanocrystals into two-dimensional superstructures," *Nano letters*, vol. 14, no. 2, pp. 1032–1037, 2014.

[20] S. Glotzer, M. Solomon, and N. A. Kotov, "Self-assembly: From nanoscale to microscale colloids," *AIChE Journal*, vol. 50, no. 12, pp. 2978–2985, 2004.

[21] J.-P. Hansen and I. R. McDonald, *Theory of simple liquids*. Elsevier, 1990.

[22] A. Yethiraj and A. van Blaaderen, "A colloidal model system with an interaction tunable from hard sphere to soft and dipolar," *Nature*, vol. 421, no. 6922, p. 513, 2003.

[23] D. Frenkel, "Computer simulation of hard-core models for liquid crystals," *Computer Physics Communications*, vol. 44, no. 3, pp. 243–253, 1987.

[24] A. Haji-Akbari, M. Engel, A. S. Keys, X. Zheng, R. G. Petschek, P. Palffy-Muhoray, and S. C. Glotzer, "Disordered, quasicrystalline and crystalline phases of densely packed tetrahedra," *Nature*, vol. 462, no. 7274, p. 773, 2009.

[25] U. Agarwal and F. A. Escobedo, "Mesophase behaviour of polyhedral particles," *Nature materials*, vol. 10, pp. 230–235, Mar. 2011.

[26] P. F. Damasceno, M. Engel, and S. C. Glotzer, "Predictive self-assembly of polyhedra into complex structures," *Science*, vol. 337, no. 6093, pp. 453–457, 2012.

[27] A. P. Gantapara, J. de Graaf, R. van Roij, and M. Dijkstra, "Phase diagram and structural diversity of a family of truncated cubes: Degenerate close-packed structures and vacancy-rich states," *Phys. Rev. Lett.*, vol. 111, p. 015501, Jul 2013.

[28] N. Metropolis, A. W. Rosenbluth, M. N. Rosenbluth, A. H. Teller, and E. Teller, "Equation of state calculations by fast computing machines," *The journal of chemical physics*, vol. 21, no. 6, pp. 1087–1092, 1953.

[29] J. A. Anderson, C. D. Lorenz, and A. Travesset, "General purpose molecular dynamics simulations fully implemented on graphics processing units," *Journal of Computational Physics*, vol. 227, no. 10, pp. 5342 – 5359, 2008.

[30] J. Glaser, T. D. Nguyen, J. A. Anderson, P. Liu, F. Spiga, J. A. Millan, D. C. Morse, and S. C. Glotzer, "Strong scaling of general-purpose molecular dynamics simulations on gpus," *Computer Physics Communications*, vol. 192, pp. 97–107, july 2015. HOOMD-blue feature: HOOMD-blue.

[31] J. A. Anderson, M. E. Irrgang, and S. C. Glotzer, "Scalable metropolis monte carlo for simulation of hard shapes," *Computer Physics Communications*, vol. 204, pp. 21–30, July 2016. HOOMD-blue feature: HPMC.

[32] H. N. Lekkerkerker and R. Tuinier, *Colloids and the Depletion Interaction*, vol. 1-222, Ind. Springer, 2011.

[33] F. Oosawa and S. Asakura, "Surface tension of highpolymer solutions," *The Journal of Chemical Physics*, vol. 22, no. 7, pp. 1255–1255, 1954.

[34] S. Asakura and F. Oosawa, "On interaction between two bodies immersed in a solution of macromolecules," *The Journal of Chemical Physics*, vol. 22, no. 7, pp. 1255–1256, 1954.

[35] A. Vrij, "Polymers at interfaces and the interactions in colloidal dispersions," *Pure and Applied Chemistry*, vol. 48, no. 4, pp. 471–483, 1976.

[36] A. McPherson, "Crytsllization of Proteins from Polyethylene Glycol," *Journal of Biological Chemistry*, vol. 251, no. 20, pp. 6300–6303, 1976.

[37] J. Bibette, "Depletion interactions and fractionated crystallization for polydisperse emulsion purification," *Journal of Colloid and Interface Science*, vol. 147, no. 2, pp. 474 – 478, 1991.

[38] T. G. Mason, "Osmotically driven shape-dependent colloidal separations," *Phys. Rev. E*, vol. 66, p. 060402, Dec 2002.

[39] K. Zhao and T. G. Mason, "Directing colloidal self-assembly through roughness-controlled depletion attractions," *Phys. Rev. Lett.*, vol. 99, p. 268301, Dec 2007.

[40] S. Sacanna, W. Irvine, P. M. Chaikin, and D. J. Pine, "Lock and key colloids," *Nature*, vol. 464, no. 7288, p. 575, 2010.

[41] K. Park, H. Koerner, and R. A. Vaia, "Depletion-induced shape and size selection of gold nanoparticles," *Nano Letters*, vol. 10, no. 4, pp. 1433–1439, 2010.

[42] L. Rossi, S. Sacanna, W. T. M. Irvine, P. M. Chaikin, D. J. Pine, and A. P. Philipse, "Cubic crystals from cubic colloids," *Soft Matter*, vol. 7, pp. 4139–4142, 2011.

[43] R. Tuinier, J. Rieger, and C. G. de Kruif, "Depletion-induced phase separation in colloid-polymer mixtures.," *Advances in colloid and interface science*, vol. 103, pp. 1–31, Mar. 2003.

[44] L. Onsager, "The effects of shape on the interaction of colloidal particles," *Annals of the New York Academy of Sciences*, vol. 51, no. 1, pp. 627–659, 1949.

[45] J. G. Kirkwood, "Crystallization as a Cooperative Phenomenon," *Phase Transformations in Solids*, pp. 67–76, 1951.

[46] B. Alder and T. Wainwright, "Phase transition for a hard sphere system," *The Journal of chemical physics*, vol. 27, no. 5, pp. 1208–1209, 1957.

[47] W. W. Wood and J. Jacobson, "Preliminary results from a recalculation of the monte carlo equation of state of hard spheres," *The Journal of Chemical Physics*, vol. 27, no. 5, pp. 1207–1208, 1957.

[48] W. G. Hoover and F. H. Ree, "Melting transition and communal entropy for hard spheres," *The Journal of Chemical Physics*, vol. 49, no. 8, pp. 3609–3617, 1968.

[49] P. N. Pusey and W. Van Megen, "Phase behaviour of concentrated suspensions of nearly hard colloidal spheres," *Nature*, vol. 320, no. 6060, p. 340, 1986.

[50] M. Rutgers, J. Dunsmuir, J.-Z. Xue, W. Russel, and P. Chaikin, "Measurement of the hard-sphere equation of state using screened charged polystyrene colloids," *Physical Review B*, vol. 53, no. 9, p. 5043, 1996.

[51] J. Zhu, M. Li, R. Rogers, W. Meyer, R. Ottewill, W. Russel, P. Chaikin, *et al.*, "Crystallization of hard-sphere colloids in microgravity," *Nature*, vol. 387, no. 6636, p. 883, 1997.

[52] D. Frenkel, H. Lekkerkerker, and A. Stroobants, "Thermodynamic stability of a smectic phase in a system of hard rods," *Nature*, vol. 332, no. 6167, p. 822, 1988.

[53] A. Haji-Akbari, M. Engel, and S. C. Glotzer, "Phase diagram of hard tetrahedra," *The Journal of Chemical Physics*, vol. 135, no. 19, p. 194101, 2011.

[54] R. Ni, A. P. Gantapara, J. de Graaf, R. van Roij, and M. Dijkstra, "Phase diagram of colloidal hard superballs: from cubes via spheres to octahedra," *Soft Matter*, vol. 8, pp. 8826–8834, 2012.

[55] A. P. Gantapara, J. de Graaf, R. van Roij, and M. Dijkstra, "Phase behavior of a family of truncated hard cubes," *The Journal of Chemical Physics*, vol. 142, no. 5, p. 054904, 2015.

[56] A. Sharma, V. Thapar, and F. Escobedo, "Solid-Phase Nucleation Free-energy Barriers in Truncated Cubes: Interplay of Localized Orientational Order and Facet Alignment," *Soft Matter*, 2018.

[57] D. Seo, J. C. Park, and H. Song, "Polyhedral gold nanocrystals with o h symmetry: From octahedra to cubes," *Journal of the American Chemical Society*, vol. 128, no. 46, pp. 14863–14870, 2006.

[58] E. C. Greyson, J. E. Barton, and T. W. Odom, "Tetrahedral zinc blende tin sulfide nano-and microcrystals," *Small*, vol. 2, no. 3, pp. 368–371, 2006.

[59] J. Henzie, M. Grünwald, A. Widmer-Cooper, P. L. Geissler, and P. Yang, "Self-assembly of uniform polyhedral silver nanocrystals into densest packings and exotic superlattices.," *Nature Materials*, vol. 11, pp. 131–137, Feb. 2012.

[60] S. Sun, C. B. Murray, D. Weller, L. Folks, and A. Moser, "Monodisperse fept nanoparticles and ferromagnetic fept nanocrystal superlattices," *Science*, vol. 287, no. 5460, pp. 1989–1992, 2000.

[61] A. Tao, P. Sinsermsuksakul, and P. Yang, "Polyhedral silver nanocrystals with distinct scattering signatures," *Angewandte Chemie International Edition*, vol. 45, no. 28, pp. 4597–4601, 2006.

[62] K. L. Young, M. L. Personick, M. Engel, P. F. Damasceno, S. N. Barnaby, R. Bleher, T. Li, S. C. Glotzer, B. Lee, and C. A. Mirkin, "A directional entropic force approach to assemble anisotropic nanoparticles into superlattices," *Angewandte Chemie International Edition*, vol. 52, no. 52, pp. 13980–13984, 2013.

[63] H. R. Vutukuri, A. Imhof, and A. Van Blaaderen, "Fabrication of polyhedral particles from spherical colloids and their self-assembly into rotator phases," *Angewandte Chemie - International Edition*, vol. 53, no. 50, pp. 13830–13834, 2014.

[64] L. Rossi, V. Soni, D. J. Ashton, D. J. Pine, A. P. Philipse, P. M. Chaikin, M. Dijkstra, S. Sacanna, and W. T. M. Irvine, "Shape-sensitive crystallization in colloidal superball fluids," *Proceedings of the National Academy of Sciences*, vol. 112, no. 17, pp. 5286–5290, 2015.

[65] J. Gong, R. S. Newman, M. Engel, M. Zhao, F. Bian, S. C. Glotzer, and Z. Tang, "Shape-dependent ordering of gold nanocrystals into large-scale superlattices," *Nature communications*, vol. 8, p. 14038, 2017.

[66] J.-M. Meijer, A. Pal, S. Ouhajji, H. N. W. Lekkerkerker, A. P. Philipse, and A. V. Petukhov, "Observation of solid-solid transitions in 3D crystals of colloidal superballs," *Nature Communications*, vol. 8, p. 14352, 2017.

[67] P. F. Damasceno, M. Engel, and S. C. Glotzer, "Crystalline assemblies and densest packings of a family of truncated tetrahedra and the role of directional entropic forces," *ACS Nano*, vol. 6, no. 1, pp. 609–614, 2012.

[68] G. van Anders, D. Klotsa, N. K. Ahmed, M. Engel, and S. C. Glotzer, "Understanding shape entropy through local dense packing," *Proceedings of the National Academy of Sciences*, vol. 111, no. 45, pp. E4812–E4821, 2014.

[69] G. van Anders, N. K. Ahmed, R. Smith, M. Engel, and S. C. Glotzer, "Entropically patchy particles: Engineering valence through shape entropy," *ACS Nano*, vol. 8, no. 1, pp. 931–940, 2014.

[70] E. G. Teich, G. van Anders, D. Klotsa, J. Dshemuchadse, and S. C. Glotzer, "Clusters of polyhedra in spherical confinement," *Proceedings of the National Academy of Sciences*, vol. 113, no. 6, pp. E669–E678, 2016.

[71] Y. Geng, G. van Anders, P. M. Dodd, J. Dshemuchadse, and S. C. Glotzer, "Engineering entropy for the inverse design of colloidal crystals from hard shapes," *arXiv preprint arXiv:1712.02471*, 2017.

[72] G. van Anders, D. Klotsa, A. S. Karas, P. M. Dodd, and S. C. Glotzer, "Digital alchemy for materials design: Colloids and beyond," *ACS Nano*, vol. 9, no. 10, pp. 9542–9553, 2015. PMID: 26401754.

[73] E. S. Harper, G. van Anders, and S. C. Glotzer, "Nature of the entropic bond in particle assemblies," *In preparation*, 2018.

[74] H. N. Lekkerkerker, W. Poon, P. Pusey, A. Stroobants, and P. Warren, "Phase Behaviour of Colloid + Polymer Mixtures," *Europhysics Letters*, vol. 20, no. 6, pp. 559–564, 1992.

[75] A. S. Karas, J. Glaser, and S. C. Glotzer, "Using depletion to control colloidal crystal assemblies of hard cuboctahedra," *Soft Matter*, vol. 12, pp. 5199–5204, 2016.

[76] K. Zhao and T. G. Mason, "Suppressing and enhancing depletion attractions between surfaces roughened by asperities," *Phys. Rev. Lett.*, vol. 101, p. 148301, Sep 2008.

[77] K. L. Young, M. L. Personick, M. Engel, P. F. Damasceno, S. N. Barnaby, R. Bleher, T. Li, S. C. Glotzer, B. Lee, and C. A. Mirkin, "A directional entropic force approach to assemble anisotropic nanoparticles into superlattices," *Angewandte Chemie International Edition*, vol. 52, no. 52, pp. 13980–13984, 2013.

[78] J. Glaser, A. S. Karas, and S. C. Glotzer, "A parallel algorithm for implicit depletant simulations," *The Journal of Chemical Physics*, vol. 143, no. 18, p. 184110, 2015.

[79] E. S. Harper, R. L. Marson, J. A. Anderson, G. van Anders, and S. C. Glotzer, "Shape allophiles improve entropic assembly," *Soft Matter*, vol. 11, pp. 7250–7256, 2015.

[80] M. Dijkstra, R. van Roij, and R. Evans, "Phase diagram of highly asymmetric binary hard-sphere mixtures," *Phys. Rev. E*, vol. 59, pp. 5744–5771, May 1999.

[81] S. M. Oversteegen and R. Roth, "General methods for free-volume theory," *The Journal of Chemical Physics*, vol. 122, no. 21, p. 214502, 2005.

[82] B. Widom, "Some topics in the theory of fluids," *The Journal of Chemical Physics*, vol. 39, no. 11, pp. 2808–2812, 1963.

[83] D. Frenkel and A. J. C. Ladd, "New monte carlo method to compute the free energy of arbitrary solids. application to the fcc and hcp phases of hard spheres," *The Journal of Chemical Physics*, vol. 81, no. 7, pp. 3188–3193, 1984.

[84] R. L. C. Vink and J. Horbach, "Grand canonical monte carlo simulation of a model colloid-polymer mixture: Coexistence line, critical behavior, and interfacial tension," *The Journal of Chemical Physics*, vol. 121, no. 7, pp. 3253–3258, 2004.

[85] P. G. Bolhuis, A. A. Louis, and J.-P. Hansen, "Influence of polymer-excluded volume on the phase-behavior of colloid-polymer mixtures," *Phys. Rev. Lett.*, vol. 89, p. 128302, Sep 2002.

[86] M. Dijkstra, R. van Roij, and R. Evans, "Direct simulation of the phase behavior of binary hard-sphere mixtures: Test of the depletion potential description," *Phys. Rev. Lett.*, vol. 82, pp. 117–120, Jan 1999.

[87] M. Dijkstra, J. M. Brader, and R. Evans, "Phase behaviour and structure of model colloid-polymer mixtures," *Journal of Physics: Condensed Matter*, vol. 11, no. 50, p. 10079, 1999.

[88] D. Frenkel and B. Smit, *Understanding Molecular Simulation*. Computational Science, Academic Press, 2 ed., 11 2001.

[89] L. Rovigatti, N. Gnan, A. Parola, and E. Zaccarelli, "How soft repulsion enhances the depletion mechanism," *Soft Matter*, vol. 11, pp. 692–700, 2015.

[90] N. A. Mahynski, S. K. Kumar, and A. Z. Panagiotopoulos, "Relative stability of the fcc and hcp polymorphs with interacting polymers," *Soft Matter*, vol. 11, pp. 280–289, 2015.

[91] P. F. Damasceno, A. S. Karas, B. A. Schultz, M. Engel, and S. C. Glotzer, "Controlling chirality of entropic crystals," *Phys. Rev. Lett.*, vol. 115, p. 158303, Oct 2015.

[92] A. Tao, P. Sinsermsuksakul, and P. Yang, "Polyhedral silver nanocrystals with distinct scattering signatures," *Angewandte Chemie*, vol. 118, no. 28, pp. 4713–4717, 2006.

[93] Y. Zhang, F. Lu, D. van der Lelie, and O. Gang, "Continuous phase transformation in nanocube assemblies," *Physical Review Letters*, vol. 107, no. 13, p. 135701, 2011.

[94] E. R. Chen, D. Klotsa, M. Engel, P. F. Damasceno, and S. C. Glotzer, "Complexity in surfaces of densest packings for families of polyhedra," *Physical Review X*, vol. 4, no. 1, p. 011024, 2014.

[95] C. X. Du, G. van Anders, R. S. Newman, and S. C. Glotzer, "Shape-driven solid–solid transitions in colloids," *Proceedings of the National Academy of Sciences*, vol. 114, no. 20, pp. E3892–E3899, 2017.

[96] B. A. Schultz, P. F. Damasceno, M. Engel, and S. C. Glotzer, "Symmetry considerations for the targeted assembly of entropically stabilized colloidal crystals via voronoi particles," *ACS Nano*, vol. 9, no. 3, pp. 2336–2344, 2015. PMID: 25692863.

[97] F. M. van der Kooij and H. N. W. Lekkerkerker, "Formation of Nematic Liquid Crystals in Suspensions of Hard Colloidal Platelets," *The Journal of Physical Chemistry B*, vol. 102, no. 40, pp. 7829–7832, 1998.

[98] H. Kikuchi, M. Yokota, Y. Hisakado, H. Yang, and T. Kajiyama, "Polymer-stabilized liquid crystal blue phases," *Nature Materials*, vol. 1, no. 1, pp. 64–68, 2002.

[99] L. Pauling, "The rotational motion of molecules in crystals," *Physical Review*, vol. 36, no. 3, p. 430, 1930.

[100] Timmermans, J., "Un nouvel état mésomorphe les cristaux organiques plastiques," *J. Chim. Phys.*, vol. 35, pp. 331–344, 1938.

[101] J. Timmermans, "Plastic crystals: A historical review," *Journal of Physics and Chemistry of Solids*, vol. 18, no. 1, pp. 1–8, 1961.

[102] J. N. Sherwood, ed., *The Plastically Crystalline State*. John Wiley & Sons, Ltd., 1979.

[103] R. Brand, P. Lunkenheimer, and A. Loidl, "Relaxation dynamics in plastic crystals," *Journal of Chemical Physics*, vol. 116, no. 23, pp. 10386–10401, 2002.

[104] C. Talón, M. A. Ramos, and S. Vieira, "Low-temperature specific heat of amorphous, orientational glass, and crystal phases of ethanol," *Physical Review B*, vol. 66, no. 1, pp. 1–4, 2002.

[105] O. Yamamuro, H. Yamasaki, Y. Madokoro, I. Tsukushi, and T. Matsuo, "Calorimetric and neutron scattering studies of plastically crystalline cyclooctanol*," *Journal of Physics: Condensed Matter*, vol. 15, no. 32, pp. 5439–5450, 2003.

[106] J. C. W. Folmer, R. L. Withers, T. R. Welberry, and J. D. Martin, "Coupled orientational and displacive degrees of freedom in the high-temperature plastic phase of the carbon tetrabromide $\alpha-\mathrm{Cbr}_4$," *Physical Review B - Condensed Matter and Materials Physics*, vol. 77, no. 14, pp. 1–10, 2008.

[107] W. Shen, G. van Anders, J. A. Anderson, J. Antonaglia, M. Engel, and S. C. Glotzer, "Orientational ordering of hard regular polygons in plastic crystals," *In preparation*, 2018.

[108] L. Filion, M. Marechal, B. van Oorschot, D. Pelt, F. Smallenburg, and M. Dijkstra, "Efficient method for predicting crystal structures at finite temperature: Variable box shape simulations," *Phys. Rev. Lett.*, vol. 103, p. 188302, Oct 2009.

[109] J. A. C. Veerman and D. Frenkel, "Phase behavior of disklike hard-core mesogens," *Phys. Rev. A*, vol. 45, pp. 5632–5648, Apr 1992.

[110] P. D. Duncan, M. Dennison, A. J. Masters, and M. R. Wilson, "Theory and computer simulation for the cubatic phase of cut spheres," *Phys. Rev. E*, vol. 79, p. 031702, Mar 2009.

[111] E. S. Harper, M. Spellings, J. A. Anderson, and S. C. Glotzer, "Freud: a software suite for high-throughput simulation analysis," *In preparation*, 2018.

[112] R. E. Cutkosky, "Harmonic functions and matrix elements for hyperspherical quantum field models," *Journal of Mathematical Physics*, vol. 25, no. 4, pp. 939–942, 1984.

[113] J. A. Anderson, J. Antonaglia, J. A. Millan, M. Engel, and S. C. Glotzer, "Shape and symmetry determine two-dimensional melting transitions of hard regular polygons," *Phys. Rev. X*, vol. 7, p. 021001, Apr 2017.

[114] J. E. Mayer and W. W. Wood, "Interfacial tension effects in finite, periodic, two-dimensional systems," *The Journal of Chemical Physics*, vol. 42, no. 12, pp. 4268–4274, 1965.

[115] J. K. Mason and C. A. Schuh, "The generalized Mackenzie distribution: Disorientation angle distributions for arbitrary textures," *Acta Materialia*, vol. 57, no. 14, pp. 4186–4197, 2009.

[116] N. Goldenfeld, *Lectures On Phase Transitions And The Renormalization Group (Frontiers in Physics)*. Addison-Wesley, 1992.

[117] C. B. Shoemaker, D. P. Shoemaker, T. Hopkins, and S. Yindepit, "Refinement of the structure of β-manganese and of a related phase in the Mn–Ni–Si system," *Acta Crystallographica Section B: Structural Crystallography and Crystal Chemistry*, vol. 34, no. 12, pp. 3573–3576, 1978.

[118] R. Nesper, "Bonding patterns in intermetallic compounds," *Angewandte Chemie International Edition*, vol. 30, no. 7, pp. 789–817, 1991.

[119] H. Nakamura, K. Yoshimoto, M. Shiga, M. Nishi, and K. Kakurai, "Strong antiferromagnetic spin fluctuations and the quantum spin-liquid state in geometrically frustrated-Mn, and the transition to a spin-glass state caused by non-magnetic impurity," *Journal of Physics: Condensed Matter*, vol. 9, no. 22, p. 4701, 1997.

[120] O. Gourdon, D. Gout, D. J. Williams, T. Proffen, S. Hobbs, and G. J. Miller, "Atomic distributions in the γ-brass structure of the Cu-Zn system: a structural and theoretical study," *Inorganic chemistry*, vol. 46, no. 1, pp. 251–260, 2007.

[121] W. Xie, S. Thimmaiah, J. Lamsal, J. Liu, T. W. Heitmann, D. Quirinale, A. I. Goldman, V. Pecharsky, and G. J. Miller, "β-Mn-type $Co_{8+x}Zn_{12-x}$ as a defect cubic laves phase: Site preferences, magnetism, and electronic structure," *Inorganic Chemistry*, vol. 52, no. 16, pp. 9399–9408, 2013. PMID: 23909791.

[122] L. Pauling and F. J. Ewing, "The ratio of valence electrons to atoms in metals and intermetallic compounds," *Rev. Mod. Phys.*, vol. 20, pp. 112–122, Jan 1948.

[123] D. Hobbs, J. Hafner, and D. Spišák, "Understanding the complex metallic element Mn. i. crystalline and noncollinear magnetic structure of α-Mn," *Phys. Rev. B*, vol. 68, p. 014407, Jul 2003.

[124] S. Lee, C. Leighton, and F. S. Bates, "Sphericity and symmetry breaking in the formation of frank–kasper phases from one component materials," *Proceedings of the National Academy of Sciences*, vol. 111, no. 50, pp. 17723–17731, 2014.

[125] F. Frank and J. Kasper, "Complex alloy structures regarded as sphere packings. i. definitions and basic principles," *Acta Crystallographica*, vol. 11, no. 3, pp. 184–190, 1958.

[126] D. W. Scott, *Multivariate density estimation: theory, practice, and visualization*. John Wiley & Sons, 2015.

[127] J. Hafner and D. Hobbs, "Understanding the complex metallic element Mn. ii. geometric frustration in β-Mn, phase stability, and phase transitions," *Phys. Rev. B*, vol. 68, p. 014408, Jul 2003.

[128] R. K. Cersonsky, G. van Anders, P. M. Dodd, and S. C. Glotzer, "Relevance of packing to colloidal self-assembly," *Proceedings of the National Academy of Sciences*, 2018.

[129] R. L. Marson, C. L. Phillips, J. A. Anderson, and S. C. Glotzer, "Phase behavior and complex crystal structures of self-assembled tethered nanoparticle telechelics," *Nano Letters*, vol. 14, no. 4, pp. 2071–2078, 2014. PMID: 24641517.